

# AJUR

American Journal of  
*Undergraduate Research*

Volume 13 | Issue 1 | January 2016

[www.ajuronline.org](http://www.ajuronline.org)

# AJUR

American Journal of  
*Undergraduate Research*

---

Volume 13 | Issue 1 | January 2016

[www.ajuronline.org](http://www.ajuronline.org)

---

- 2      **AJUR History and Editorial Board**
- 3      **Special Thanks to AJUR's Sponsors**
- 5      **Einstein's 1905 Paper on  $E=mc^2$**   
*Patrick Moylan, James Lombardi & Stephen Moylan*
- 11     **Aberrant DNMT3B7 Expression Correlates to Age, Race, and  
Hormone Receptor Status in Breast Cancer Patients**  
*Christian C.S. Mullin, Jennifer J. Busser, Anna M. Ciampanelli & Stacey L. Raimondi*
- 21     **Numerical Prediction of Microbubble Attachment in  
Biological Flows**  
*Joshua Gosney & Jeffrey J. Heys*
- 31     **Utilizing Machine Learning to Accelerate Automated  
Assignment of Backbone NMR Data**  
*Joel Venzke, David Mascharka, Paxten Johnson, Rachel Davis, Katie Roth, Leah  
Robison, Adina Kilpatrick & Timothy Urness*
- 41     **Approximate Formulae for Willmore Surfaces via Support Functions  
and Matlab**  
*Phillip M. Galboa & Michael C. Barg*
- 51     **Preparation of *t*-Butyldimethylphosphine Borane and  
*t*-Butyldiethylphosphine Borane by Selective Grignard Reagent  
Substitution of Phosphorus Trichloride**  
*Auston G. Butterfield, Matthew B. Prater & Nathan S. Werner*
- 59     **The Effect of *Umbellularia californica* Essential Oil on Blood Vessel  
Diameter in Frogs**  
*Holden M. Wagstaff, Stephan R. Maman, Mary Jo Tufte & Matthew S. Weeg*
- 65     **The Wellbeing of Young Adults as a Function of Parental Status in  
Rural Tanzania**  
*H. Callie Silver*
-

American Journal of Undergraduate Research (AJUR) is a national, peer-reviewed, open-source, quarterly, multidisciplinary student research journal. It is indexed internationally by EBSCO, and is listed via the Library of Congress under ISSNs of 1536-4585 (for print) and 2375-8732 (for web). The journal was established in 2002.

### EDITORIAL TEAM *Volume 13 | Issue 1 | January 2016*

Dr. Kestutis G. Bendinskas, Editor, [editor@ajuronline.org](mailto:editor@ajuronline.org)  
 Dr. Anthony Contento, Assistant Technical Editor, [technicaleditor@ajuronline.org](mailto:technicaleditor@ajuronline.org)  
 Rose Throop, Art and Copy Editor, [copyeditor@ajuronline.org](mailto:copyeditor@ajuronline.org)  
 Daniel Laird, Web Master, [webmaster@ajuronline.org](mailto:webmaster@ajuronline.org)

### EDITORIAL BOARD *by subject area*

#### ACCOUNTING

Dr. Dean Crawford,  
[dean.crawford@oswego.edu](mailto:dean.crawford@oswego.edu)

#### ART HISTORY

Dr. Lisa Seppi,  
[lisa.seppi@oswego.edu](mailto:lisa.seppi@oswego.edu)

#### ASTROPHYSICS

Dr. Shashi Kanbur,  
[shashi.kanbur@oswego.edu](mailto:shashi.kanbur@oswego.edu)

#### BEHAVIORAL NEUROSCIENCE

Dr. Aileen M. Bailey,  
[ambailey@smcm.edu](mailto:ambailey@smcm.edu)

#### BIOCHEMISTRY

Dr. Pamela K. Kerrigan,  
[pamela.kerrigan@mountsaintvincent.edu](mailto:pamela.kerrigan@mountsaintvincent.edu)

#### BIOENGINEERING

Dr. Jorge I. Rodriguez,  
[jorger@clemson.edu](mailto:jorger@clemson.edu)

#### BIOINFORMATICS

Dr. Kevin Daimi,  
[daimikj@udmercy.edu](mailto:daimikj@udmercy.edu)  
 Dr. John R. Jungck,  
[jungck@udel.edu](mailto:jungck@udel.edu)

#### BIOLOGY, PHYSIOLOGY

Dr. David Dunn,  
[david.dunn@oswego.edu](mailto:david.dunn@oswego.edu)

#### BIOLOGY, DEVELOPMENTAL

Dr. Poongodi Geetha-Loganathan,  
[p.geethaloganathan@oswego.edu](mailto:p.geethaloganathan@oswego.edu)

#### BIOLOGY, MICROBIOLOGY

Dr. Peter Newell,  
[peter.newell@oswego.edu](mailto:peter.newell@oswego.edu)

#### BOTANY

Dr. William R. Bromer,  
[wbromer@stfrancis.edu](mailto:wbromer@stfrancis.edu)  
 Dr. Julien Bachelier,  
[julien.bachelier@oswego.edu](mailto:julien.bachelier@oswego.edu)

#### CHEMISTRY

Dr. Alfredo Castro,  
[castroa@felician.edu](mailto:castroa@felician.edu)  
 Dr. Charles Kriley,  
[cekriley@gcc.edu](mailto:cekriley@gcc.edu)  
 Dr. Douglas Mulford,  
[douglas.mulford@emory.edu](mailto:douglas.mulford@emory.edu)  
 Dr. Mark A. Benvenuto,  
[benvenma@udmercy.edu](mailto:benvenma@udmercy.edu)

#### CHEMISTRY, PHYSICAL

Dr. John Oakes,  
[john.oakes@gcccd.net](mailto:john.oakes@gcccd.net)

#### COMPUTATIONAL SCIENCES

Dr. Dele Oluwade,  
[deleoluwade@yahoo.com](mailto:deleoluwade@yahoo.com)  
 Dr. J. Ben Schafer,  
[schafer@cs.uni.edu](mailto:schafer@cs.uni.edu)

#### ECOLOGY

Dr. William R. Bromer,  
[wbromer@stfrancis.edu](mailto:wbromer@stfrancis.edu)

#### EDUCATION, PHYSICS

Dr. Andrew D. Gavrin,  
[agavrin@iupui.edu](mailto:agavrin@iupui.edu)

#### ENGINEERING, ENVIRONMENTAL

Dr. Eileen M. Cashman,  
[eileen.cashman@humboldt.edu](mailto:eileen.cashman@humboldt.edu)

#### ENVIRONMENTAL SCIENCE

Dr. Eileen M. Cashman,  
[eileen.cashman@humboldt.edu](mailto:eileen.cashman@humboldt.edu)

#### GEOLOGY

Dr. Larry Davis,  
[ldavis@csbsju.edu](mailto:ldavis@csbsju.edu)

#### HONORARY EDITORIAL BOARD MEMBER

Dr. Lorrie Clemo,  
[lorrie.clemo@oswego.edu](mailto:lorrie.clemo@oswego.edu)

#### KINESIOLOGY / EXERCISE SCIENCE

Dr. David Senchina,  
[david.senchina@drake.edu](mailto:david.senchina@drake.edu)

#### LITERARY STUDIES

Dr. Douglas Guerra,  
[douglas.guerra@oswego.edu](mailto:douglas.guerra@oswego.edu)

#### MATHEMATICS

Dr. Nkechi M. Agwu,  
[nagwu@bmcc.cuny.edu](mailto:nagwu@bmcc.cuny.edu)  
 Dr. John Emert,  
[emert@bsu.edu](mailto:emert@bsu.edu)  
 Dr. Jeffrey J. Boats,  
[boatsjj@udmercy.edu](mailto:boatsjj@udmercy.edu)  
 Dr. J.D. Phillips,  
[jophilli@nmu.edu](mailto:jophilli@nmu.edu)  
 Dr. Dele Oluwade,  
[deleoluwade@yahoo.com](mailto:deleoluwade@yahoo.com)

#### METEOROLOGY

Dr. Steven Skubis,  
[steven.skubis@oswego.edu](mailto:steven.skubis@oswego.edu)

#### NEUROSCIENCE

Dr. Pamela E. Scott-Johnson,  
[pamela.scottjohnson@morgan.edu](mailto:pamela.scottjohnson@morgan.edu)  
 Dr. Amy Overman,  
[aoverman@elon.edu](mailto:aoverman@elon.edu)

#### PHYSICS

Dr. Carolina Ilie,  
[carolina.ilie@oswego.edu](mailto:carolina.ilie@oswego.edu)

#### PSYCHOLOGY

Dr. Amy Overman,  
[aoverman@elon.edu](mailto:aoverman@elon.edu)  
 Dr. Pamela E. Scott-Johnson,  
[pamela.scottjohnson@morgan.edu](mailto:pamela.scottjohnson@morgan.edu)

#### STATISTICS

Dr. Mark Ecker,  
[mark.ecker@uni.edu](mailto:mark.ecker@uni.edu)

#### TECHNOLOGY, ENGINEERING

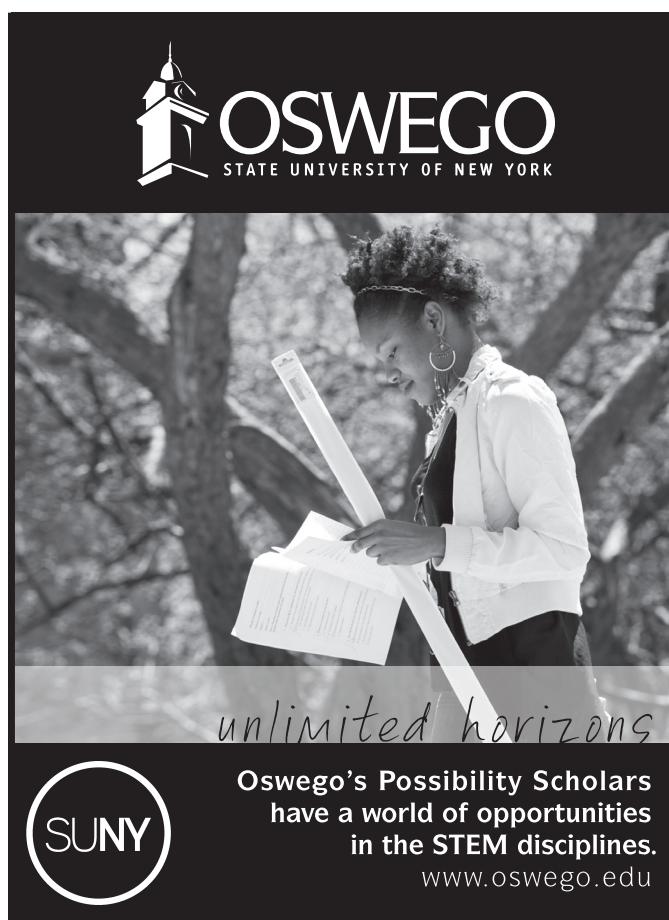
Dr. Recayi Pecen,  
[regpecen@na.edu](mailto:regpecen@na.edu)

## SPECIAL THANKS

AJUR is made possible through the assistance of our sponsors.

Support for this issue has been provided by  
the Office of the Provost, at the State University of New York at Oswego.

Thank you!



  
**OSWEGO**  
STATE UNIVERSITY OF NEW YORK

*unlimited horizons*

 Oswego's Possibility Scholars  
have a world of opportunities  
in the STEM disciplines.  
[www.oswego.edu](http://www.oswego.edu)

Interested in supporting quality undergraduate research?  
Request sponsorship information at [editor@ajuronline.org](mailto:editor@ajuronline.org)



## Einstein's 1905 Paper on $E=mc^2$

Patrick Moylan<sup>a</sup>, James Lombardi<sup>b\*</sup> and Stephen Moylan<sup>c\*</sup>

<sup>a</sup>Department of Physics, The Pennsylvania State University, Abington College, Abington, PA

<sup>b</sup>Department of Computer Engineering, The Pennsylvania State University, University Park, PA

<sup>c</sup>Department of Physics, The Pennsylvania State University, University Park, PA

Students: jcl5395@psu.edu\*, sam604@psu.edu\*

Mentor: pjm11@psu.edu

### ABSTRACT

It is well-known that Einstein's first paper on  $E = mc^2$  as published in the *Annalen der Physik* in 1905 is problematic in that it suffers from the error of circular reasoning. This means that it uses as one of its premises a statement which is equivalent to the conclusion of the paper, namely, that  $E = mc^2$ . This difficulty with the paper has been pointed out by many writers including Max Planck, Herbert Ives, Max Jammer and also biographers of Einstein including Gerald Holton and Arthur I. Miller. Unfortunately, the derivation is repeated today as being correct without any mention of the above criticisms of it. In view of this it seems to us worthwhile to have a clear and as simple as possible explanation of the logical difficulties associated with Einstein's 1905 derivation, and it is to this end that this paper is written. Herewith we present a very simple treatment of the problem which makes absolutely clear the logical difficulties in Einstein's first published work on  $E = mc^2$ .

### KEYWORDS

History of Science; Origins of Special Relativity

### INTRODUCTION

Does Einstein's first paper<sup>1</sup> on  $E = mc^2$  suffer from the fallacy of circular reasoning? A circular argument, which in philosophical circles is frequently referred to as *petitio principii* or *circulus in probando*, is one that assumes what it is trying to prove. It inserts the conclusion into the premises, as in the simple example, "Jason is the best candidate for the position because Jason is better than all the other candidates. Therefore, Jason is the best candidate for the position." No one will argue that such argumentation is circular. So also, according to many notable scientists, such as Max Planck and the well-known historian of physics, Max Jammer, is Einstein's 1905 paper on  $E = mc^2$ .<sup>\*</sup> Unfortunately, this paper entitled "Does the Inertia of a body depend upon its energy content?" is referenced in scientific articles and textbooks on special relativity as gospel truth coming from the great scientist himself without any reference to the problems existing within it. Others try to defend the paper against the logical criticisms of the above mentioned scientists, however, none successfully, for to do such would necessarily have to refute the fallacy of circular reasoning from which we show quite clearly that Einstein's paper suffers. Most simply, as we show below, the error of circular reasoning in Einstein's paper can be understood from our **Equation 7'**, which relates the total energy of a particle in a moving frame to the total energy of a particle in its rest frame to order  $\left(\frac{v}{c}\right)^2$ . Einstein's argument essentially rests upon using a more

---

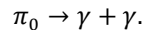
<sup>\*</sup>The list of authoritative figures associated with objections to Einstein's 1905 paper started with Max Planck, the father of the quantum theory. His criticism of Einstein's 1905 work is contained in an important 1907 paper by Planck, which some consider to contain the first generally valid and correct derivation of  $E = mc^2$  for matter.<sup>2</sup> Apparently Einstein himself was not very happy with his 1905 paper, and shortly afterwards he published another derivation of mass-energy equivalence.<sup>3</sup> That paper, according to Einstein, is basically a rewriting of a treatment of mass-energy equivalence for light given a few years earlier by Poincaré.<sup>4</sup> In 1952 the American physicist, Herbert Ives, wrote a particularly lucid account of the matter on which most subsequent authors base their analyses.<sup>5</sup> In particular, he spells out quite clearly the circular reasoning used in Einstein's 1905 paper. The noted philosopher and historian of physics, Max Jammer, reiterates Ives arguments in his book, *The Concept of Mass in Classical and Modern Physics*.<sup>2</sup> Other scientists and historians of science, such as Gerald Holton,<sup>6</sup> H. Arzeliés<sup>7</sup> and Arthur I. Miller<sup>8</sup> all reiterate these objections of Planck and Ives.

complicated form of **Equation 7'** to derive  $E = mc^2$ . However, as our analysis clearly shows, it turns out that  $E = mc^2$  is already implicit in **Equation 7'**. Thus the fallacy of circular reasoning.<sup>†</sup>

We were led to this problem by uncovering purported derivations of  $E = mc^2$  that one finds on the notoriously dangerous internet highway of false and misleading information. One can find on there all kinds of discussions of  $E = mc^2$  claiming to be scientific, but which essentially repeat Einstein's circular argumentation in one way or another, without any mention of the logical difficulties associated with it, or without any reference to the well-established claims that Einstein's paper suffers from such logical error. One of the worst is the "derivation" of  $E = mc^2$  posted by Henry Reich.<sup>14</sup> For many a keen student this situation must be a frustrating state of affairs: trying to logically understand the illogical. For indeed there is something wrong with Einstein's 1905 derivation! To this end, it seems worthwhile to have a concise and clear as possible explanation of Einstein's error, which is what we present here. Our argumentation is essentially the same as Ives' (and repeated by Jammer and others) except that we simplify things by considering a particular special and simple case of that considered in Einstein's paper, namely where the particle ceases to exist after it emits light isotropically in all directions, which, for the special situation considered by us, means emission of a light pulse in one direction along with another light pulse emitted in the opposite direction. This amounts to particle annihilation, something utterly unthinkable at the time in which Einstein wrote his paper, and it enables us to see very clearly the logical difficulties associated with Einstein's first paper on  $E = mc^2$ .

**EINSTEIN'S 1905 ANALYSIS OF  $E = mc^2$  APPLIED TO PION ANNIHILATION: A SIMPLIFIED TREATMENT SHOWING THE DIFFICULTIES WITH HIS ANALYSIS**

Einstein in **Reference 1** considers a body which at some time emits a light pulse in one direction and simultaneously an identical light pulse in the opposite direction. After the emission of the two light pulses the energy of the body is, by conservation of energy, diminished by an amount equal to the sum of the energies of the two light pulses. A most simple case of this situation is when the body ceases to exist after the emission of the light pulses. An elementary particle process which physically describes this case is neutral pion annihilation into two gamma rays (light pulses), described symbolically by the following reaction:



Here  $\gamma$  represents one of the gamma rays and  $\pi_0$  represents the neutral pion.

Consider the rest frame  $S_0$  of the pion before it decays into two photons. Call its energy  $E_0$  and let its mass be denoted by  $m$ . Its energy after the decay may be taken as zero, since it has ceased to exist. The combined energy of both of the emitted photons is  $E_\gamma$ . The energies and kinetic energies of both of the photons and of the pion before and after the decay are shown in **Table 1**. ( $\gamma + \gamma$  in the tables represents both photons going off in opposite directions.)

Now consider the situation from the point of view of an observer moving with speed  $v$  relative to the pion. The energies of the pion and photons are denoted with primes to distinguish them from the corresponding quantities in the rest frame  $S_0$ . The values of these quantities are shown in **Table 2**. In Einstein's paper the kinetic energy  $K'_0$  is denoted by  $K$  and the energy of radiation (which in our case is the energy of one of the photons) is denoted by  $L$ . Einstein uses the subscripts 0 and 1 to distinguish quantities in the  $S_0$  and  $S'_0$  frames, respectively. For the energy of the particle before the emission of radiation he uses the symbol  $E$  and he uses  $H$  to denote the energy of the particle after the emission of light.

$S_0$	Energy	Kinetic Energy
$\pi_0$ (before)	$E_0$	0
$\pi_0$ (after)	0	0
$\gamma + \gamma$	$E_\gamma$	0

**Table 1.** Values of Relevant Quantities in Rest Frame of Pion.

<sup>†</sup>It should be pointed out that Einstein gave other (mathematically correct) proofs of the equivalence of mass and energy in the following articles: *Annalen der Physik* **20** 627-633 (1906); *Annalen der Physik* **23** 371-384 (1907); *Bull. Amer. Math. Soc.* **41** 223-230 (1935). For an up-to-date discussion about attempts to understand the meaning of  $E = mc^2$  we refer the reader to the recent article by Hecht<sup>9</sup> which contains a useful and relatively complete bibliography on the subject including somewhat tenuous attempts to justify on physical grounds Einstein's circular reasoning argument in his paper.<sup>10</sup>

$S'_0$	Energy	Kinetic Energy
$\pi_0$ (before)	$E'_0$	$K'_0$
$\pi_0$ (after)	0	0
$\gamma + \gamma$	$E'_\gamma = \frac{E_\gamma}{\sqrt{1 - \frac{v^2}{c^2}}}$	0

Table 2. Values of Relevant Quantities in the Frame  $S'_0$ .

Clearly the energy of each of the photons in the  $S_0$  frame is  $\frac{1}{2}E_\gamma$ . Hence the total energy of both photons in  $S_0$  frame is  $E_\gamma$  as listed in Table 1. According to Einstein’s first equation in his paper, we have that

$$\frac{1}{2}E'_\gamma(\phi) = \frac{1}{2}E_\gamma \frac{1 - \frac{v}{c} \cos(\phi)}{\sqrt{1 - \frac{v^2}{c^2}}} \tag{Equation 1.}$$

represents the energy of a photon going off at an angle  $\phi$  with respect to the positive  $x$  axis when the particle is located at the center of the coordinate system (see Figure 1). Thus the combined energy of the two photons going off in opposite directions from one another along the  $x$  axis is, in the  $S'_0$  frame, given by:

$$E'_\gamma = \frac{1}{2}E'_\gamma(0) + \frac{1}{2}E'_\gamma(\pi) = \frac{1}{2}E_\gamma \frac{1 - \frac{v}{c} \cos(0)}{\sqrt{1 - \frac{v^2}{c^2}}} + \frac{1}{2}E_\gamma \frac{1 - \frac{v}{c} \cos(\pi)}{\sqrt{1 - \frac{v^2}{c^2}}} = \frac{E_\gamma}{\sqrt{1 - \frac{v^2}{c^2}}} \tag{Equation 2.}$$

Now we come to Einstein’s assumptions which, in his notation, are

$$H_0 - E_0 = K_0 + C \tag{Equation 3.}$$

$$H_1 - E_1 = K_1 + C \tag{Equation 4.}$$

Using these assumptions, Einstein is led to conclude that  $E_0 = mc^2$ . (Precisely, Einstein’s conclusion states: *If a body gives off energy  $L$  in the form of radiation, its mass diminishes by  $L/c^2$ .* Clearly, this statement amounts to the assertion that  $E_0 = mc^2$ , and even more so in our case, ours being a special case of Einstein’s treatment where the particle ceases to exist after the emission of radiant energy.)

For our case the second assumption (Equation 4) reads

$$0 - 0 = 0 + C \tag{Equation 4'.$$

which implies

$$C = 0 \tag{Equation 5.}$$

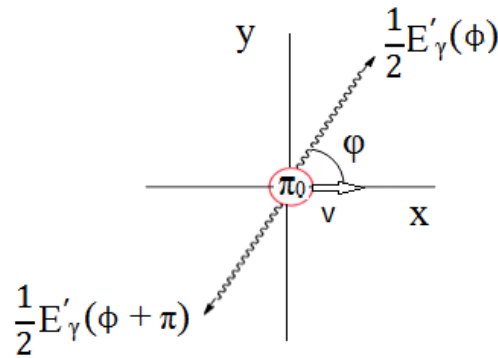


**Figure 1.** Pion decay, in the  $S'_0$  frame, showing two photons going off in opposite directions, the directions making angles  $\phi$  and  $\phi + \pi$  with respect to the positive  $x$  axis. (For the decay in the  $S_0$  frame, i.e. the rest frame of the pion, the figure looks the same except that  $v = 0$  and there are no primes on the  $E'_\gamma$ 's.)

The first of Einstein’s assumptions (**Equation 3**) in our notation then gives

$$E'_0 - E_0 = K'_0 + C = K'_0 \tag{Equation 6.}$$

since we have shown that  $C = 0$  for our simplified case. Thus

$$E'_0 = K'_0 + E_0 = K'_0 + E_\gamma \tag{Equation 7.}$$

since  $E_0 = E_\gamma$  by conservation of energy in the  $S_0$  frame. Hence, for our simple treatment, the constant  $C$  is zero and Einstein’s assumptions, **Equation 3** and **Equation 4**, amount to just one equation, namely **Equation 7**.

Now conservation of energy in the  $S'_0$  frame gives

$$E'_0 = \frac{E_\gamma}{\sqrt{1 - \frac{v^2}{c^2}}} \tag{Equation 8.}$$

Thus we obtain by using **Equation 7**

$$K'_0 = E_\gamma \left( \frac{1}{\sqrt{1 - \frac{v^2}{c^2}}} - 1 \right). \tag{Equation 9.}$$

This is, for our special case and in our notation, Einstein’s second to last equation of his paper. By expanding the term involving the radical as a power series in  $\frac{v}{c}$  to order  $\left(\frac{v}{c}\right)^2$ , we obtain as an approximation:

$$K'_0 = \frac{1}{2} \frac{E_\gamma}{c^2} v^2. \tag{Equation 10.}$$

This is, for our case and in our notation, Einstein’s last equation in his paper.

Let us see how Einstein was led to  $E_0 = mc^2$  out of **Equation 7** and **Equation 9**. For  $v \ll c$ ,  $K'_0$  must reduce to its nonrelativistic limit, so we have:

$$E'_0 = E_\gamma + K'_0 = E_\gamma + \frac{1}{2} m v^2 \text{ to order } \left(\frac{v}{c}\right)^2. \tag{Equation 7'}$$

Now expand **Equation 8** in powers of  $\left(\frac{v}{c}\right)^2$  to get:

$$E'_0 = E_\gamma + \frac{1}{2} \left( \frac{E_\gamma}{c^2} \right) v^2 \text{ to order } \left( \frac{v}{c} \right)^2 . \tag{Equation 11.}$$

Equating **Equation 7'** and **Equation 11** we obtain

$$m = \frac{E_\gamma}{c^2}. \tag{Equation 12.}$$

This is the argumentation used by Einstein in his paper and it enables him to conclude at the end of his paper what we stated above in italics, namely: *If a body gives off the energy L in the form of radiation, its mass diminishes by L/c<sup>2</sup>*. In summary, by using **Equation 7'** plus energy conservation, as did Einstein, we have been led to energy mass equivalence i.e. to  $E_0 = mc^2$ .

Finally we show the logical difficulties associated with Einstein's paper. Specifically we show that not only does **Equation 7'** together with energy conservation imply  $E_0 = mc^2$  but also  $E_0 = mc^2$  together with energy conservation implies **Equation 7'**. This means (assuming energy conservation) that the statement embodied by **Equation 7'**, i.e. the statement embodied by **Equation 7** to order  $\left(\frac{v}{c}\right)^2$ , is equivalent to the statement of  $E = mc^2$  and hence it cannot be used to derive  $E = mc^2$ . Let us now show that this is so. From **Equation 11** which comes from **Equation 8** which we were led to by conservation of energy, we obtain:

$$E'_0 = E_\gamma + \frac{1}{2} \left( \frac{E_\gamma}{c^2} \right) v^2 + \dots$$

On the other hand, we also have **Equation 7'** which is

$$E'_0 = E_\gamma + \frac{1}{2} m v^2 + \dots$$

Equating coefficients of the corresponding terms of degree  $v^2$  and using the fact that  $E_\gamma = E_0$  gives

$$E = mc^2$$

This shows that **Equation 7** to order  $\left(\frac{v}{c}\right)^2$  implies  $E_0 = mc^2$ . If this is all that we could show, then there would be no logical difficulties in Einstein's paper. But, in fact, as we have already stated above, more can be shown, namely that  $E_0 = mc^2$  implies **Equation 7** to order  $\left(\frac{v}{c}\right)^2$ , i.e. **Equation 7'**. Thus **Equation 7** to order  $\left(\frac{v}{c}\right)^2$  is logically equivalent to the statement of  $E = mc^2$  and hence it cannot be used to derive  $E = mc^2$ . This is what the young Einstein unfortunately neglected to realize in his paper.

We now show that  $E_0 = mc^2$  together with energy conservation implies **Equation 7'**. As before, we start with **Equation 11** which comes from **Equation 8** which we were led to by conservation of energy. We have:

$$E'_0 = E_\gamma + \frac{1}{2} \left( \frac{E_\gamma}{c^2} \right) v^2 + \dots$$

Combining  $E_\gamma = E_0$  (which comes from conservation of energy in the S frame) and  $E_0 = mc^2$  we obtain  $E_\gamma = mc^2$ . Using this in the second term of the above equation gives:

$$E'_0 = E_\gamma + \frac{1}{2} m v^2 + \dots$$

which is **Equation 7'**. Thus **Equation 7'** is equivalent to  $E_0 = mc^2$ .

**CONCLUSIONS**

From what we have shown in this paper, it seems clear that there can be no (mathematically correct) argumentation to obtain  $E = mc^2$  from considerations starting with a body emitting light isotropically in all directions as is done in **Reference 11**. That this is so, was essentially what Poincaré already pointed out in 1900 when he stated that in order to obtain the result ( $E = mc^2$ ) it is necessary to use a parabolic mirror in order to focus and send light in one direction.<sup>12</sup> It is thus advisable for teachers and

expositors on the subject to steer clear of Einstein's 1905 paper on  $E = mc^2$ , and instead to follow his 1906 paper, namely **Reference 3**, to explain the famous formula. This was the path followed by Max Born in his well-known book "Einstein's Theory of Relativity".<sup>13</sup> This book which is even suitable for high school students contains a lucid and quite elementary derivation of  $E = mc^2$  that is based on **Reference 3**. Born probably was well aware of the logical difficulties with the 1905 paper and thus avoided using it.

## REFERENCES

1. Albert Einstein (1905) Ist die Trägheit eines Körpers von seinem Energieinhalt Abhängig? *Annalen der Physik* 18, 639–641.
2. Max Jammer (1961) *The Concepts of Mass in Classical and Modern Physics*, pp 181, Harvard University Press.
3. Albert Einstein (1906), *Annalen der Physik* 20, 627–633.
4. Henri Poincaré (1900) *Archives Néerlandaises des sciences exactes et naturelles* 2, 252–278.
5. Herbert E. Ives (1952) *J. Opt. Soc. Am.* 42, 540–543.
6. G. Holton (1962) *Am. J. Phys.* 10, 462.
7. H. Arzeliés (1966) *Rayonnement et Dynamique du Corpuscule Chargé Fortement Accélééré*, 74–79, Gauthier-Villars, Paris.
8. A. I. Miller (1981) *Albert Einstein's Special Theory of Relativity: Emergence (1905) and Early Interpretation (1905-1911)*, 377, Addison-Wesley, Reading, MA.
9. Hecht, E. (2011) *Am. J. Phys.* 79 (6), 591–600.
10. Stachel, J., and Torretti, R. (1982) *Am. J. Phys.* 50 (8), 760–763.
11. Reich, H., Minute Physics, Einstein's Proof of  $E = mc^2$ , <https://www.youtube.com/watch?v=bW7DW9NIO9M> (accessed July 2015).
12. Henri Poincaré (1900) *Archives Néerlandaises des sciences exactes et naturelles* 2, page 260.
13. Max Born (1965) *Einstein's Theory of Relativity*, Dover, New York, 283-286.

## ABOUT THE STUDENT AUTHORS

James Lombardi is a senior undergraduate student in Computer Engineering at The Pennsylvania State University, University Park, PA USA. He enjoys reading about the latest news and research in physics and astronomy, as well as coding in C/C++ and Python. The experience that he gained while interning for ARRIS Group Inc. has provided him with a phenomenal opportunity to work at Oracle as a Cloud Engineer. His hobbies include weight lifting and playing soccer, and dreams of one day obtaining tickets to watch the World Cup Final in person.

Stephen Moylan is a senior undergraduate student in Physics at the Pennsylvania State University, University Park, PA USA. His research interests include general relativity and quantum mechanics. In the current 2015/2016 academic year he is studying French, mathematics and piano performance in Paris, France as part of the International Exchange of Scholars Program at the Pennsylvania State University. His hobbies include classical piano and reading literature.

## PRESS SUMMARY

It is a well-known and indisputable fact that Einstein's first paper on  $E = mc^2$ , published in 1905, is problematic in that it suffers from the error of circular reasoning. Despite this defect it is blindly referenced in many scientific articles as the official derivation of the famous formula. Furthermore, the arguments in that paper are still used today by some authors to purportedly derive  $E = mc^2$ . In view of this disturbing state of affairs, it seems worthwhile to have a clear and as elementary as possible explanation of the erroneous reasoning in Einstein's 1905 paper on  $E = mc^2$ .

# Aberrant *DNMT3B7* Expression Correlates to Age, Race, and Hormone Receptor Status in Breast Cancer Patients

Christian C.S. Mullin, Jennifer J. Busser, Anna M. Ciampanelli, and Stacey L. Raimondi\*

Department of Biology, Elmhurst College

Students: mullinc@net.elmhurst.edu, jennifer.j.busser@net.elmhurst.edu, ciampanellia@net.elmhurst.edu

Mentor: raimondis@elmhurst.edu\*

## ABSTRACT

Invasive breast cancer caused almost 40,000 deaths last year alone. Deciphering a way to better understand aggressive phenotypes of breast cancer could potentially provide a novel approach to increase the efficacy of breast cancer treatments. The aberrant gene *DNA methyltransferase 3B7*, *DNMT3B7*, has been observed in virtually all cancer types and has been shown to affect multiple facets of breast cancer progression including changes in cell adhesion, cellular proliferation, and anchorage-independent growth. A bioinformatics approach was taken to attempt to determine which clinical parameters are potentially altered by *DNMT3B7* expression in breast cancer patients. Clinical parameters including age at initial diagnosis, menopausal status, race, and the status of three hormone receptors — estrogen, progesterone, and human epidermal growth factor 2 (ER, PR, HER2, respectively) — were collected from The Cancer Genome Atlas (TCGA) and analyzed using T-tests and ANOVA. Our results show increased expression of the aberrant gene, *DNMT3B7*, is correlated with age at initial diagnosis, race, and hormone receptor status (ER negative, PR negative, and HER2 positive) in breast cancer patients, but not with menopausal status. Taken together, these data indicate that *DNMT3B7* expression may be an important marker in tumor progression.

## KEYWORDS

*DNMT3B7*, DNA Methylation; Bioinformatics; Breast Cancer; Tumor Progression; Estrogen Receptor; Progesterone Receptor; Human Epidermal Growth Factor Receptor 2

## INTRODUCTION

Cancer is the term used for a group of different diseases in which abnormal cells divide uncontrollably and may eventually progress to invade other bodily tissues.<sup>1</sup> The National Cancer Institute estimates that 39.6% of all men and women in the United States will develop cancer in their lifetime. Breast cancer is caused by abnormal cell growth in the tissues of the breast, specifically the glands (lobules) and ducts needed for milk production. This type of cancer caused almost 40,000 deaths last year alone, making it the second largest cause of cancer death among women.<sup>2</sup> Breast cancer that spreads to the rest of the breast is classified as invasive or infiltrating. Out of approximately 300,000 cases of breast cancer estimated last year, over 200,000 of those cases were infiltrating.<sup>2</sup> However, once spread to a different and unconnected part of the body, the cancer has metastasized. Metastasis is a more aggressive cancer phenotype because of the difficulty in targeting cancer cells as they move throughout the body. Unfortunately, the five year survival rate for metastatic cancer is only 24%, which is a significant drop from the 99% survival rate for women with cancer localized in only the breast.<sup>2</sup> Therefore, it is imperative that we understand the mechanisms by which breast cancer develops and progresses in order to develop better treatments in the future, especially for patients with invasive or metastatic tumors.

Of particular interest are the genetic factors that control the metastatic process.<sup>3</sup> The abnormal methylation of DNA can cause cells to become cancerous by altering expression of oncogenes and tumor suppressor genes.<sup>4</sup> DNA methyltransferase 3B, or *DNMT3B*, is one of the three main DNA methyltransferases that catalyze cytosine methylation in eukaryotic cells. It is a *de novo* methylase, which means that it is capable of methylating new sites,<sup>5</sup> and aberrant versions of *DNMT3B* have been found to be highly expressed in cancer cells.<sup>6,7</sup> *DNMT3B7* is an aberrant transcript formed through the retention of 94bp of intron 10, leading to an early stop codon and a truncated protein. It has been shown to methylate the promoter region of *CDH1/E-cadherin*<sup>6</sup> leading to the loss of E-cadherin expression, which is seen when tumors become more aggressive.<sup>8</sup> Furthermore, previous studies have shown that *DNMT3B7* promotes tumor progression to a more aggressive phenotype in breast cancer cells through changes in cell adhesion, proliferation, and anchorage-independent growth.<sup>8</sup> However, an analysis of the connection between *DNMT3B7* expression and clinical parameters has not been performed to date. Therefore, the purpose of this study was to determine which clinical

It has been shown that as age increases, the probability of getting cancer also increases.<sup>2</sup> The more cycles of replication of DNA, the more opportunities there are for a mutation to occur.<sup>9</sup> Incidence and mortality of breast cancer in women makes a steady climb until the late 70's and then levels off.<sup>2</sup> However, it is more likely for young women to be diagnosed with aggressive tumors that are faster growing, which makes early screening important.<sup>10,11</sup> Premenopausal women are more likely to have a more aggressive form of breast cancer while postmenopausal women have a greater risk of getting breast cancer due to the high endogenous estrogen or testosterone levels.<sup>12-14</sup> Women who started their menstrual cycle early or did not lose their menstrual cycle until later in life also have a greater risk of breast cancer thought to be caused by a longer exposure to reproductive hormones. For every year younger at first menstrual cycle, the risk of breast cancer increases by a factor of 1.05, and for every year older at menopause, the risk of breast cancer increases by a factor of 1.209.<sup>15, 16</sup>

Race is also a factor that is correlated with different five-year survival rates in breast cancer. It has been shown that African Americans have a five year survival rate that is on average about ten percent lower than whites.<sup>2, 17</sup> African American women tend to be diagnosed with a more aggressive disease at a higher rate (39%) compared to non-African American women of any age (16%).<sup>18</sup> Furthermore, premenopausal African American women have a smaller chance (36%) of being diagnosed with less aggressive tumors compared to non-African American women of any age (54%).<sup>18</sup> Therefore, African American women tend to have a higher rate of aggressive breast cancer and a lower rate of the less aggressive cancer type, which may correspond to their altered survival rates.

Breast cancer diagnosis and treatment regimens are based on the expression of three hormone receptors in patients: estrogen receptor (ER), progesterone receptor (PR) and the human epidermal growth factor receptor 2 (HER2). ER and PR are considered tumor suppressor genes, which code for proteins that cause an abnormal cell to stop dividing.<sup>19</sup> With regard to both receptors, it is better to be positive because having a positive status means that these tumor suppressor genes are functioning normally and can respond to targeted therapies.<sup>17</sup> Interestingly, recent studies have shown that ER and PR may be methylated in cancers leading to the loss of expression and more aggressive disease.<sup>19-22</sup> The HER2 gene codes for a protein that, when expressed at normal levels, promotes growth, division and repair of cells. However, if the HER2 gene is amplified, there will be too many HER2 receptors produced, causing cells to grow and divide abnormally. A positive HER2 status is correlated with aggressive breast cancer cells, and this occurs in approximately 20 to 30% of all breast cancers.<sup>23</sup>

Breast cancers are classified based on their expression of these three hormone receptors in one of the following categories, ordered by increasing aggressiveness: Luminal A (ER and/or PR positive, HER2-), Luminal B (ER and/or PR positive, HER2+), HER2 type (ER-, PR-, HER2+), and basal-like/triple negative breast cancer (TNBC; ER-, PR-, HER2-). The first three types can be treated by targeted therapies to the appropriate hormone receptor being expressed, which can lead to higher survival rates. However, in the case of TNBC, targeted therapies do not exist and, therefore, the only treatment option for patients is chemotherapy. Because of this, patients with TNBC typically have a lower survival rate and more aggressive disease.

*DNMT3B7* is correlated with a more aggressive cancer phenotype,<sup>8</sup> so expression of *DNMT3B7* should be greatest in cells that correspond with a clinical risk factor. In order to measure this, we analyzed data that were taken from The Cancer Genome Atlas (TCGA) where patients in clinical settings allowed disclosure of their age at initial diagnosis, menopausal status, race, and status of ER, PR, and HER2 receptors. Based on previous data indicating *DNMT3B7* correlates with tumor progression in breast cancer cells,<sup>8</sup> we hypothesize that the expression of *DNMT3B7* will be higher in patients with a more aggressive phenotype including those who are younger, premenopausal, African American, ER-negative, PR-negative, and HER2-positive.

## METHODS AND PROCEDURES

In order to study gene expression levels in breast cancer patients, we utilized the RNA sequencing (RNAseqV2) data from the breast invasive carcinoma (BRCA) database and all corresponding clinical parameters from The Cancer Genome Atlas (TCGA) data portal.<sup>8</sup> Briefly, data were processed utilizing a custom Python script to provide relative expression levels of the 94bp intron 10 sequence unique to *DNMT3B7*. *DNMT3B7* expression was measured as reads per kilobase million (RPKM) and analyzed to determine clinical correlations in 971 primary and metastatic breast cancer patient samples. Throughout this study, N values changed due to a lack of available data for one clinical parameter compared to another. The data from the TCGA were grouped into categories consisting of age at initial diagnosis, menopausal status, race, and expression of hormone receptors using TCGA headings when appropriate. *DNMT3B7*

expression was examined and statistical significance was determined by ANOVA or T-test using Sigma Plot. All data were graphed using box plots in which the bottom and top of the box represent the 25<sup>th</sup> and 75<sup>th</sup> percentiles of data, respectively. The line within the box indicates the median while the errors bars indicate 10<sup>th</sup> and 90<sup>th</sup> percentiles of the data. Finally, the filled dots represent all outliers. Statistical significance is indicated on the graphs, when relevant.

## RESULTS

### *Increased DNMT3B7 expression is observed in younger patients*

*DNMT3B7* expression was analyzed with specific age groups at the initial age of diagnosis of breast cancer. The test was done to determine if *DNMT3B7* expression is correlated with a more aggressive phenotype typically observed in younger women.<sup>10, 11</sup> The data obtained from the TCGA datasheet was sorted into age groupings of 25-55 and 56-90+ and the corresponding *DNMT3B7* expression value (measured by RPKM) was analyzed. These age groupings were designated based on the age at which women are more likely to be diagnosed with breast cancer.<sup>1</sup> There is a much higher likelihood of being diagnosed after age 55, so for the purposes of this analysis, we considered women diagnosed between 25 and 55 “young”. A Mann-Whitney Sum test revealed a statistically significant increase in *DNMT3B7* expression in younger patients compared to the older patients ( $P=0.032$ ; **Figure 1A**). Patients were then grouped in a narrower range of ages — by decade — to determine if changes in *DNMT3B7* expression were observed. An ANOVA test determined that the median values did not display a statistically significant difference (**Figure 1B**).

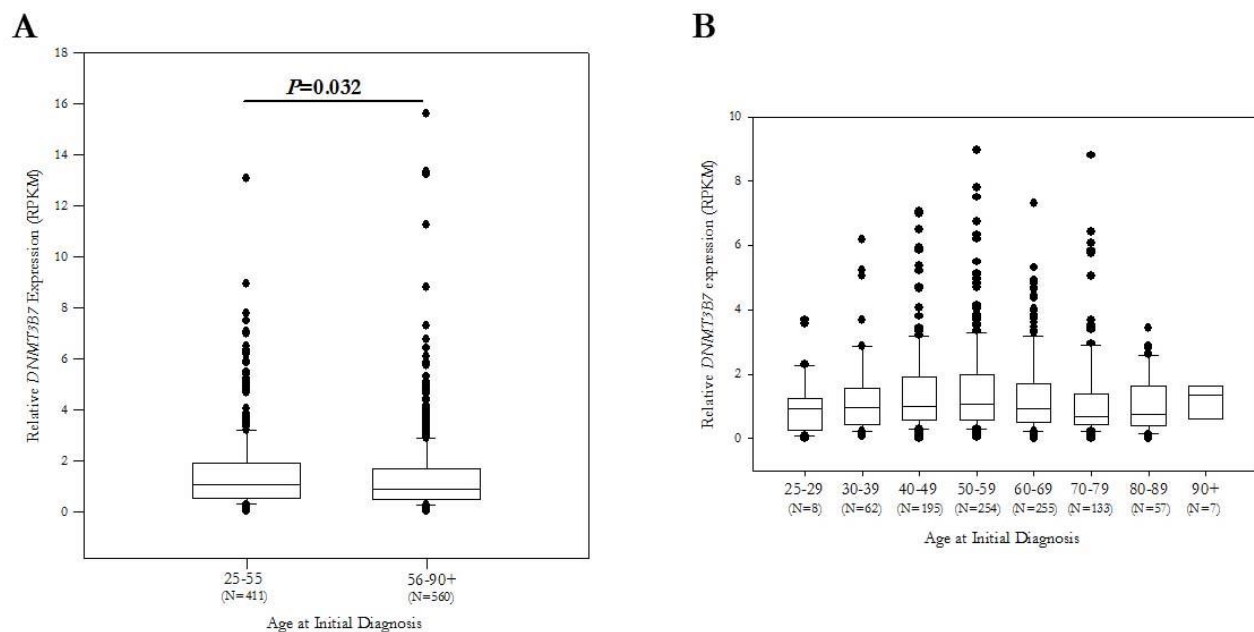


**Figure 1.** *DNMT3B7* expression is higher in younger patients. Patients with available age data were grouped (N for each group shown on graph) and *DNMT3B7* expression was measured as RPKM. **A**) Patients were grouped as either 25-55 (“young”) or 56-90+ (“old”). A Mann-Whitney Sum test indicated a significant difference between groups ( $p=0.032$ ). **B**) Patients were grouped by decade and an ANOVA on Ranks test was performed showing no significant difference in *DNMT3B7* expression between groups.

### *DNMT3B7 expression is not correlated with menopausal status*

Based on the results of our age analysis, above, we wanted to determine if *DNMT3B7* expression was altered based on menopausal status. To that end, all patients were grouped based on their menopausal status — pre-, peri-, and post — and *DNMT3B7* expression levels were compared. A Kruskal-Wallis ANOVA on Ranks test determined there was no statistically significant difference between the medians of pre-, peri-, and post-menopausal status (**Figure 2**).

### *African American women have higher DNMT3B7 expression.*

Because previous studies have shown that African American women typically present with a more aggressive breast tumor,<sup>18</sup> we analyzed *DNMT3B7* expression among races to see if there was a correlation. Patients were grouped by race — Caucasian/White, African American/Black, or Asian — and the corresponding *DNMT3B7* expression was measured. African American breast cancer patients had higher expression of *DNMT3B7* compared to their Caucasian counterparts ( $P=0.048$ ; **Figure 3**).

*DNMT3B7 expression correlates with a more aggressive receptor phenotype.*

DNMT3B7 expression was analyzed in comparison with ER, PR, and HER2 hormone receptor status. The data were extracted from the TCGA data sheet and separated into positive and negative receptor values in correspondence with DNMT3B7 expression. Examination of estrogen and progesterone receptor statuses indicated significantly increased expression of DNMT3B7 in ER- and PR- patients compared to ER+ and PR+ patients, respectively ( $P < 0.001$ ; **Figure 4A and 4B**). DNMT3B7 was also significantly increased in HER2+ patients compared to HER2- patients ( $P < 0.001$ ; **Figure 4C**). As previously stated, the loss of ER and PR, as well as amplification of HER2, correspond to a more aggressive phenotype.<sup>17,23</sup>

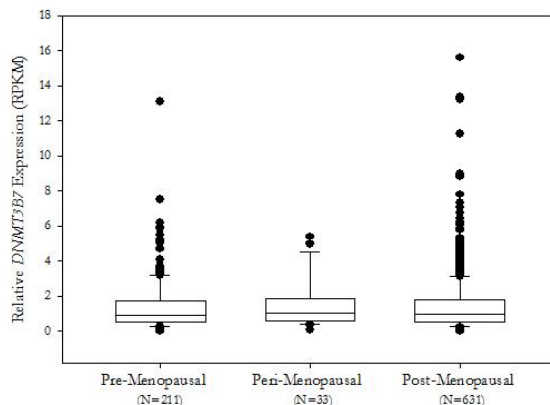


**Figure 2.** Menopausal status does not affect DNMT3B7 expression. Patients with available data indicating menopausal status (pre-menopause = <6 months since last menstruation; peri-menopause = 6-12 months since last menstruation; post-menopause = >12 months since last menstruation) were grouped based on TCGA headings (N for each group shown on graph) and DNMT3B7 expression was measured as RPKM. An ANOVA on Ranks test was performed and showed no significant difference between groups.

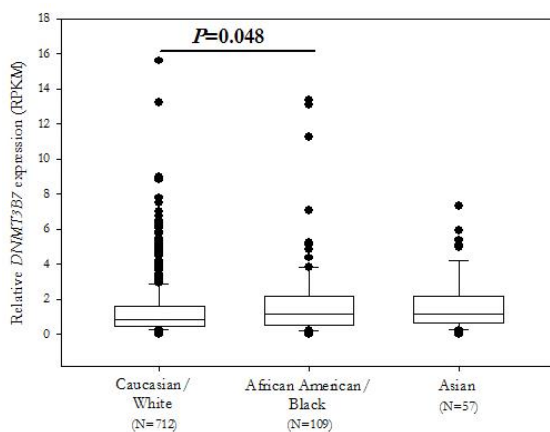


**Figure 3.** DNMT3B7 expression is increased in African Americans compared to Caucasians. Patients with available race information were grouped based on TCG headings (N for each group shown on graph) and DNMT3B7 expression was measured as RPKM. A t-test was performed between each group and significance is indicated on the graph.

*Examination of DNMT3B7 expression in comparison with race and hormone receptor status combined.*

Our previous results showed increased DNMT3B7 expression in African American women as well as women who were either ER-, PR-, or HER2+. Therefore, we wanted to examine DNMT3B7 expression when these clinical parameters were combined, as would be found in a realistic clinical setting. All patients for which race and all receptor status data were available were isolated and grouped as shown in **Table 1**. DNMT3B7 expression was measured as RPKM and means for all groups are indicated. An ANOVA on Ranks with a Tukey’s test between all groups showed a difference between African American TNBC women and Caucasian Luminal A ( $P < 0.001$ ) and between Asian HER2-type women and Caucasian Luminal A ( $P = 0.040$ ). No other groups showed any significant difference. Interestingly, we noticed a difference in the raw number of women diagnosed in each group, as shown in **Table 1**. Specifically, while Caucasian women made up 83% of the total population of all diagnosed patients in our sample with African Americans at 9% and Asians at 8%, African American women made up 20% of the population of women diagnosed with TNBC and Asian

women made up 26% of the HER2-type population. These data indicate that minority women are being diagnosed with the more aggressive forms of breast cancer at a much higher rate than their Caucasian counterparts.

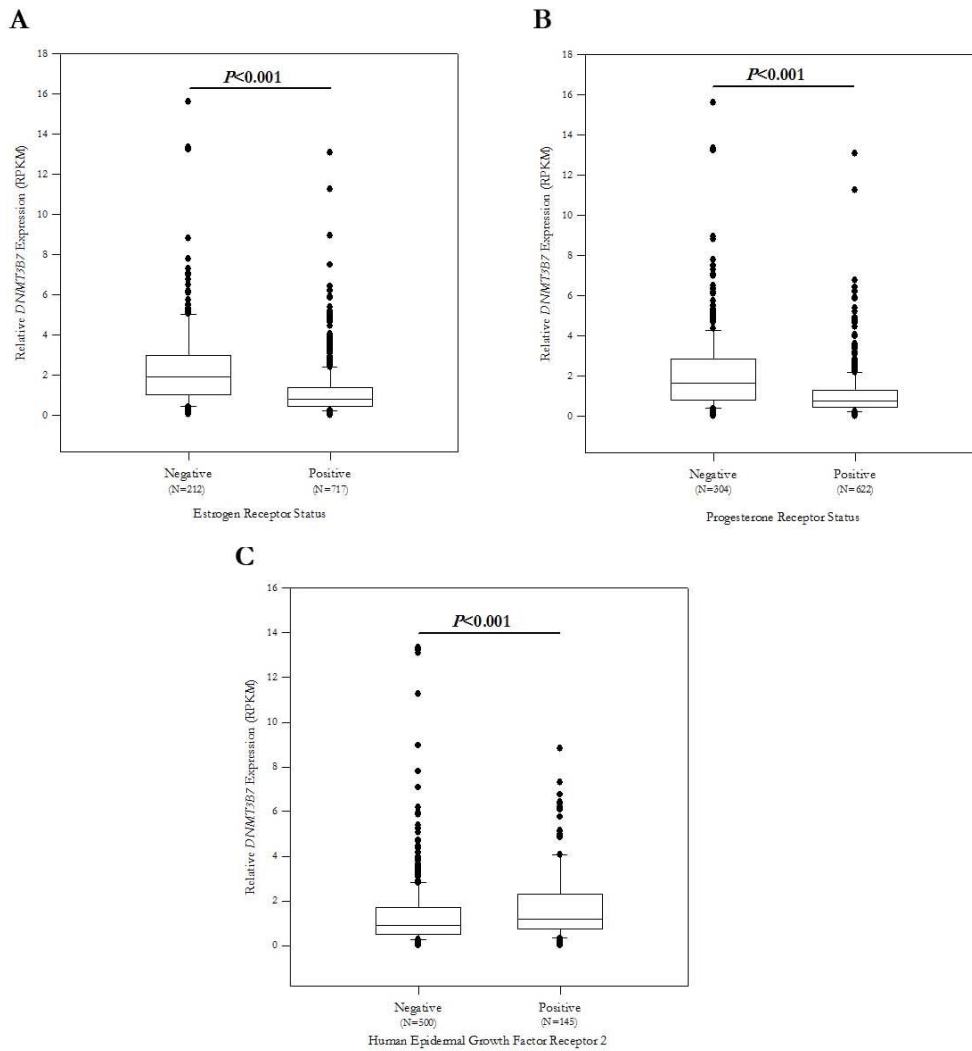


**Figure 4.** *DNMT3B7* expression is increased in ER-, PR-, and HER2+ patients. Patients with available hormone receptor information were grouped based on TCGA headings (N for each group shown on graph) and *DNMT3B7* expression was measured as RPKM. A Mann-Whitney Rank Sum test was performed between each group and significance is indicated on the appropriate graph. *DNMT3B7* expression is increased in **A)** ER- patients, **B)** PR- patients, and **C)** HER2+ patients, which corresponds to a more aggressive phenotype.

	Luminal A			Luminal B			HER2-type			TNBC			Total		
	Caucasian	African American	Asian	Caucasian	African American	Asian	Caucasian	African American	Asian	Caucasian	African American	Asian	Caucasian	African American	Asian
Mean RPKM	0.9709	2.025	1.375	1.502	1.577	1.114	2.644	2.052	2.841*	2.406	2.691**	1.808	1.349	1.804	1.644
N	296	25	21	76	3	5	19	4	8	67	19	8	458	51	42
% of total N for subgroup	86.55%	7.31%	6.14%	90.48%	3.57%	5.95%	61.29%	12.90%	25.81%	71.28%	20.21%	8.51%	83.12%	9.26%	7.62%

**Table 1.** Examination of a combination of race and hormone receptor status with regard to *DNMT3B7* expression (measured as RPKM) and raw number of patients diagnosed. Statistical significance compared to Caucasian Luminal A is indicated as \* ( $P=0.040$ ) or \*\* ( $P<0.001$ ).

## DISCUSSION

*DNMT3B7* has been shown to promote a more aggressive phenotype in breast cancer cells due to a combination of parameters including changes in cell adhesion, cellular proliferation, and anchorage-independent growth.<sup>8</sup> However, we still do not understand the clinical implications of *DNMT3B7* expression in breast cancer patients. The data described here examine broad clinical correlations between the expression of *DNMT3B7* with respect to age, menopausal status, and race, in addition to ER, PR, and HER2 receptor status. These results allow for a more comprehensive understanding of how *DNMT3B7* promotes tumor progression within breast cancer cells which may lead to better treatment and diagnosis of patients in a clinical setting.

In order to determine if *DNMT3B7* expression was correlated with age at diagnosis, **Figure 1** illustrates the dependence of the aberrant *DNMT3B7* with respect to the age of patients at initial diagnosis. Increased expression of *DNMT3B7* in the younger age bracket when compared to the older age bracket revealed statistically relevant data between the two groupings ( $P=0.032$ ; **Figure 1A**). It should be noted that the statistically significant data was seen in **Figure 1A**, which was separated into two age brackets for younger women (25-55 years old) and older women (56-90+). Conversely, when bracketing these same data off into decades, statistically significant data are not shown (**Figure 1B**). We believe the sampling number of the treatment groups was not great enough to provide a proper analysis of whether or not these data were statistically significant. Therefore, we have focused our analysis on **Figure 1A** because of the larger sample size in two groups in order to better understand the relevance between age at initial diagnosis and *DNMT3B7* expression. To support our findings, research has shown that younger women are more apt to develop an advanced stage of breast cancer that is fast growing and lacks estrogen receptors (ER-negative).<sup>10</sup> Furthermore, Hofvind and colleagues demonstrated that younger women develop faster proliferating breast cancers as compared to their older female counterparts and justify the need for earlier screening.<sup>11</sup> This supports the idea that more aggressive phenotypes are seen in younger females than older females and thus supports our claim that higher expression of *DNMT3B7* should be seen in young females.

Further, due to the fact that older females experience a lower ratio of aggressive phenotypes as compared to younger females as supported by **Figure 1A**, it should be expected that older women that have been through menopause would demonstrate decreased expression of *DNMT3B7* when compared to pre-menopausal women. This is not the case as illustrated by **Figure 2**. Menopausal status does not appear to correlate with the aberrant gene *DNMT3B7*, as the data show no statistical significance. These data do not exclude menopausal status as a potential player in the aggressive phenotypes of breast cancer, however it can be said that menopause is not a causative agent with respect to *DNMT3B7* expression in breast cancer patients based on **Figure 2**.

In addition to age and menopausal status, we examined the effect of race on *DNMT3B7* expression in tumorigenic patients. Our results show that aberrant *DNMT3B7* is expressed in Black or African American patients at higher levels than both Asian and White patients (**Figure 3**). This could be due to a multitude of factors. One study suggests that although breast cancer mammography has increased the efficacy of treatment exponentially, it has reduced breast cancer deaths more so in Caucasian or White women as compared to Black or African American women.<sup>25</sup> They claim that this slower decrease in death rate amongst the African American population is due to the accessibility of technological advancements and is linked to the socioeconomic status of the majority of the African American female population.<sup>25</sup> Unfortunately, the information provided in TCGA does not allow us to examine this possibility in our study. It has been documented that Black or African American women show a 12.9% decrease in survival differences when compared to White women in a 5-year study.<sup>25</sup> Additionally, the Black or African American population had a lower survival rate that was unchanged from 1991 to 2005 ( $P$ -value  $< 0.001$ ).<sup>18</sup> Treatment was a factor in the decreased survival rate of African American women, however, only 0.81% of the 12.9% accounted for these data. The treatment plan was thus ruled out as the main contributing factor of the survival difference. Interestingly, the presentation differences at diagnosis were deemed to be of utmost importance in linking race to breast cancer survival, which may correlate with our findings here indicating increased *DNMT3B7* expression.<sup>26</sup> African American women appear to have a higher incidence of TNBC and decreased survival rate when compared to their White or Caucasian counterparts.<sup>26</sup> These results were recapitulated in our own study (**Table 1**) and indicate an area of further study. Our laboratory has previously shown that *DNMT3B7* expression is increased in TNBC patients therefore it is imperative that we understand the mechanism by which this aberrant gene is functioning with regard to this clinical parameter.<sup>8</sup>

To better understand the role of *DNMT3B7* expression in TNBC patients, we compared PR, ER, and HER2 receptor status with respect to the aberrant *DNMT3B7* gene. **Figure 4** elucidates that all three of the receptors (ER, PR, HER2) show statistical significance denoting that the aberrant gene *DNMT3B7* is involved in the regulation of these specific receptors found in breast cancer patients. Breast tumors lacking a functioning estrogen receptor, ER- tumors, are known

to have poor prognoses as well as resistance to endocrine hormone therapies. Previous studies have shown that the ER-phenotype may be caused by abnormal DNA methylation.<sup>27</sup> Specifically, Martínez-Galán and associates have found that the estrogen receptor 1 gene, *ESR1*, is hypermethylated in tumor cells and correlated with the ER- status in patients.<sup>27</sup> This coincides with the function of a *de novo* methylase, like *DNMT3B7*, which can methylate specific sites and is capable of silencing tumor suppressor genes like the endocrine receptors via hypermethylation.<sup>19-21</sup> Taken together, the fact that *DNMT3B7* is highly expressed within ER- patients, and has the ability to methylate new sites, leads to the possibility that *DNMT3B7* could hypermethylate *ESR1* and consequently down-regulate ER in breast cancer patients. Methylation studies of the promoter region of *ESR1* in cells with and without *DNMT3B7* will be performed in the future to investigate the correlation between the *ESR1* pathway and *DNMT3B7*.

Progesterone receptors were thought to always associate with estrogen receptors due to the fact that progesterone receptors are estrogen-induced. It is now understood that PR-negative phenotypes can arise from multiple mechanisms, which include hypermethylation of the PR promoter and loss of heterozygosity of the PR gene.<sup>22</sup> Similar to ER, it is possible that *DNMT3B7* is methylating PR in breast cancer cells, leading to a more aggressive phenotype, and future studies will examine this relationship.

Conversely, HER2-positive phenotypes are also linked to the aberrant *DNMT3B7* gene as shown by **Figure 4C**. It is widely known that the HER family is composed of tyrosine kinases that are involved in intracellular communication cascades that regulate cell survival, cell proliferation, and migration.<sup>28,29</sup> Because *DNMT3B7* has been previously shown to promote cell proliferation,<sup>8</sup> it is possible that *DNMT3B7* and HER2 are operating through the same signaling pathway to promote tumor progression. Furthermore, HER2+ and ER- statuses have been linked together in the HER2 tyrosine kinase pathway.<sup>30</sup> An overexpression of HER2 (HER2+) associates with an ER- phenotype in breast cancer patients, which would aid in linking *DNMT3B7* to the two receptors. Additionally, studies have shown that loss of PR is correlated with a HER2+ phenotype.<sup>31</sup> Therefore, it is possible that *DNMT3B7* is methylating ER and/or PR in breast cancer cells and the loss of these receptors leads to increased HER2 expression. Taken together, this information allows us to believe that *DNMT3B7* is likely to be involved in crosstalk between the receptors leading to aggressive phenotypes.

## CONCLUSIONS

In summation, the aberrant gene, *DNMT3B7*, has been previously found to be highly expressed and linked to aggressive phenotypes in breast cancer cells.<sup>8</sup> By comparing the given parameters of age, menopausal status, race, and receptor statuses of ER, PR, and HER2, respectively, this study has allowed for a more comprehensive understanding of what was being affected by the aberrant gene *DNMT3B7* in a clinical setting. Understanding the big picture of how the aberrant gene interacts with each of these parameters could aid in leading to better and more effective treatment regimens for aggressive breast cancer phenotypes in the future.

## ACKNOWLEDGEMENTS

This work was supported by funds from the Ellen Marks Cancer Foundation (SLR) and the Center for Scholarship and Teaching at Elmhurst College (SLR).

## REFERENCES

1. National Cancer Institute. Cancer. <http://www.cancer.gov> (accessed Nov 2014)
2. American Cancer Society, Inc. Breast Cancer Facts and Figures. <http://www.cancer.org> (accessed Nov 2014)
3. Nguyen, D., Massague, J. (2007) Genetic determinants of cancer metastasis, *Nature Rev Genet* 8, 341–352.
4. Jones, P. (1996) DNA methylation errors and cancer, *Cancer Res* 56, 2463–2467.
5. Pawlak M., Jaenisch R. (2011) De novo DNA methylation by DNMT3A and DNMT3B is dispensable for nuclear reprogramming of somatic cells to a pluripotent state, *Genes Dev* 25(1), 1035–1040.
6. Ostler, K.R., Davis, E.M., Payne, S.L., Gosalia, B.B., Exposito-Cespedes, J., Le Beau, M.M., Godley, L.A. (2007) Cancer cells express aberrant DNMT3B transcripts encoding truncated proteins, *Oncogene* 26, 5553–5563.
7. Ostler, K.R., Yang, Q., Looney, T.J., Zhang, L., Vasanthakumar, A., Tian, Y., Kocherginsky, M., Raimondi, S., Demaio, J., Salwen, H., Gu, S., Chlenski, A., Naranjo, A., Gill, A., Peddinti, R., Lahn, B., Cohn, S., Godley, L. (2012) Truncated DNMT3B isoform DNMT3B7 suppresses growth, induces differentiation, and alters DNA methylation in human neuroblastoma, *Cancer Res* 72, 4714–4723.
8. Brambert, P.R., Kelsch, D.J., Hameed, R., Desai, C., Calafiore, G., Godley, L.A., Raimondi, S.L. (2015) DNMT3B7 expression promotes tumor progression to a more aggressive phenotype in breast cancer cells, *PLoS ONE* 10(1), e0117310.

9. Venkitaraman, A. (2000) The breast cancer susceptibility gene, BRCA2: At the crossroads between DNA replication and recombination? *Phil Trans: Biol Sciences* 355(1394), 191–198.
10. Freedman R.A., Partridge, A.H. (2013) Management of breast cancer in very young women, *Breast* 22 Suppl 2, S176–S179.
11. Hofvind, S., Vacek, P.M., Skelly, J., Weaver, D.L., Geller, B.M. (2008) Comparing screening mammography for early breast cancer detection in Vermont and Norway, *JNCI J Natl Cancer Inst* 100(15), 1082–1091.
12. Fuhrman, B., Schairer, C., Gail, M., Boyd-Morin, J., Xu, X., Sue, L., Buys, S., Isaacs, C., Keefer, L., Veenstra, T., Berg, C., Hoover, R., Ziegler, R. (2012) Estrogen metabolism and risk of breast cancer in postmenopausal women, *J Natl Cancer Inst* 104(4), 326–339.
13. Key, T. (2011) Endogenous oestrogens and breast cancer risk in premenopausal and postmenopausal women, *Steroids* 76(8), 812–815.
14. Hankinson, S. and Eliassen, A. (2007) Endogenous estrogen, testosterone and progesterone levels in relation to breast cancer risk, *J Steroid Biochem Mol Biol* 106(1-5), 24–30.
15. Kelsey, J., Gammon, M., John, E. (1993) Reproductive factors and breast cancer, *Epidemiol Rev* 15(1), 36–47.
16. Collaborative Group on Hormonal Factors in Breast Cancer. (2012) Menarche, menopause, and breast cancer risk: individual participant meta-analysis, including 118 964 women with breast cancer from 117 epidemiological studies, *Lancet Oncol* 13(11), 1141–1151.
17. Chevarley, F., White, E. (1997) Recent trends in breast cancer mortality among white and black US women, *Am J Public Health* 87(5), 775–781.
18. Carey, L. A., Perou C.M., Livasy, C.A., Dressler, L.G., Cowan, D., Conway, K., Karaca, G., Troester, M.A., Tse, C.K., Edmiston, S., Deming, S.L., Geradts, J., Cheang, M.C., Nielson, T.O., Moorman, P.G., Earp, H.S., Millikan, R.C. (2006) Race, breast cancer subtypes, and survival in the Carolina Breast Cancer Study, *JAMA* 295, 2492–2502.
19. Zhu, K., Williams, S. (1998) Methyl-deficient diets, methylated ER genes and breast cancer: A hypothesized association, *Cancer Causes & Control* 9(6), 615–620.
20. Mostoslavsky, R., Bergman, Y. (1997) DNA methylation: regulation of gene expression and role in the immune system, *Biochim Biophys Acta* 1333, 29–50.
21. Issa, J., Zehnauer, B., Civin, C., Collector, M., Sharkis, S., Davidson, N., Kaufmann, S., Baylin, S. (1996) The estrogen receptor CpG island is methylated in most hematopoietic neoplasms, *Cancer Res* 56, 973–977.
22. Lapidus R.G., Ferguson A.T., Otaviano Y.L., Parl F.F., Smith S.B., Weitzman S.A., Baylin S.B., Isa J.J., Davidson N.E. (1996) Methylation of estrogen and progesterone receptor gene 5' CpG islands correlates with lack of estrogen and progesterone receptor gene expression in breast tumors, *Clin Cancer Res* 2, 805–810.
23. Engel, R., Kaklamani, V. (2007) HER2-positive breast cancer, *Drugs* 67(9), 1329–1341.
24. DeSantis, C., Jemal, A., Ward E., Thun, M.J. (2008) Temporal trends in breast cancer mortality by state and race, *Cancer Causes Control* 19, 537–545.
25. Sibley, J.H., Rosenbaum, P.R., Clark, A.S., Giantonio, B.J., Ross, R.N., Teng, Y., Wang, M., Niknam, B.A., Ludwig, J.M., Wang, W., Even-Shoshan, O., Fox, K.R. (2013) Characteristics associated with differences in survival among black and white women with breast cancer, *JAMA* 310(4), 389–397.
26. Veer, L.J., Dai, H., Van de Vijver, M., He, Y., Hart, A., Maro, M., Peterse, H., Van der Kooy, K., Marton, M., Witteveen, A., Schreiber, G., Kerkhoven, R., Roberts, C., Linsley, P., Bernards, R., Friend, S. (2002) Gene expression profiling predicts clinical outcome of breast cancer, *Nature* 415, 530–536.
27. Martínez-Galán, J., Torres-Torres, B., Núñez, M.I., López-Peñalver, J., Del Moral, R., Ruiz De Almodóvar, J.M., Menjón, S., Concha, Á., Chamorro, C., Ríos, S., Delgado, J.R. (2014) *ESR1* gene promoter region methylation in free circulating DNA and its correlation with estrogen receptor protein expression in tumor tissue in breast cancer patients, *BMC Cancer* 14, 59.
28. Yarden, Y., Sliwkowski, M.X. (2001) Untangling the ErbB signaling network, *Nat Rev Mol Cell Biol* 2(2), 127–137.
29. Fink, M.Y., Chipuk, J.E. (2013) Survival of HER2-positive breast cancer cells: Receptor signaling to apoptotic control centers, *Genes Cancer* 4(5-6), 187–195.
30. Pietras R.J., Arboleda J., Reese D.M., Wongvipat, N., Pegram, M.D., Ramos, L., Gorman, C.M., Parker, M.G., Sliwkowski, M.X., Slamon, D.J. (1995) HER-2 tyrosine kinase pathway targets estrogen receptor and promotes hormone-independent growth in human breast cancer cells, *Oncogene* 10, 2435–2446.
31. Kim H.J., Cui, X., Hilsenbeck S.G., Lee, A.V. (2006) Progesterone receptor loss correlates with human epidermal growth factor receptor 2 overexpression in estrogen receptor-positive breast cancer, *Clin Cancer Res* 12(3pt2), 1013s–1018s.

**ABOUT THE STUDENT AUTHORS**

Christian Mullin graduated from Elmhurst College in May of 2015 with a Bachelor of Science (BS) degree in Biology and a minor in Chemistry. He is currently applying to dental schools.

Jennifer Busser is currently enrolled at Elmhurst College and is working towards graduating with a Bachelor of Science degree in Biology with minors in Chemistry and Medical Humanities in May of 2016. She plans on attending Podiatry School after graduation.

Anna Ciampanelli graduated from Elmhurst College in May 2015 with a Bachelor of Science degree in Biology and a minor in Chemistry. She hopes to attend PA school in the future.

**PRESS SUMMARY**

Invasive breast cancer caused almost 40,000 deaths last year alone. When breast cancer progresses to a more advanced stage, it can be due to a multitude of factors, one of which is epigenetic changes. DNA methylation is an example of an epigenetic change in which a methyl group is added to DNA leading to altered gene expression. Our research focuses on the aberrant DNA methyltransferase, *DNMT3B7*, which is capable of methylating new sites that have not been previously methylated. Prior research has shown that expression of *DNMT3B7* can turn off important genes that are needed to combat cancerous cells and promotes tumor progression to an aggressive state. However, the effect of *DNMT3B7* expression on clinical parameters was not known. The objective of our research was to analyze data from breast cancer patient samples available in The Cancer Genome Atlas database and attempt to correlate these clinical parameters to *DNMT3B7* expression. Our data demonstrate that increased expression of *DNMT3B7* correlates to age, race, and hormone receptor status. These findings have the potential to lead to better diagnosis and improved treatment regimens in the future.



# Numerical Prediction of Microbubble Attachment in Biological Flows

Joshua Gosney\* and Jeffrey J. Heys

Department of Chemical and Biological Engineering, Montana State University, Bozeman, MT

Student: joshgosney@gmail.com\*

Mentor: jeffrey.heys@coe.montana.edu

## ABSTRACT

Biofilm infections pose a major threat to human health and are difficult to detect. Microbubbles provide an effective and inexpensive method of detection for biofilm-based infections and other diseases such as cancer. The approach studied here examines the potential of targeted microbubbles, with specific antibodies covalently linked to their surfaces for use as ultrasound contrast agents and drug delivery vehicle. This work presents a novel numerical model for estimating the forces on microbubble conjugates in the vascular system. A full computational fluid dynamics simulation of biological fluid flow and the resulting forces on attached microbubbles is presented as well as comparisons with simplified analytical models. Both the computational and analytical predictions are compared with experimental measurements from Takalkar *et al.* and Schmidt *et al.*, and these comparisons indicate stable microbubble attachment can be anticipated when the total hydrodynamic force on the microbubble is less than 100 pN. Through the examination of typical biological flows, microbubble attachment can be expected up to an average fluid velocity of  $0.025 \frac{\text{cm}}{\text{s}}$  near the microbubble (i.e., a particle Reynolds number on the order of .001). The Stokes drag law was shown to predict the drag force (the dominant force) on the microbubble within an order of magnitude of the force predicted by the numerical model. Finally, it was found that the lift force on a microbubble was small relative to the drag force, and that the Saffman equation prediction differed from the numerical model by more than an order of magnitude for the biological flows examined.

## KEYWORDS

Microbubble Attachment; Ultrasound Contrast Agent; Hydrodynamic Force; Computational Fluid Dynamics

## INTRODUCTION

The NIH estimates that 80% of all microbial infections are biofilms,<sup>1</sup> which pose a significant threat to human health. The additional expenditures caused by biofilm infections are estimated to be \$0.3-\$2.3 billion a year.<sup>2,3</sup> The current method for determining the presence of a biofilm-based infection on a medical device or tissue is via microscopy through the use of a scanning electron or optical microscope. While highly accurate, this method of detection is very invasive, usually requiring the removal and destruction of an implanted device or tissue. In a study done by Passerini,<sup>4</sup> 81% of indwelling catheters showed evidence of a biofilm on the surface of the device, but a site swab taken at the dermal entry point only detected bacteria 6% of the time. A potential alternative approach, recently demonstrated through an *in vitro* experiment,<sup>5</sup> utilizes targeted microbubbles as a contrast agent for detecting and imaging biofilm infections. This method of detection would be limited to the outside surface of the catheter as a large acoustic impedance mismatch would disrupt detection of biofilms on the inner catheter surface. The microbubbles bind to the biofilm due to antibodies that are bound to their surface, and the microbubbles are imaged using ultrasound due to the density difference between biological fluids and the gas filled microbubbles. The potential advantages of this system for the detection of biofilm infections include lower costs, avoiding invasive medical device removal, and the potential for earlier biofilm detection.

These same microbubbles targeted at the biofilm could also potentially be used as a treatment delivery platform. Experiments conducted *in vivo* have shown that microbubble destruction via sonication is both an effective delivery method for the delivery of therapy agents and microbubble rupture during sonication could be enough to break up the biofilm. Targeted drug delivery to a location adjacent to the targeted tissue is often sufficient because the therapeutic drugs are often capable of diffusing to the target cells and tissues.<sup>6,7</sup> Even without microbubbles, focused ultrasound energy can disrupt and fracture tissue or biofilms, a technique known as histotripsy.<sup>8,9</sup> For any of these treatments to be utilized, the biofilm must first be detected.

Conjugated microbubbles were first developed in the 1990s and have provided a new avenue for medical imaging that has not been available in the past.<sup>10-13</sup> The combination of ultrasound imaging techniques and targeted microbubbles is becoming more effective than ever before at detecting diseases that express a target that the microbubbles can bind.<sup>10, 11</sup> Persistent microbial infections, carcinomas, autoimmune disorders and amyloid plaques have proven to be difficult to detect and treat due to the toxicity and limited effectiveness of most current allopathic treatments.<sup>14</sup> A wide range of antibodies are commercially available that can be covalently linked to microbubbles and injected into the bloodstream to detect relevant disease targets and deliver therapeutic agents. For example, it has previously been shown that amyloid plaques could be targeted using biotinylated microbubbles<sup>11</sup>, squamous cell carcinomas can be targeted with Bleomycin microbubbles<sup>7</sup>, and microbubbles can be targeted to the regulatory receptors that cause Crohn's disease.<sup>15</sup> Targeted microbubbles have also been experimentally tested in a flow chamber with results indicating that microbubbles have a predictable, target specific attachment frequency that is a function of the flow rate.<sup>15-17</sup> The experiments conducted by Takalkar *et al.* involved flowing microbubbles targeted to P-selectin through a flow chamber with varying surface densities of P-selectin. The principle result of this paper was that attachment and microbubble accumulation depended strongly on the fluid shear stress and the density of target receptors. Schmidt *et al.* conducted a very similar experiment, using a NeutrAvidin-coated polystyrene substrate. The observations of this paper indicated that shear from the flow was a major factor in microbubble binding and reversible binding caused by low intensity ultrasound could disrupt binding events. Further, they showed high acoustic pressure could cause microbubble destruction and therapeutic agent delivery.

Contrast agent implementations have been researched for the detection and treatment of carcinomas and atherosclerotic plaque, but little research has been conducted on the detection of biofilm infections using microbubbles.<sup>12, 18-22</sup> Experiments have shown that microbubbles will bind specifically to *S. aureus* in a closed system, but no estimates have been made about the behavior and attachment potential for microbubbles under common biological flow conditions.

*There are two primary objectives for this work. The first objective is to develop a FEM model that estimates the hydrodynamic forces that a microbubble is exposed and validate the model by comparing its prediction of microbubble attachment to targets with experimental measurements of microbubble adhesion under specific, controlled flow conditions. The second objective is to extend the validated FEM model to examine the potential for microbubble attachment under various biological flow conditions.* Finally, the force obtained from the FEM-based numerical model are compared to simple analytical approximations of the force for isolated spheres in idealized fluid flow conditions. The environment of a microbubble in the body is somewhat different from where the analytical expressions are expect to be valid, but the FEM model is used to assess the potential accuracy of the simple, analytical approximation of the force for typical biological flows.

## METHODS AND PROCEDURES

For bovine serum albumin (BSA) shelled microbubbles, which are a commonly used type of microbubbles, the average shear modulus for the shell has been estimated to be in the range of **6.6 MPa** to **16.9 MPa**, depending on the microbubble diameter.<sup>23</sup> Based on this estimate and stress-strain calculations for a spherical shell, the microbubbles were assumed to be spherical and rigid for the flow conditions and forces of interest within this paper. The fluids were assumed to be incompressible, Newtonian fluids.

For the geometries and flows of interest here, the microbubbles are assumed to be attached to a surface, and the primary direction of flow is parallel to that surface. Under these conditions, only two components of the three-dimensional force vector were non-negligible: one component is parallel to the direction of flow (the drag force, **Figure 1**) and the other is perpendicular to the direction of flow and normal to the attached surface (the lift force). The buoyancy force was neglected as it is at least two orders of magnitude less than the other forces for normal microbubble sizes and under typical biological flow conditions of interest.

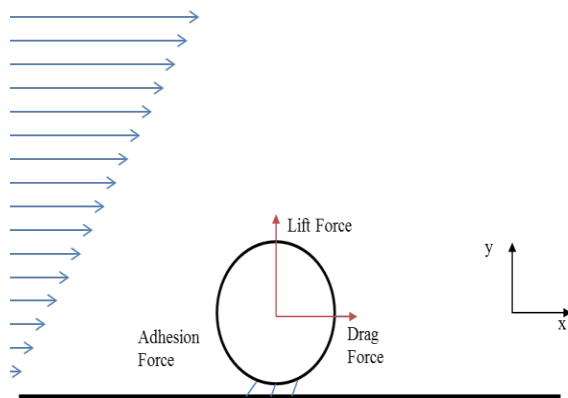


**Figure 1.** A microbubble attached to the surface and the forces of interest are shown in a linear flow field (not to scale).

Numerical Model

The main objective of this research is to develop a numerical model that estimates the force on a microbubble under various biological flow conditions and compare these estimates to the analytical model. The numerical studies were conducted using the finite element method to approximately solve the Navier-Stokes equations for incompressible flow.<sup>24</sup>

$$-\nabla p + \nabla \cdot \mu[(\nabla u + \nabla u^T)] = \rho(u \cdot \nabla u + \frac{\partial u}{\partial t}) \tag{Equation 1.}$$

$$\nabla \cdot u = 0 \tag{Equation 2.}$$

where  $u$  is the velocity vector,  $\mu$  is the viscosity,  $p$  is the pressure, and  $\rho$  is the density of the fluid.

The finite element method was used for the spatial discretization of the Navier-Stokes equations, and the mesh resolutions were varied from 88,762 – 325,000 mixed finite elements (Taylor-Hood tetrahedral elements). Grid continuation studies indicated that the forces on a sphere attached to the wall could be considered relatively (less than 2% change in the drag force with refinement) grid independent for these mesh resolutions as long as the microbubble had at least 3300 elements on its surface (i.e., the mesh had to be sufficiently refined near the microbubble). As the number of elements increased, the microbubble geometry was captured more accurately, and the grid continuation studies showed that the number of elements on the boundary of the microbubble was the most important factor in determining the numerical model accuracy.

Geometry	Dimensions	Average inflow velocity Particle Reynolds number	Domain/ microbubble size ratio
Parallel Plate <sup>16</sup>	0.6 mm x 8 mm	$V_{avg} = 0.2 \frac{cm}{s} \text{ to } 1.5 \frac{cm}{s}$ $Re_p = 0.00017 \text{ to } 0.0013$	215
Parallel Plate <sup>17</sup>	0.25mm x 3.5 mm	$V_{avg} = 0.0806 \frac{cm}{s} \text{ to } 0.4 \frac{cm}{s}$ $Re_p = 0.0001 \text{ to } 0.0008$	145
Capillary <sup>25</sup>	Diameter = 10 $\mu m$	$V_{peak} = 0.0001 \frac{cm}{s} \text{ to } 0.03 \frac{cm}{s}$ $Re_p = 1 \cdot 10^{-6} \text{ to } 1.8 \cdot 10^{-4}$	3
Venule <sup>25</sup>	Diameter = 100 $\mu m$	$V_{peak} = 0.1 \frac{cm}{s} \text{ to } 0.3 \frac{cm}{s}$ $Re_p = 2.7 \cdot 10^{-4} \text{ to } 8.4 \cdot 10^{-4}$	36
Vein <sup>25</sup>	Diameter = 1 mm	$V_{peak} = 1 \frac{cm}{s} \text{ to } 5 \frac{cm}{s}$ $Re_p = 1.5 \cdot 10^{-4} \text{ to } 7.3 \cdot 10^{-4}$	360

Table 1. Description of numerically assessed geometries and their flow rates.

Blood was assumed to be a Newtonian fluid with a density of 1040 kg/m<sup>3</sup> and a constant viscosity of 3.5x10<sup>-3</sup>kg/m/s. Blood is a suspension of cells and exhibits the behavior of a shear thinning fluid, but testing with a non-Newtonian blood flow model showed negligible deviation from the simpler Newtonian model for the flow rates and geometries described here so a Newtonian model was used. Flows with higher shear rates often require a non-Newtonian viscosity model for blood. Consistent with previous experimental results, the fluid in the model had the physical properties of PBS (phosphate buffered saline) with a

constant viscosity of  $1.05 \times 10^{-3} \text{ kg/m/s}$ . The forces on the microbubble were calculated by taking an approximate integral over the surface of the microbubble.

Two computational geometries were used in this study. A parallel plate flow channel geometry is used for comparison to previously published experimental results of Schmidt et al. and Takalkar et al., and the dimensions of the model domain match as closely as possible the flow channel used in those experiments (**Table 1**).<sup>16,17</sup> In addition, representative blood vessels including capillaries, veins and arteries were modeled using a straight, cylindrical geometry (**Table 1**). The length of the blood vessel sections used in the model ranged from 10 microns (capillaries) to 3 cm (vein) with internal diameters ranging from 10 microns (capillaries) to 1 mm (vein).<sup>25</sup> Thus, even the smallest diameter cylinders were larger than the typical microbubble diameter, which vary from 3.5 to 6 microns.

Large ranges of length scales were present in some problems where the ratio of the fluid domain size to microbubble diameter exceed 100. In these cases, it was impossible to generate a finite element mesh that was both computational feasible (i.e., did not require billions of elements) and did not contain invalid elements with negative Jacobians or extremely high aspect ratios. For these problems with a large range of length scales (i.e., for all problems where the total domain size to microbubble diameter ratio is greater than 100), a multi-scale modeling technique is employed to separate the larger length scales from the smaller length scales near the microbubble. When this technique is used, the larger fluid domain is modeled first without the microbubble explicitly included in the large length scale problem because it is significantly smaller than the individual elements. Then, after the larger length scale flow problem has been solved, the solution from the large scale problem is used to obtaining boundary conditions for the microbubble scale model, which only includes the fluid near the microbubble (i.e., the fluid within approximately 20 microbubble diameters of the center of the microbubble).

The boundary conditions for the parallel plate geometries are given in the experimental comparison section below. The capillary and venule simulations employed a range of flow rates (see **Table 1**), and boundary conditions were set based on a Poiseuille flow profile. Early simulations of flow in the larger blood vessels (vein) included the effects of wall elasticity and displacement on both the velocity gradients near the wall and the forces on the microbubble. These early results showed that the largest forces would be generated with a rigid wall, consistent the observations of others<sup>26</sup>, so all results shown below are based on the most difficult conditions for microbubble attachment: the rigid wall vessel.

#### Experimental Comparisons

The experimental measurements by others that are used here for numerical model validation were assumed to be at steady state with a fully developed flow profile. The fluid shear stress near the wall in the experimental channel can be calculated through the equation.<sup>16</sup>

$$Q = \frac{\tau h^2 w}{6\mu} \quad \text{Equation 3.}$$

where  $\tau$  is the wall shear stress,  $h$  is the channel height, and  $w$  is the channel width. The velocity in the mathematical model was set so that the wall shear stress matched the experimental wall shear stress values of 0.02, 0.05, 0.1 and 0.15 Pa.<sup>16</sup> The shear stresses for the second set of experiments by Takalkar *et al.* were 0.02, 0.03, 0.06, 0.1 and 0.17 Pa.<sup>17</sup> The channel height,  $h$ , was 0.6 and 0.254 mm for the Schmidt et al. and Takalkar *et al.* experiments, respectively, and since the channel width in both experiments was at least an order of magnitude greater than the height, a 2-dimensional model was used for the macro-scale fluid model. (A full 3-dimensional model was used for the micro-scale model of flow around the microbubble.) The boundary conditions used to simulate the experiments (i.e., the boundary conditions for the macro-scale model) include:

- no-slip ( $u = 0$ ) at the upper and lower walls,
- the normal stress in the normal direction is zero at the outlet, and
- tangential velocity of zero at the inlet and outlet.

For the micro-scale model, the solution from the macro-scale model was used to specify the velocity boundary conditions. The adhesion forces between the microbubbles and surfaces containing the targets were estimated based on previous Atomic force microscope (AFM) measurements and are used as a basis for comparisons between experiments and model predictions.<sup>27</sup>

*Analytical Models*

The drag force on a sphere in an infinite, uniform, creeping flow can be approximated by the well-known Stokes drag law equation:

$$F_D = 6\pi\mu V a \quad \text{Equation 4.}$$

where  $a$  is the radius of the microbubble,  $V$  is the characteristic velocity around the outer perimeter of the microbubble's surface, and  $\mu$  is the viscosity. The Stokes drag law assumptions include low Reynolds number flow ( $Re < 10$ ), no particle-particle interactions, and an infinite body of fluid around the spherical particle. The Reynolds number for this problem is defined as:

$Re = \frac{V \cdot L \cdot \rho}{\mu}$ , where  $V$  is characteristic velocity (defined as the mean fluid velocity),  $L$  is the characteristic length (the microbubble diameter unless otherwise specified), and  $\rho$  is the fluid density.<sup>7</sup>

The Saffman equation<sup>28</sup> can be used to estimate the lift force (i.e., the force perpendicular to the primary flow direction) on a spherical particle due to a velocity gradient:

$$F_L = KV a^2 \frac{k^{1/2}}{\nu^{1/2}} \quad \text{Equation 5.}$$

where  $\nu$  is the fluid's kinematic viscosity and  $k$  is the velocity gradient. Assumptions for the lift force estimate include symmetrical flow around the center of the sphere, and a semi-infinite body of fluid around the sphere, meaning that the microbubble should be surrounded by ample fluid on all sides.

**RESULTS AND DISCUSSION**

The numerical simulation results are divided into two sections: first the results of the parallel plate simulations are described and compared to previous experimental measurements, and then in the second section, the results of simulations in cylindrical blood vessel geometries are presented.

*Parallel Plate Simulations*

The first set of simulations was focused on the square channel geometry used in previous experimental observations to estimate the microbubble binding strength. **Figure 2** shows the drag force predicted by the numerical simulation for a range of Reynolds number in a geometry consistent with Schmidt *et al.* and Takalkar *et al.*<sup>16, 24</sup> The range of drag force values predicted by the model was from 14 to 100 pN for superficial velocities between  $0.2 \frac{cm}{s}$  and  $1.5 \frac{cm}{s}$ . Schmidt *et al.* observed microbubble detachment at a velocity of approximately  $1.5 \frac{cm}{s}$  for their flow cell, and the model predicts a drag force of 100 pN under these conditions.

Takalkar *et al.* showed a similar result, observing detachment at a superficial velocity of  $0.6 \frac{cm}{s}$ , corresponding to a drag force of 100 pN according to the model. Thus, based on the experiments of Takalkar *et al.* and Schmidt *et al.*, the model predicts microbubble attachment when the drag force is 100 pN or less, and no attachment when the drag force is greater than 100 pN.

Recent experiments have attempted to measure the total microbubble adhesion forces through the use of an atomic force microscope (AFM). These experiments showed a median adhesion force of 93 pN.<sup>27</sup> This result is consistent with the drag force estimate from the numerical simulation combined with flow cell measurements. Since the AFM measurements are believed to have measured the adhesion force of individual bonds, the implication is that each microbubble is primarily held in place by one or a few antibody bonds. This is intriguing since the surface density of the microbubbles has been estimated to be approximately 2500 antibodies per  $m^2$ ,<sup>17</sup> so there is the potential for multiple bonds between the microbubble and the target. However, the formation of many bonds would require a high density of receptors on the target and, if there were multiple bonds, their binding strengths are unlikely to be additive because just a few bonds would be expected to be under tension as described by Ward *et al.*<sup>29</sup> The drag force on the upper part of the microbubble furthest from the surface attachment bonds is likely to result in a 'peeling' or 'unzipping' of individual antibody bonds from each attachment sites.

*Blood Flow Simulations*

The second set of results is focused on predicting whether or not microbubble attachment is likely or unlikely for a range of blood vessel sizes and a range of blood flow velocities. The goal was to evaluate a sufficient range of vessel sizes and blood flow velocities to represent most of the conditions found in the cardiovascular system. The results are focused on predicting microbubble attachment in a "worst case" scenario and thus the model predictions of attachment may be conservative. The prediction of microbubble attachment is based on three regions of the vascular system: capillaries, venules, and veins.

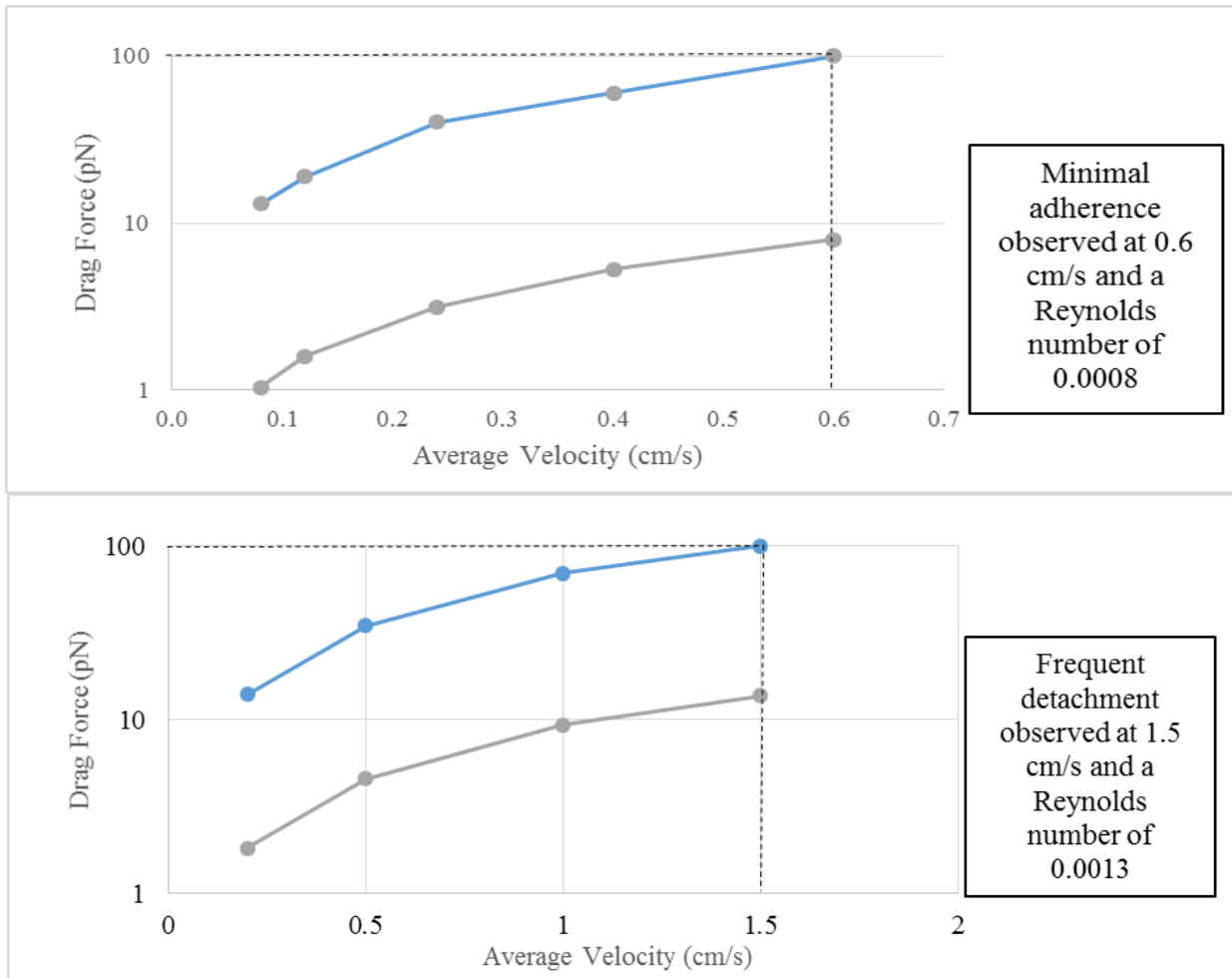


**Figure 2.** The numerical model predictions of drag force (blue) at different average velocities. The attachment/detachment of microbubbles based on experimental measurements by the Takalkar et al. (top) and Schmidt et al. (bottom) are indicated by the vertical dashed line. The Stokes drag law predictions of drag force are shown in gray. The model prediction of drag force combined with the experimental measurements of detachment suggest a drag force of 100 pN results in detachment.

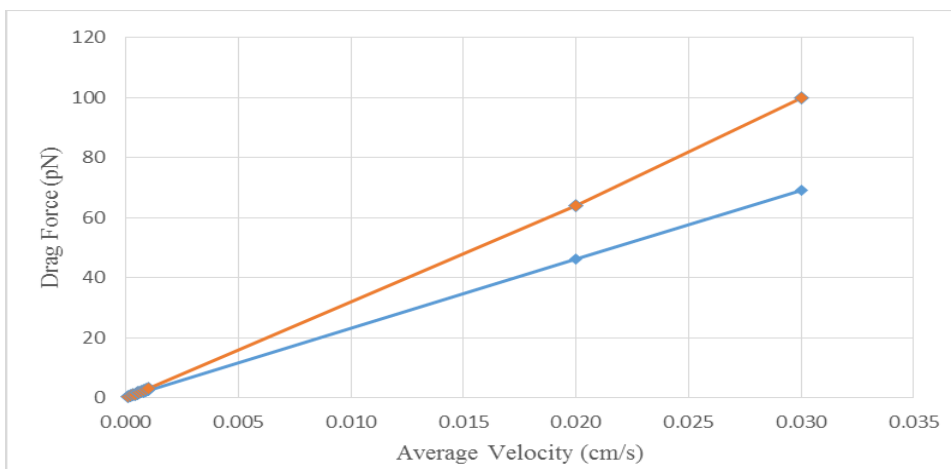


**Figure 3.** Numerical results (orange) from the capillary indicate that microbubbles should stay attached at all velocity. Stokes drag results (blue) are similar but diverge from the numerical results. This is most likely due the small capillary diameter to microbubble diameter ratio around .001

Additionally, these blood vessel results are compared with the predictions of the Stokes drag law. If the Stokes drag law results are consistent with the numerical model, it would allow for the use of simplified equations to predict microbubble behavior in a

wide range of flow conditions throughout the body without the use of computational modeling software. For all simulations, the microbubble is attached to the vessel wall and the hydrodynamic forces on the bubble are estimated.

The first vessel examined is the capillary geometry, and the force increases nearly linearly with the Reynolds number over the range of flow rates examined (Figure 3). Although the total hydrodynamic forces from fluid flow are unlikely to prevent attachment based for the typical range of velocities in the capillaries (i.e., the forces are less than 100 pN), the additional force from the impact of red blood cells, or other small particles could be significant and potentially lead to detachment. The force predictions from the Stokes drag law differed from the more accurate numerical simulation calculation of drag by no more than 50% at low Reynolds numbers ( $Re_c \ll 1$ ) found within capillaries. The agreement between the numerical simulation and Stokes drag law is somewhat unexpected because the Stokes drag law was derived using an infinite, unbounded body of fluid. As the flow rate increases in the capillary, however, a separation between the Stokes drag and numerical results is observed and is due to the acceleration of additional fluid through the space between the microbubble and opposing wall.

The second set of numerical results address forces on the microbubble in flow regimes similar to those found in venules. It can be seen once again that the forces increase approximately linearly with velocity. In flow regimes where the velocity is less than  $0.15 \frac{cm}{s}$ , microbubble adherence should be observed for this vessel, which has a much larger diameter than the capillary.

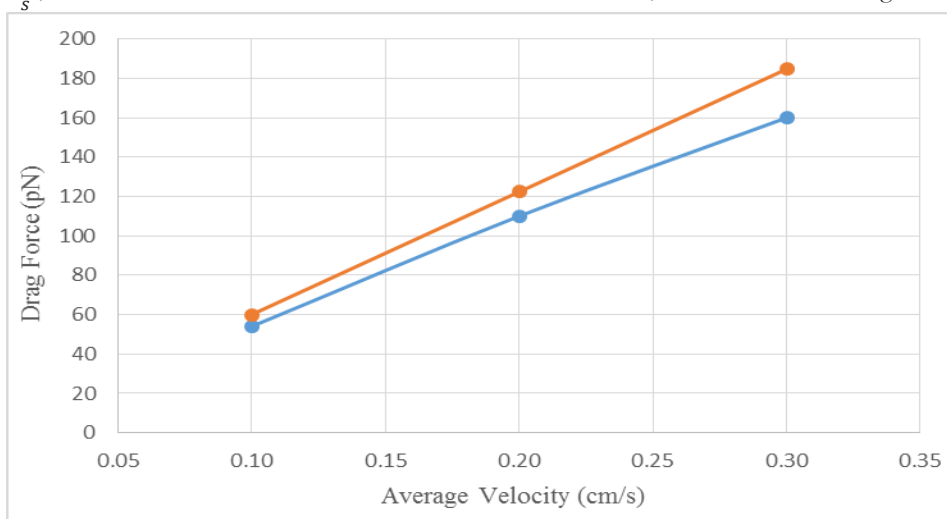


Figure 4. Numerical results in the Venuole flow regimes (orange) indicate that microbubble adherence is observed at velocities less than approximately 0.20 cm/s. The results also indicate that the Stokes drag (blue) is a relatively accurate approximation of the force within these regimes.

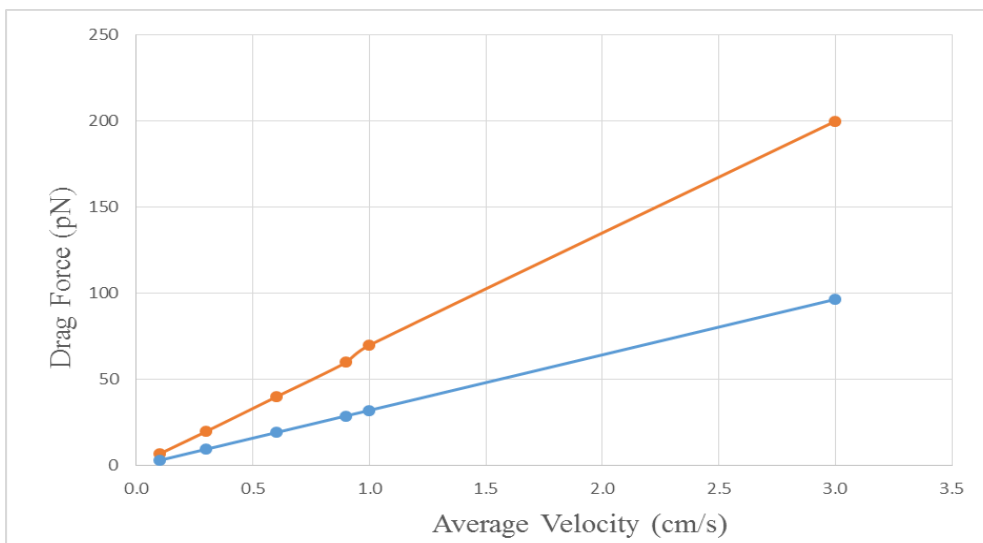
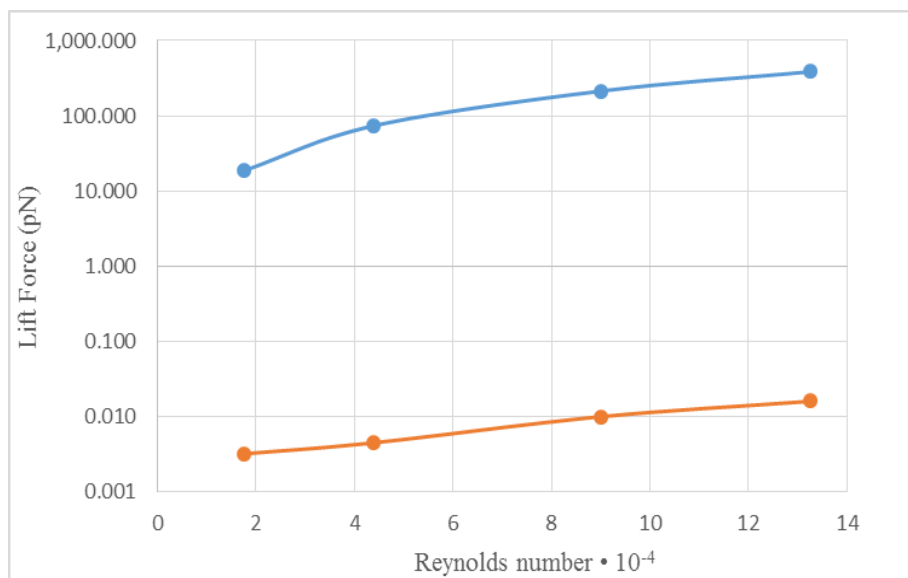


Figure 5. Numerical results from the vein flow regime (orange) indicate that microbubble attachment is observed at velocities less than 1.5 cm/s. Additionally a divergence from the Stokes drag law is observed, but the Stokes drag law was accurate within an order of magnitude for the flow regimes of interest.

Velocities above  $0.15 \frac{cm}{s}$  are predicted to result in frequent detachment and infrequent adherence of microbubbles. The microbubble is very small relative to the vessel size, so the microbubble is not directly in the flow path, but it does extend far enough into the main flow channel to be detached by the larger hydrodynamic forces away from the wall of the vessel. Unlike capillary flows, these vessels are much larger, so effects from red blood cells and other particles should be less pronounced. The Stokes drag law prediction of the drag force is similar to the numerical results in this regime, showing a variation of less than 10% between the two approximations (Figure 4).

The third and final set of numerical studies were conducted on the flow regimes typical for a vein. Because the microbubble is much smaller than the vein, these results were collected using the multi-scale modeling techniques described in the Methods section. The results indicate that the microbubble was likely to stay attached in areas where the average velocity in the vein was less than  $1.5 \frac{cm}{s}$  (Figure 5). By contrast, detachment is predicted in the much smaller venule at velocities above  $0.15 \frac{cm}{s}$ . This difference is not a surprising result because the microbubble is over 1000 times smaller than a vein, but only about 50 times smaller than a venule. In other words, the microbubble is a tiny fraction of the diameter of the vein and completely out of the main fluid flow. Additionally, increasing differences between the Stokes drag law force prediction and the numerical model were observed. This is partially because the Stokes drag law can only be considered accurate at Reynolds numbers much less than one. However, the Stokes drag law is still within a factor of 2 for the flow regimes of interest, making it a potentially useful tool for predicting the overall force on a microbubble.



**Figure 6.** The numerical lift force (orange), is much smaller than the lift force predicted by the Saffman equation. This is not a surprising result, as Saffman's equation of lift is only valid when the particle is very far from the wall.

The final goal of this work was to analyze the potential effectiveness of the Saffman equation (Equation 5) for predicting hydrodynamic lift forces on the microbubble. The Stokes drag law prediction of the drag force has already been discussed and is consistently less than the numerical model results. The Saffman equation for estimating the lift force was also compared to numerical results for all of the cases outlined. The Saffman equation predicted that the lift force was consistently the same order of magnitude as the drag force, but the numerical results indicated that this was not the case (Figure 6). For all of the problem geometries and flow rates of interest, it was found that the results from the Saffman equation for predicting the lift force were at least two orders of magnitude greater than the numerical results. The Saffman equation was derived based on the assumption that the particle was in an unbounded shear flow (far from the wall), and the violation of this assumption in the problems of interest probably leads to this difference. The numerical results indicated that the lift force on the microbubble could be considered negligible for all cases of interest, displaying a lift force that was at least one order of magnitude less than the drag forces.

## CONCLUSIONS

There were two primary objectives for this work. The first objective was to develop a numerical model of the forces on a microbubble in order to predict microbubble attachment/detachment, and then to validate the model based on previously published experimental measurements. The mathematical model predicted that the microbubble would adhere to its target unless it was exposed to forces greater than 100 pN. This result was consistent with AFM experiments with microbubbles that showed the median force of microbubble attachment is about 100 pN. The result suggests an unzipping effect, seen in other

experiments,<sup>29</sup> may be important when there are multiple bonds between the microbubble and the target surface, and this effect would allow multiple antibody bonds to rupture in a sequential manner. The second objective was to develop a numerical model to predict the potential for attachment of microbubbles in various flow conditions throughout the body. The principle result from this objective is that microbubble adhesion is predicted to occur in most capillaries, some venules and some veins, depending on the velocity (or Reynolds number) of the flow.

The numerical modeling results were compared to analytical equations that predict hydrodynamic forces on spherical particles. The results indicated that the lift force predicted by the Saffman equation did not agree with the numerical model predictions, primarily because the derivation of the equation was based on the assumption that the spherical particle was in an unbounded flow (far from the wall). The results also indicated that the Stokes drag law is typically within one order of magnitude of the drag force prediction of the numerical model. Limitations of the numerical model include the assumption of a Newtonian fluid, the assumption that both the vessels and the microbubbles were rigid, and the absence of erythrocytes in the model.

Future work on this project is focused on two objectives. First, the numerical model will be extended to model therapeutic drug delivery via the target microbubbles. Using targeted drug delivery would allow not only the detection of a biofilm based infection, but would also enable the immediate delivery of either therapeutic drugs. The second future objective is additional experimental measurements to validate the microbubble attachment model, assess the effects of nearby medical device materials on the feasibility of ultrasound imaging of microbubbles, and evaluate treatment options including therapeutic drug delivery and the disruption of the physical structure of the biofilm using either ultrasound energy directly or the rupturing of microbubbles.

#### ACKNOWLEDGEMENTS

This work was supported by the McNair Scholars program (U.S. Dept. of Education grant #P217A130148) and NSF grant CBET 1249950.

#### REFERENCES

1. Harro, J. M., Peters, B. M., O'May, G. A., Archer, N., Kerns, P., Prabhakara, R., and Shirliff, M. E. (2010) Vaccine development in *Staphylococcus aureus*: taking the biofilm phenotype into consideration, *Fems Immunol Med Mic* 59, 306–323.
2. Frasca, D., Dahyot-Fizelier, C., and Mimoz, O. (2010) Prevention of Central Venous Catheter-related Infection in the Intensive Care Unit, *Intensive Care Medicine: Annual Update* 2010, 223–234.
3. Mermel, L. A., Farr, B. M., Sherertz, R. J., Raad, I. I., O'Grady, N., Harris, J. S., and Craven, D. E. (2001) Guidelines for the management of intravascular catheter-related infections, *Clin Infect Dis* 32, 1249–1272.
4. Passerini, L., Lam, K., Costerton, J. W., and King, E. G. (1992) Biofilms on Indwelling Vascular Catheters, *Crit Care Med* 20, 665–673.
5. Anastasiadis, P., Mojica, K. D. A., Allen, J. S., and Matter, M. L. (2014) Detection and quantification of bacterial biofilms combining high-frequency acoustic microscopy and targeted lipid microparticles, *J Nanobiotechnol* 12.
6. Shohet, R., Chen, S., Zhou, Y. T., Wang, Z. W., Meidell, R. S., Unger, R., and Grayburn, P. A. (2000) Targeted gene delivery to the left ventricular myocardium using ultrasound-triggered microbubble destruction, *J Am Coll Cardiol* 35, 444a–444a.
7. Wilkes, J. O. (2006) *Fluid mechanics for chemical engineers with Microfluidics and CFD*, 2nd ed., Prentice Hall Professional Technical Reference, Upper Saddle River, NJ.
8. Bigelow, T. A., Northagen, T., Hill, T. M., and Sailer, F. C. (2008) Ultrasound Histotripsy and the Destruction of *Escherichia Coli* Biofilms, *Ieee Eng Med Bio*, 4467–4470.
9. Schade, G. R., Keller, J., Ives, K., Cheng, X., Rosol, T. J., Keller, E., and Roberts, W. W. (2012) Histotripsy Focal Ablation of Implanted Prostate Tumor in an ACE-1 Canine Cancer Model, *J Urology* 188, 1957–1964.
10. Chapuis, J. C., Schmaltz, R. M., Tsosie, K. S., Belohlavek, M., and Hecht, S. M. (2009) Carbohydrate Dependent Targeting of Cancer Cells by Bleomycin-Microbubble Conjugates, *J Am Chem Soc* 131, 2438.
11. Rand, A., Gilman, G., Kane, D., and Belohlavek, M. (2008) Biotinylated Microbubbles Targeted to Amyloid., *The Open Clinical Chemistry Journal* 1, 75–78.
12. Ferrara, K., Pollard, R., and Borden, M. (2007) Ultrasound microbubble contrast agents: Fundamentals and application to gene and drug delivery, *Annual Review of Biomedical Engineering* 9, 415–447.
13. Bloch, S. H., Dayton, P. A., and Ferrara, K. W. (2004) Targeted imaging using ultrasound contrast agents, *Ieee Eng Med Biol* 23, 18–29.
14. Brady, R. A., Leid, J. G., Kofonow, J., Costerton, J. W., and Shirliff, M. E. (2007) Immunoglobulins to surface-associated Biofilm Immunogens provide a novel means of visualization of methicillin-resistant *Staphylococcus aureus* Biofilms, *Applied and Environmental Microbiology* 73, 6612–6619.
15. Brobst, T., Rombola, C., Ungerleider, S., Voncannon, S., and Ward, B. (2013) Targeted Microbubble Drug Delivery in an Experimental Treatment Model of Crohn's Disease, *The Spectra*, 27–35.

16. Schmidt, B. J., Sousa, I., van Beek, A. A., and Bohmer, M. R. (2008) Adhesion and ultrasound-induced delivery from monodisperse microbubbles in a parallel plate flow cell, *J Control Release* 131, 19-26.
17. Takalkar, A. M., Klibanov, A. L., Rychak, J. J., Lindner, J. R., and Ley, K. (2004) Binding and detachment dynamics of microbubbles targeted to P-selectin under controlled shear flow, *J Control Release* 96, 473-482.
18. Stride, E. P., and Coussios, C. C. (2010) Cavitation and contrast: the use of bubbles in ultrasound imaging and therapy, *P I Mech Eng H* 224, 171-191.
19. Tinkov, S., Bekeredjian, R., Winter, G., and Coester, C. (2009) Microbubbles as Ultrasound Triggered Drug Carriers, *Journal of Pharmaceutical Sciences* 98, 1935-1961.
20. Dayton, P. A., and Rychak, J. J. (2007) Molecular ultrasound imaging using microbubble contrast agents, *Front Biosci* 12, 5124-5142.
21. Klibanov, A. L., Rychak, J. J., Yang, W. C., Alikhani, S., Li, B., Acton, S., Lindner, J. R., Ley, K., and Kaul, S. (2006) Targeted ultrasound contrast agent for molecular imaging of inflammation in high-shear flow, *Contrast Media Mol I* 1, 259-266.
22. Unger, E. C., Porter, T., Culp, W., Labell, R., Matsunaga, T., and Zutshi, R. (2004) Therapeutic applications of lipid-coated microbubbles, *Advanced Drug Delivery Reviews* 56, 1291-1314.
23. Finnoy, A. (2013) Acoustic and Mechanical Properties of Microbubbles Stabilized by Polymeric Nanoparticles, In *Department of Physics, Norwegian University of Science and Technology, Trondheim*.
24. Gresho, P. M., Sani, R. L., and Engelman, M. S. (1998) *Incompressible flow and the finite element method : advection-diffusion and isothermal laminar flow*, Wiley, Chichester.
25. Fung, Y. C. (1984) *Biodynamics : circulation*, Springer-Verlag, New York.
26. Box, F. M. A., van der Geest, R. J., Rutten, M. C. M., and Reiber, J. H. C. (2005) The influence of flow, vessel diameter, and non-Newtonian blood viscosity on the wall shear stress in a carotid bifurcation model for unsteady flow, *Invest Radiol* 40, 277-294.
27. Sboros, V., Glynos, E., Ross, J. A., Moran, C. M., Pye, S. D., Butler, M., McDicken, W. N., Brown, S. B., and Koutsos, V. (2010) Probing microbubble targeting with atomic force microscopy, *Colloid Surface B* 80, 12-17.
28. Saffman, P. G. (1965) Lift on a Small Sphere in a Slow Shear Flow, *Journal of Fluid Mechanics* 22, 385.
29. Ward, M. D., Dembo, M., and Hammer, D. A. (1994) Kinetics of Cell Detachment — Peeling of Discrete Receptor Clusters, *Biophys J* 67, 2522-2534.

#### ABOUT THE STUDENT AUTHOR

Joshua Gosney received his A.S. degree in economics from Flathead Valley Community College in 2010. In 2012, Mr. Gosney began his academic pursuits at Montana State University, where he completed his B.S. degree in Chemical Engineering on May, 2015. Joshua Gosney has since begun his Chemical Engineering PhD. studies at the University of Arizona. At the time this paper was written, Mr. Gosney was conducting research in the computational bio-fluids laboratory under the advisement of Dr. Jeffrey Heys, and their work was focused around developing a targeted drug delivery system with use of microbubble conjugates. Mr. Gosney is a proud Native American, McNair Scholar, and an active member of the American Indian Science and Engineering Society, American Institute of Chemical Engineers student group, U.S. Green Building Council, Sustainability committee, Leadership Institute and the Undergraduate Scholars Program.

#### SUMMARY

The inability to noninvasively detect some diseases such as biofilm-based infections and cancer is a significant challenge. The combination of targeted microbubbles and ultrasound has been shown to potentially be an effective and inexpensive method of detection for diseases such as biofilm-based infections, cancer, and the formation of atherosclerotic plaque, among others. This study focuses on determining the biological flow conditions where microbubbles are likely to be an effective targeting agent in the human body versus flow conditions where microbubble attachment is unlikely due to large hydrodynamic forces on the microbubble. The goals of this project were to develop a numerical model predicting the forces on a microbubble, validate the model using published experimental measurements, assess the potential for using a simplified analytical model for predicting the hydrodynamic forces, and, finally, assess the potential for microbubble attachment under various biological flow conditions within the human body.

# Utilizing Machine Learning to Accelerate Automated Assignment of Backbone NMR Data

Joel Venzke<sup>a,b</sup>, David Mascharka<sup>a</sup>, Paxten Johnson<sup>a,b</sup>, Rachel Davis<sup>a,\*</sup>, Katie Roth<sup>a</sup>, Leah Robison<sup>a</sup>, Adina Kilpatrick<sup>b</sup> and Timothy Urness<sup>a</sup>

<sup>a</sup>Department of Mathematics and Computer Science, Drake University, Des Moines, IA

<sup>b</sup>Department of Physics and Astronomy, Drake University, Des Moines, IA

Students: joel.venze@drake.edu, david.mascharka@drake.edu, paxten.johnson@drake.edu, rachel.davis@drake.edu\*, katherine.roth@drake.edu, leah.robison@drake.edu

Mentors: adina.kilpatrick@drake.edu, timothy.urness@drake.edu

## ABSTRACT

Nuclear magnetic resonance (NMR) spectroscopy is a powerful method for determining three-dimensional structures of biomolecules, including proteins. The protein structure determination process requires measured NMR values to be assigned to specific amino acids in the primary protein sequence. Unfortunately, current manual techniques for the assignment of NMR data are time-consuming and susceptible to error. Many algorithms have been developed to automate the process, with various strengths and weaknesses. The algorithm described in this paper addresses the challenges of previous programs by utilizing machine learning to predict amino acid type, thereby increasing assignment speed. The program also generates place-holders to accommodate missing data and amino acids with unique chemical characteristics, namely proline. Through machine learning and residue-type tagging, the assignment process is greatly sped up, while maintaining high accuracy.

## KEYWORDS

Chemical Shift; Machine Learning; NMR; Artificial Intelligence; Proteins; Bioinformatics

## INTRODUCTION

Nuclear Magnetic Resonance (NMR) spectroscopy is a powerful method for obtaining atomic-resolution three-dimensional protein structures,<sup>1</sup> as well as assessing changes in protein conformations or motions due to mutations or interactions with ligands or other biomolecules. Determining a protein's structure is essential for understanding its function and alterations in function, which often lead to disease. The analysis of NMR data, in particular the sequence-specific assignment of backbone and side-chain protein resonances, is an error-prone and time-consuming step during protein structure determination by NMR spectroscopy.<sup>2</sup> This paper describes a computational algorithm that utilizes machine learning in the process of automating the assignment of backbone protein NMR resonances.

## BACKGROUND

NMR experiments generate information on several variables that can be used in the determination of protein structures.<sup>1</sup> In particular, essential information is provided by the chemical shifts of NMR-active nuclei present in proteins, including hydrogen and isotopes of carbon and nitrogen.<sup>3</sup> The chemical shift is a quantifier for the deviation in the resonant frequency of a nucleus from its value in a structure-free environment, and therefore provides information on the local conformation. Measuring the chemical shifts of all or most of the nuclei in a protein is the first step in determining its structure by NMR spectroscopy. An important set of protein chemical shifts are those corresponding to the nuclei in the backbone of the protein polypeptide chain, including the amide nitrogen (N), attached hydrogen (H), and the alpha and beta carbons ( $C_\alpha$  and  $C_\beta$ ) of each residue. Chemical shift values are measured using various three-dimensional NMR experiments,<sup>4</sup> and then matched to the individual residues in the protein in a process called sequential assignment.

Triple resonance experiments on hydrogen, nitrogen, and carbon nuclei are the method of choice for proteins and other large biomolecules, because they can greatly decrease the amount of spectral overlap in data.<sup>5</sup> Typical experiments for the assignment of backbone resonances include HNCA, HN(CO)CA, HNCACB, and CBCA(CO)NH or HN(CO)CACB.<sup>6</sup> These experiments transfer magnetization over the protein polypeptide chain, and thus connect different spin systems through covalent bonds. A spin system contains all resonances belonging to a particular residue in the protein sequence. The order of elements in experiment names indicates the order in which magnetization is

passed down the line of nuclei, resonances in parentheses being used only for transfer to the next nucleus. All these experiments produce NMR spectra with common H-N resonance correlations, and provide connectivities between neighboring residues.<sup>7</sup> For example, the HNCACB experiment identifies the chemical shifts corresponding to the  $C_\alpha$  and  $C_\beta$  nuclei of each residue in the protein chain (residue  $i$ ), as well as the immediately preceding residue (residue  $i - 1$ ).<sup>8</sup> In this experiment, resonances corresponding to residue  $i$  can usually be distinguished from the  $i - 1$  values due to their higher intensity. However, ambiguities can arise if the intensities are comparable or if chemical shift ranges overlap. These ambiguities can be resolved by using additional experiments. For example, the CBCA(CO)NH experiment yields the chemical shifts of the preceding residue only, unambiguously identifying  $i$  and  $i - 1$  values.<sup>9</sup> Using all inter-residue connectivities, a chain of correlations through the protein backbone chemical shifts can be established. The pattern of sequentially-linked chemical shift values reflects the linear arrangement of individual residues in the protein sequence. This pattern is then matched to the protein sequence through certain residues with characteristic  $C_\alpha$  and  $C_\beta$  chemical shift values that uniquely identify them. Thus, each measured chemical shift is assigned to a protein residue and can then be used to infer structural information about the biomolecule.

### SEQUENTIAL ASSIGNMENT STRATEGIES

The sequential assignment of backbone chemical shifts can be done manually or in an automated fashion. Both approaches follow similar strategies. The process starts by identifying the chemical shifts of  $i$  and  $i - 1$  residues from a set of three-dimensional NMR experiments. Many computer programs, such as NMRPipe<sup>10</sup> and SPARKY,<sup>11</sup> can be used to process, analyze, and visualize NMR data. After grouping chemical shifts into spin systems, they are linked into increasingly larger segments by matching  $i$  and  $i - 1$  values. This process can be seen in **Figure 1**. In parallel, the spin systems are classified into possible residue types, using a set of established chemical shift values for each of the 20 common amino acids found in proteins. For example, alanines have  $C_\alpha$  and  $C_\beta$  chemical shifts ranging from approximately 50 to 56 ppm (parts-per-million), and 17 to 25 ppm, respectively; glycines have unique  $C_\alpha$  values in the 45 ppm region, and threonines have distinctive  $C_\beta$  values in the 68-73 ppm range.<sup>3,12</sup> Using the residue type information, the linked segments from the resonance sequential walk are iteratively mapped onto the primary protein sequence.

Chemical Shift (ppm)	Residue $i-1$	Residue $i$	Residue $i+1$
$C_\alpha$ (self)	66.770	55.393	59.224
$C_\beta$ (self)	38.056	17.975	29.006
$C_\alpha$ (preceding)	58.701	66.743	55.335
$C_\beta$ (preceding)	29.070	38.067	17.927

Figure 1. Sequential residues are linked by matching  $i$  and  $i - 1$  chemical shifts

When performed manually, the assignment process is time-consuming and prone to error. If chemical shift values overlap, multiple matches between  $i$  and  $i - 1$  values are possible. The classification of spin systems into amino acid types also has a high potential for error, as the spin systems can look identical or very similar, even for very different amino acids. In recent years, advances in computer technology, accompanied by the increased use of NMR spectroscopy in drug design and structural genomics initiatives, have created a push for the automation of various steps in the NMR structure determination process.<sup>13</sup> These automated methods decrease the time needed to complete the assignment, and attempt to minimize the risk of human error and subjectivity. A wide variety of algorithms and software packages for the assignment of backbone chemical shifts exist,<sup>14,15</sup> including GARANT,<sup>16</sup> AutoAssign<sup>13,17</sup> and MARS.<sup>18</sup>

### RELATED WORK

GARANT is an example which has three key elements in an algorithm.<sup>16</sup> GARANT starts by matching observed peaks to expected peaks in the backbone sequence, scoring these values, and then running through an optimization routine. This optimization is similar to simulated annealing, which makes repeated selections until a solution is reached. If the current selection decreases error, it becomes the new structure. If it is worse, a new selection is made based on probability.<sup>13</sup>

SPARKY uses a method called AUTOASSIGN, a heuristic, best-first mapping algorithm.<sup>11</sup> This program utilizes

five basic steps. It first filters peaks and aligns resonances from different spectra.<sup>17</sup> Then, it groups these resonances based on their spin systems and identifies the amino acid types. Next, the already assigned segments are found and linked together into short chains. Finally, a solution is obtained.

MARS looks to optimize the quality of assignments overall.<sup>18</sup> This program breaks the assignment into segments, assigning up to five pieces into a chain and using them as units in assignment. Then, by combining secondary structure analysis with assignment, the most accurate model is selected and expanded upon. Lastly, MARS tests the chemical shifts for noise and reliability.

Programs such as GARANT, AUTOASSIGN, and MARS, have limitations. The best-first strategies employed by some of these programs may abandon a promising set too early and the optimum solution will not be selected. Many programs also experience difficulty with handling local minimums; not being able to identify these outliers in the assignment process can throw off the optimization process. Further issues also arise when programs try to assign larger protein chains, often needing days to finish assignment and still having very high error calculations. Even though these issues exist, these programs have paved the way for the automation of chemical shift assignments and made significant advances in the field of protein NMR spectroscopy.

Our algorithm utilizes elements from these existing programs, such as cost analysis and sorting amino acids into groups, but employs novel concepts from machine learning to accelerate the assignment process.

## MACHINE LEARNING

Machine learning provides algorithms that learn from attributes in the input data to increase performance. Supervised learning, a field of machine learning, builds a model based on numerous data elements and their respective labels. The result is a mathematical model that predicts a label given a set of input attributes. Machine learning algorithms provide excellent solutions for building models that generalize well given large amounts of data with potentially many attributes by discovering patterns and trends in the data; a task that is often difficult or impossible by other means.

Machine learning offers a natural solution to the problem of determining amino acid type from NMR chemical shift values. The overlap in the normal range of  $C_{\alpha}$  and  $C_{\beta}$  values among many amino acids makes it difficult to infer the type of residue based solely on chemical shift information. Machine learning algorithms offer a unique approach to this problem and achieve excellent accuracy.

There are several supervised machine learning algorithms that can be applied to improve automated assignment strategies. The J4.8 algorithm<sup>19</sup> builds a decision tree model. This means that the data is split based on a comparison to an attribute of the data, with a branch for each possible outcome of the test. At the end of the tree, the leaf, is the predicted label. In our case this is the amino acid type. To classify a new value, a datapoint begins at the root of the tree and moves through until a leaf is encountered. The encountered leaf is the predicted value for that datapoint. To construct the tree, the attribute test used at each branch is the one that partitions the set in the most useful manner.

The Logistic Model Tree, or LMT,<sup>20</sup> is another tree-based algorithm. In contrast to the J4.8 algorithm, LMT constructs a tree with logistic regression functions at each branch rather than an attribute test. Logistic regression attempts to model class probabilities with linear functions. The weights used for each function can be learned to split each class in a way somewhat analogous to the split in J4.8 described above.

The Decision Table algorithm<sup>21</sup> is comprised of a set of features and a set of labeled data. To classify a new datapoint, the set of labeled data is searched for a match with the new point, considering only the features in the feature set. If no matches are found, the majority class of the labeled data is used. Otherwise, the majority class of the matches is used.

## PROGRAM DEVELOPMENT

Our goal is to create an automated program for the assignment of protein backbone chemical shifts that can deliver quality results in a small amount of time without the use of a supercomputer. Our program implements group sorting, machine learning, filtered amino acid selection, and careful cost calculations. The algorithm completes resonance assignment in six steps: (1) the NMR chemical shifts and the protein sequence are used to fill data structures; (2) the protein sequence is processed and empty data structures are initialized for missing data; (3) model created utilizing machine learning is employed to assign possible amino acid types to each spin system; (4) filtering is applied to locate chemical shift values that could potentially be assigned to residue 1 in the protein sequence; (5) the search process continues and identifies the closest-matching sequence until all chemical shift data is assigned; (6) the best solution is recorded and the process is terminated.

Before the algorithm begins the assignment process, machine learning is used to build a model for predicting amino acid type. After the model is trained, the pre-processing component of the algorithm (steps 1 to 3) begins. Pre-processing is where our research has made significant advances; by predicting amino acid types with machine learning algorithms, the assignment time is decreased significantly. Machine learning allows the data to be filtered, significantly reducing the search space and consequently the running time of the algorithm. The algorithm is then able to intelligently search the remaining possibilities for the best assignment (**steps 4 to 6**).

## METHODS

### *Machine Learning Data Collection*

The training dataset for the machine learning algorithm was obtained from the Biological Magnetic Resonance Bank (BMRB), a database of NMR chemical shifts hosted by the University of Wisconsin-Madison.<sup>22</sup> We initially identified 9,736 datasets containing chemical shifts for the  $C_\alpha$  and  $C_\beta$  resonances of 689,977 residues. In order to improve both accuracy and generalization, and to prevent the algorithm from fitting extraneous data, it was necessary to remove outliers from the published datasets. By inspecting statistics available on the BMRB site, we excluded chemical shift values outside three standard deviations of the mean for each amino acid type. This gave us 681,363 pairs of  $C_\alpha$  and  $C_\beta$  values to use for training.

### *Pre-processing*

**Step 1** of our algorithm consists of reading the chemical shift values and the protein amino acid sequence from an input file. We use the  $C_\alpha$  and  $C_\beta$  values for each pair of  $i$  and  $i - 1$  residues to create an object we will refer to as a *tile*. A tile holds all the available chemical shift information corresponding to a single residue in the protein sequence to be assigned.

**Step 2** of the algorithm converts the primary protein sequence into  $C_\alpha$  and  $C_\beta$  chemical shift values, using statistics available in BMRB. These statistics provide average chemical shift values for each of the twenty common amino acids found in proteins. For example, we assign alanine a  $C_\alpha$  chemical shift of 53.19 ppm and a  $C_\beta$  chemical shift of 18.96 ppm. Next, the algorithm searches the protein sequence for prolines. As prolines lack H-N spin systems, HNCACB and CBCA(CO)NH experiments do not provide  $C_\alpha$  and  $C_\beta$  chemical shifts for this residue. Special tiles, designed to specifically identify the proline residue, are created to handle this case. Identifiers in the proline tiles ensure that these tiles are placed only when the corresponding residue in the protein sequence is a proline. The identifier limits the number of possibilities where the tile can be assigned. The length of the protein sequence is then compared to the total number of tiles created thus far. If fewer tiles exist than the overall number of residues, blank tiles are created to fill the difference. Blank tiles can fit in any location in the assignment. However, large amounts of missing data will deteriorate the algorithm's performance as every blank tile would need to be checked for the best fit in every position in the assignment.

**Step 3** assigns possible amino acid types to each tile. The  $C_\alpha$  and  $C_\beta$  values for residue  $i$  in each tile are processed by our machine learning model, producing a list of probabilities that a tile represents a certain amino acid. The probabilities correspond to confidence levels used for filtering during the assignment process.

Preprocessing the dataset takes a minimal amount of time (less than a second on a standard laptop) and drastically reduces the time required to assign the chemical shifts without affecting accuracy. The search for the optimal assignment then begins.

### *The Search*

The algorithm initiates an intelligent search through filtered combinations of all possible chemical shifts. The search begins with **step 4** by placing the first tile, which is selected based on the filtering process. Only tiles that could correspond to the first amino acid based on a confidence level threshold (0.4% match or better) are placed at residue one. The threshold was chosen by determining the lowest probability for a correct amino acid classification.

At this point, a "cost" of assignment is generated. The cost of placing a tile consists of two parts: (1) the difference between the tile's residue  $i - 1$  values and the previous tile's residue  $i$  values, and (2) the difference between the residue  $i$  values and the values predicted from the protein sequence. In the case of blank and proline tiles, a fixed cost is added instead of the above calculation. This value is set to ensure a blank tile is neither the best nor worst option, allowing the blank and non-blank tiles to be considered simultaneously by the algorithm. When the first tile is placed, the cost is based solely on a comparison to the protein sequence, and the search moves on to **step 5**.

In **step 5**, the algorithm selects the assignment with the lowest cost to continue the search process. The solution is reached when all tiles have been placed in an assignment and the solution has the lowest cost. If the assignment is not a solution, the amino acid type of the next residue in the protein sequence is retrieved. Any unplaced tile that corresponds to that amino acid type with a confidence level above the threshold is placed at the next location in the sequence. In the special case that the next amino acid type is proline, only the special proline tiles are considered for placement. The cost is then adjusted to include the newly placed tile. **Step 5** is repeated until a solution has been reached.

In the final step the search records the solution. The solution assignment, along with the performance (the number of possible assignments searched) is output. Then the algorithm terminates.

## RESULTS

The chemical shift dataset used in this study consisted of  $C_\alpha$  and  $C_\beta$  values for the 62-residue long C-terminal domain of the Tfg1 subunit of the yeast transcription factor TFIIF. The chemical shifts were previously obtained by Kilpatrick et al. from HNCACB and CBCA(CO)NH experiments, and manually assigned to 99% completeness.<sup>23</sup> The chemical shift dataset was divided into sub-sections, randomized, and used for algorithmic analysis.

The results of assigning this dataset with different filtering methods are shown in **Figure 2**. Each of the tests described in **Figure 2** follows a smooth trend, as opposed to a highly irregular trend which would indicate an impediment in the processing and assignment of data. A comparison of the methods indicates that our filtering process results in a significant decrease in number of generated nodes compared to an unfiltered generic search algorithm similar to a predecessor to this algorithm.<sup>24</sup> Since the most time-consuming part of the search is node generation, there is a direct correlation between assignment time and the number of nodes generated. With a 2.3 GHz Intel Core i7 processor and 8 GB of RAM, generating 7036 nodes requires approximately 1 second. The graph in **Figure 2** indicates that the LMT machine learning algorithm has the best performance, outperforming the unfiltered method by almost two orders of magnitude, without loss of assignment accuracy. LMT was able to assign all 62 residues within forty-five minutes, whereas the other filters were unable to complete the full assignment within a 12 hour time limit. The LMT model not only accelerates assignment, but also allows for larger datasets to be assigned in the same amount of time.

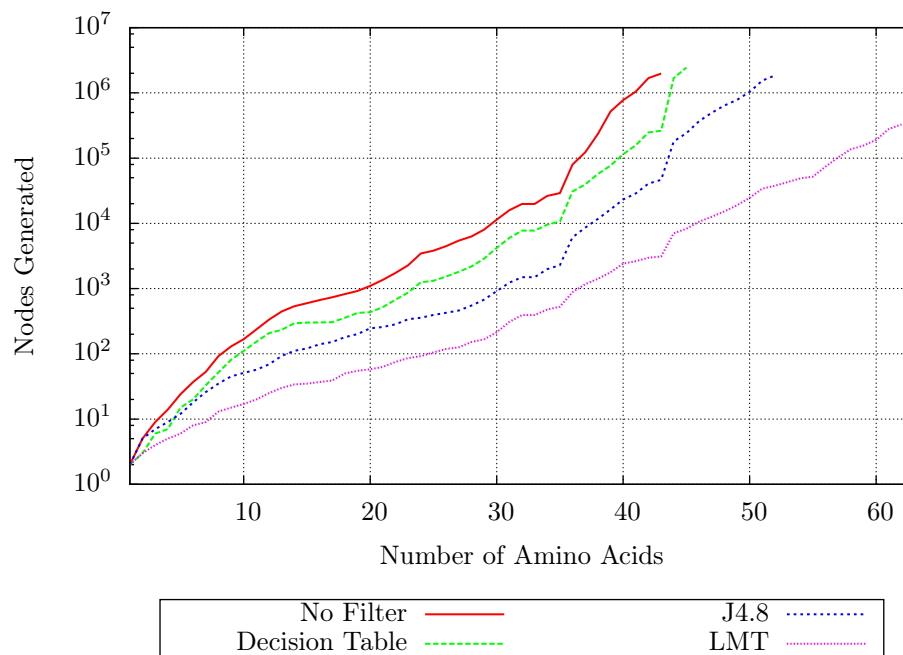


**Figure 2.** Impact of filtering methods on assignment time. Number of nodes (y-axis) is plotted as a function of number of residues (protein sequence length) used in the assignment (x-axis). The search without machine learning filtering is depicted in red. The other three groups (DecisionTable, J4.8 and LMT) are the machine learning algorithms that were used for filtering, e.g. DecisionTable used a Decision Table for the filtering process.

The impact of proline identification on our algorithm's performance is shown in **Figure 3**. In the sequence of the studied protein, residue 33 is a proline, for which chemical shifts are missing. The same unfiltered and LMT data from **Figure 2** is plotted for comparison. The large jump in assignment time between residues 32 and 33 shows the impact of missing data on performance without filtering and using the LMT model. If the algorithm identifies and handles prolines as a special case, only one more node is generated for the 33-residue long sequence. However, if the proline is not dealt with separately, the algorithm's performance is significantly impacted. Without proline checking, the proline tile is placed in every position in the assignment. The result is a major increase in the branching factor that leads to the jump observed in **Figure 3**. With proline checking, prolines are no longer problematic to the assignment process. This indicates that our algorithm can accurately obtain assignments with reasonably fast assignment times even when chemical shift data is missing.

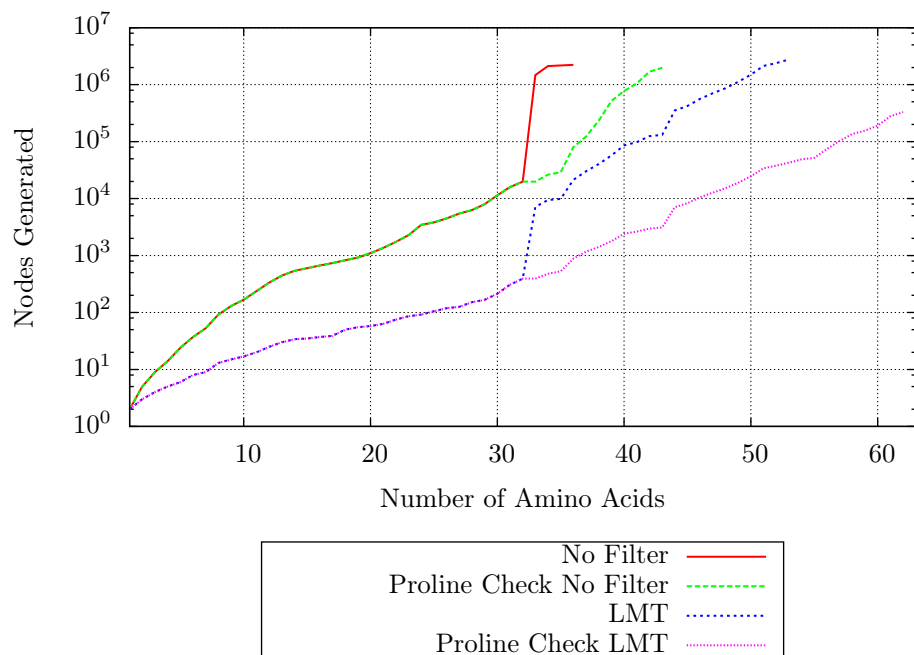


**Figure 3.** Impact of proline identification on assignment time. Number of nodes (y-axis) is plotted as a function of number of residues used in the assignment (x-axis). Red shows the search without proline checking and without machine learning filtering. Similarly, the search with proline checking without machine learning filtering is depicted in green. The search without proline checking using LMT machine learning filtering is depicted in blue. Utilizing proline checking and LMT machine learning filtering is depicted in pink.

In order to evaluate our algorithm's performance, and effectiveness, we compare the number of nodes generated in our search to the total possible number of nodes. To calculate the total possible number of nodes, we first consider  $n$  to be the number of amino acids. The search space will start with a single node, the root node, which has no tiles placed. Call this level 0. The next level of the search space, level 1, will have  $n$  nodes, one for each of the amino acids that could go in the first spot. We now have  $n + 1$  total nodes in our search space. Off of each node in level 1, there will be  $n - 1$  nodes. So level 2 will be  $n(n - 1)$  nodes in size. We can rewrite this in the form

$$n(n - 1) = \frac{n!}{(n - 2)!} \quad \text{Equation 1.}$$

We can extend this to the  $i$ th level by replacing 2 in the denominator with  $i$  since there will be  $(n - i)$  tiles left to place at the  $i$ th level. By doing so, the number of nodes at a given level is

$$n(n - 1) \cdots (n - i + 1) = \frac{n!}{(n - i)!} \quad \text{Equation 2.}$$

To get the total search space, we sum the levels from  $i = 0$ , the root level, until  $i = n$ , the level which all amino acids are placed. This yields

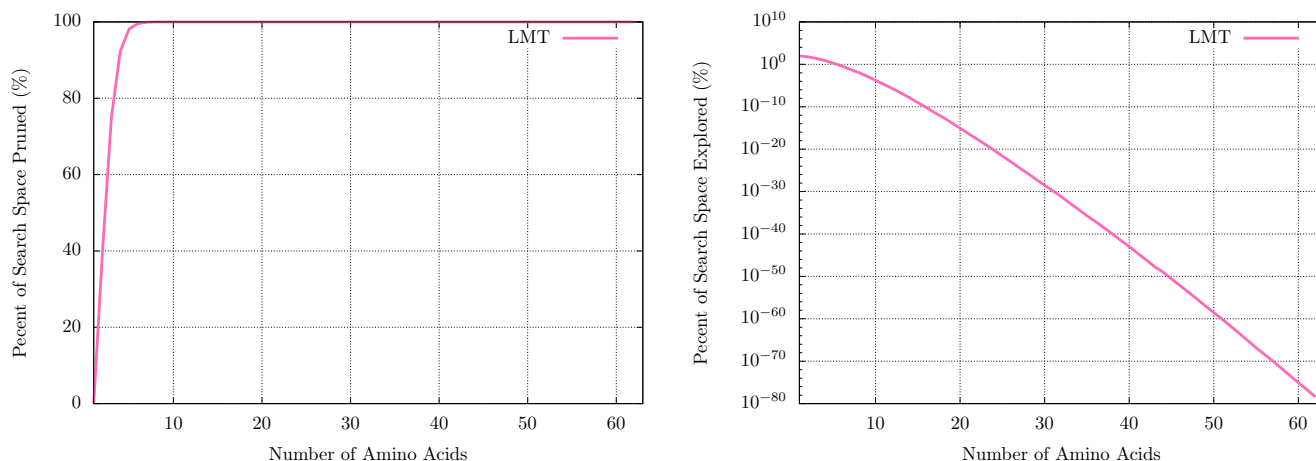


**Figure 4.** The plot on the right shows the percent of the search space not explored by the LMT model. On the left is a plot showing the percent of the Search Space that was explored by the LMT model. DecisionTable, J48 and No Filter all behave in a similar matter and are not shown for simplicity.

$$Search\ Space = \sum_{i=0}^n \frac{n!}{(n-i)!} \tag{Equation 3}$$

We can now evaluate the effectiveness of our algorithm by comparing the number of nodes generated for each of our machine learning filters to the total possible number of nodes. In **Table 1**, we have shown the results for 43 amino acids (the largest sequence that the “No Filter” for proline detection completed). The search space given by **Equation 3** for  $n = 43$  is  $1.64 \cdot 10^{53}$  nodes. The table shows that no filter explored a little over  $10^{-45}\%$  of the search space. DecisionTable, J48, and LMT each preformed approximately an order magnitude better than the one before it, with LMT exploring  $1.89 \cdot 10^{-48}\%$  of the search space.

Filtering Model	Nodes Generated	Percent of Search Space
No Filter	1,977,233	$1.20 \cdot 10^{-45}\%$
DecisionTable	262,961	$1.60 \cdot 10^{-46}\%$
J48	46,372	$2.82 \cdot 10^{-47}\%$
LMT	3,105	$1.89 \cdot 10^{-48}\%$

**Table 1.** A comparison of the filtering algorithms with respect to the search space. The results shown are for 43 amino acids, the largest set completed by the no filter algorithm.

**Figure 4** shows the relationship of the number of amino acids assigned and the amount of the search space explored by the LMT model. DecisionTable, J48, and No Filter all show the same general trend. The trend shows that the more amino acids assigned, the more of the search space is removed due to filtering. Due to the factorial growth of the search space, even  $10^{-79}\%$  of the search space is over 300,000 nodes in size when taken for  $n = 62$ . As we can see, even an extremely small percentage of the search space can have a major impact on the assignment process. The addition of filtering to our algorithm removes large portions of the search space and drastically reduces assignment times.

Our algorithm with LMT filtering and proline checking can complete the 62-residue assignment in approximately 40 minutes on a 2.3 GHz Intel Core i7 processor with 8Gb of RAM. The LMT model with proline checking can complete the assignment of a 43-residue long sub-sequence in less than 1 second, compared to 27, 29 and 30 seconds without filtering, using a Decision Table for filtering and using the J4.8 model for filtering, respectively. In all cases, the solution from the automated algorithm is identical to the manual assignment, indicating that our algorithm is both fast and accurate.

## CONCLUSIONS AND FUTURE DIRECTIONS

Our algorithm has made significant advances in the field of automated assignment of protein backbone chemical shifts. We implemented machine learning to filter NMR data in order to reduce the branching factor in a search-based algorithm. This increased our assignment rate by approximately three orders of magnitude, as seen in **Figure 3**, while still maintaining the accuracy of the solution.

The use of proline checking and the utilization of machine learning to filter data has shown to be extremely effective in accelerating the assignment. Our algorithm has successfully completed assignments of up to 62 amino acids in 40 minutes without the use of a supercomputer. The same sequence took several days to manually assign. If allotted more time, more residues from a larger dataset could be assigned.

One of our main focuses for the future is handling missing data in a more efficient manner. By examining characteristics of the amino acids in the sequence, we hope to predict where missing data will end up in the final assignment. This would reduce the number of assignments attempted by greatly reducing the number of nodes in the search. Furthermore, we will work to improve the overall performance of our algorithm by optimizing cost calculations and investigate assignment via parallel processing.

We are currently measuring the backbone chemical shifts of a protein previously uncharacterized by NMR spectroscopy. This new dataset will include additional chemical shifts that can be used in the assignment process, such as the backbone carbonyl and H-alpha values. This data will be used to further validate and improve our algorithm. Since the cost calculation is crucial to the effectiveness of our algorithm, additional chemical shifts may prove invaluable to the success of the algorithm for longer protein sequences or incomplete datasets. We are also investigating methods of predicting the final cost of an assignment in order to remove unrealistic assignments early on. Having this information available will help optimize our cost calculation, resulting in a further decrease in assignment times.

## ACKNOWLEDGEMENTS

The authors of this paper thank Drake University for being a conducive space to research, and John Emmons for initiating this research.

## REFERENCES

1. Wüthrich, K. (1990), Protein structure determination in solution by NMR spectroscopy., *The Journal of Biological Chemistry* 265, 22059–22062.
2. Linge, J. P., Habeck, M., Rieping, W., Nilges, M. (2003), ARIA: Automated NOE assignment and NMR structure calculation, *Bioinformatics*.
3. Wishart, D., Nip, A. (1998), Protein chemical shift analysis: a practical guide., *Biochemistry and Cell Biology* 76, 153–163.
4. Nagayama, K. (1988), Three-dimensional NMR spectroscopy, US Patent 4,789,832.
5. Kay, L. E., Ikura, M., Tschudin, R., Bax, A. (1990), Three-dimensional triple-resonance NMR spectroscopy of isotopically enriched proteins, *Journal of Magnetic Resonance (1969)* 89, 496–514.
6. Cavanagh, J., Fairbrother, W. J., III, A. G. P., Rance, M., Skelton, N. J. (2007), *Protein NMR Spectroscopy*, second edition ed., Academic Press: Burlington.
7. Bax, A. (2011), Triple resonance three-dimensional protein NMR: Before it became a black box, *Journal of Magnetic Resonance* 213, 442–445.
8. Wittekind, M., Mueller, L. (1993), HNCACB, a high-sensitivity 3D NMR experiment to correlate amide-proton and nitrogen resonances with the alpha-and beta-carbon resonances in proteins, *Journal of Magnetic Resonance, Series B* 101, 201–205.
9. Rios, C. B., Feng, W., Tashiro, M., Shang, Z., Montelione, G. T. (1996), Phase labeling of C- H and C- C spin-system topologies: Application in constant-time PFG-CBCA (CO) NH experiments for discriminating amino acid spin-system types, *Journal of Biomolecular NMR* 8, 345–350.
10. Delaglio, F., Grzesiek, S., Vuister, G., Zhu, G., Pfeifer, J., Bax, A. (1995), NMRPipe: A multidimensional spectral processing system based on UNIX pipes, *Journal of Biomolecular NMR* 6, 277–293.
11. Goddard, T., Kneller, D. SPARKY 3, University of California, San Francisco, <https://www.cgl.ucsf.edu/home/sparky/> (Accessed February 2015).

12. Wang, Y., Jardetzky, O. (2002), Probability-based protein secondary structure identification using combined NMR chemical-shift data., *Protein science : a publication of the Protein Society* 11, 852–861.
13. Moseley, H. N. B., Monleon, D., Montelione, G. T. (2001), Automatic determination of protein backbone resonance assignments from triple resonance nuclear magnetic resonance data, Elsevier, 339, pp 91–108.
14. Güntert, P. (2009), Automated structure determination from NMR spectra, *European Biophysics Journal* 38, 129–143.
15. Emmons, J., Johnson, S., Urness, T. (2013), Automated Assignment Of Backbone NMR Data using Artificial Intelligence, [http://micsymposium.org/mics\\_2013\\_Proceedings/submissions/mics20130\\_submission\\_26.pdf](http://micsymposium.org/mics_2013_Proceedings/submissions/mics20130_submission_26.pdf) (Accessed February 2015).
16. Bartels, C., Güntert, P., Billeter, M., Wüthrich, K. (1997), GARANT - A General Algorithm for Resonance Assignment of Multidimensional Nuclear Magnetic Resonance Spectra, *Journal of Computational Chemistry* 18, 139–149.
17. Zimmerman, D. E., Kulikowski, C. A., Huang, Y., Feng, W., Tashiro, M., Shimotakahara, S., ya Chien, C., Powers, R., Montelione, G. T. (1997), Automated Analysis of Protein NMR Assignments Using Methods from Artificial Intelligence, 269, *"J Mol Bio"*, pp 592–610.
18. Jung, Y., Zweckstetter, M. (2004), Mars-robust automatic backbone assignment of proteins, *Journal of Biomolecular NMR* 30, 11–23.
19. Quinlan, R. (1993), *C4.5: Programs for Machine Learning*, Morgan Kaufmann Publishers: San Mateo, CA.
20. Landwehr, N., Hall, M., Frank, E. (2005), Logistic Model Trees, *Machine Learning* 95, 161–205.
21. Kohavi, R. (1995), The Power of Decision Tables, 8th European Conference on Machine Learning, pp 174–189.
22. Ulrich, E. L. et al. (2008), BioMagResBank., *Nucleic Acids Research* 36, 402–408.
23. Kilpatrick, A. M., Koharudin, L. M., Calero, G. A., Gronenborn, A. M. (2012), Structural and binding studies of the C-terminal domains of yeast TFIIF subunits Tfg1 and Tfg2, *Proteins: Structure, Function, and Bioinformatics* 80, 519–529.
24. Emmons, J., Venzke, J., Johnson, P., Davis, R., Roth, K., Mascharka, D., Robison, L., Urness, T. (2014), Accelerating Biomolecular Nuclear Magnetic Resonance Assignment with A\*, [http://www.micsymposium.org/mics2014/ProceedingsMICS\\_2014/mics2014\\_submission\\_35.pdf](http://www.micsymposium.org/mics2014/ProceedingsMICS_2014/mics2014_submission_35.pdf) (Accessed February 2015).

**ABOUT THE STUDENT AUTHORS**

Joel Venzke is a senior pursuing a B.S. in Physics, Computer Science, and Mathematics. Outside of conducting research, Joel is president of the Drake University chapter of the Society of Physics Students and vice president of the math club. He also works as an award winning photojournalist for Drake University Communications and The Times-Delphic. Joel plans to pursue a Ph.D. in computational science.

David Mascharka is a junior seeking a B.S. in Computer Science and Mathematics and B.A. in Philosophy. David also pursues his love for mathematics as the president of the math club at Drake University, where is he able to hone his leadership skills. His research interests include machine learning and mobile computation.

Paxten Johnson is on track to graduate in the Spring of 2016 with a B.S. in Physics, Computer Science, and Mathematics. Aside from conducting this research for the past two years, she has been involved with Air Force ROTC, Delta Gamma Fraternity, and the Drake Honors Program. She hopes to use the knowledge and experience gained from this research to help her advance into the military intelligence branch of the Air Force.

Rachel Davis is currently on the path to obtaining a B.S. in both Computer Science and Mathematics, with a minor in Data Analytics. This is the second year conducting this sequencing research. Her research includes not only this primary structuring of proteins, but also a collaborative tertiary structuring algorithm. Rachel is also the president of the Women in Mathematics and Computer Science and an active member of the Math Club.

Katie Roth is pursuing a B.A. in Mathematics and Computer Science. She has been working on this research for two years, and enjoys it immensely. Katie is the vice president of the Women in Mathematics and Computer Science and an active member of Math Club.

Leah Robison is on her way to graduate with a B.S. in Environmental Science and a minor in Computer Science. Apart from studying abroad in Denmark for a semester, she has been involved with this research group for the past two years. She hopes to apply the knowledge gained from this research to future studies in the field of Environmental Science.

**PRESS SUMMARY**

Manually assigning nuclear magnetic resonance data to a protein sequence is time consuming and error prone. Although current algorithms have made advances in this area, a student research group at Drake University is improving the process by utilizing machine learning to identify amino acids before assignment. Using both old and new methods has resulted in an algorithm that is fast and accurate.

# Approximate Formulae for Willmore Surfaces via Support Functions and Matlab

Phillip M. Galbo<sup>a</sup>, Michael C. Barg<sup>\*b</sup>

<sup>a</sup>Biology Department, Niagara University, NY

<sup>b</sup>Mathematics Department, Niagara University, NY

Student: phillipgalbo@gmail.com

Mentor: mbarg@niagara.edu\*

## ABSTRACT

Bio-membrane shapes are calculated numerically by minimizing a bending energy with area and volume constraints. We use a modified Helfrich's bending energy that includes buoyancy. Spheres, prolate and oblate discocytes, tori, *Y*-shapes, and dumbbells are some of the variety of bio-membranes that have been observed without buoyancy. Since the system of differential equations that minimizers must satisfy is extremely complex, many shapes are only known to exist through their numerical solutions. Indeed, exact analytical solutions for many shapes remain elusive. Here, we consider *Y*-shapes and dumbbells and give closed-form approximate formulae for these shapes using a support function method.

**KEYWORDS** Bio-membranes; Support Functions; Willmore Surfaces; Generating Curves; Polynomial Approximation; Numerical Solutions; Matlab; Helfrich's Bending Energy

## INTRODUCTION

Bio-membrane shapes are often calculated numerically by minimizing a bending energy with area and volume constraints. In this work, we use the term bio-membrane to refer to lipid bilayers, vesicles, red blood cells, and other similar structures. Lipids can be described as hydrophobic molecules composed mostly of hydrogen and carbon molecules. A defining feature of lipids is that they are non-polar, and, therefore, insoluble in water. Lipids are an important bio-structure because they account for nearly 40% of the organic matter in the average human body and are the main components of lipid bilayers.<sup>1</sup> Such bilayer structures have been used as models for more complex structures like red blood cells and cell membranes. Lipid bilayers form because lipids are amphipathic molecules; meaning, they have hydrophilic heads and hydrophobic tails. This allows lipid heads to congregate in a manner that exposes them to surrounding aqueous solution while the lipid tails associate between the lipid heads, thus minimizing exposure to outer and inner cellular solution. A lipid bilayer can form various shapes and sizes depending on many factors, including the amount of lipids present in solution. While much recent work on these structures involves so-called multi-phase membranes that can arise when more than one type of lipid is present, here we concern ourselves with a single lipid type.<sup>2-4</sup>

From a mathematical perspective, a vesicle shape can be realized as a two-dimensional surface embedded in a three-dimensional space. Assuming axisymmetry, the bio-membrane is treated as a surface of revolution. The actual shape of the generating curve for the surface of revolution can be found as a solution to an optimization problem. Using Helfrich's bending energy,<sup>5</sup> other authors have found such numerical solutions via a Lagrange multiplier method. The idea is to minimize a total energy functional

$$E_{Total} = E_{Bending} + Area\ Constraint + Volume\ Constraint \quad \text{Equation 1.}$$

consisting of Helfrich's bending energy,  $E_{Bending}$ , and two additional terms that are included with Lagrange multipliers to enforce surface area and volume constraints. The actual formula for  $E_{Total}$  appears in many references.<sup>6</sup> We follow the same approach here, but include a term in the volume constraint to account for buoyant effects. In particular, instead of

introducing a Lagrange multiplier  $p_0$  and including

$$\text{Volume Constraint} = \int_D p_0 dV$$

we use

$$\text{Volume Constraint} = \int_D (p_0 + bz) dV$$

where  $b$  is buoyancy,  $z$  is height above a fixed reference height  $z = 0$ ,  $D$  is the interior region of the vesicle, and  $dV$  is volume measure. When  $b = 0$ , minimizers of  $E_{Total}$  are called Willmore surfaces. We also refer to minimizers with  $b \neq 0$  as Willmore surfaces. As our goal is to give formulae for Willmore surfaces, we consider only the simplest bio-membranes, that is, homogeneous vesicles and single phase lipid bilayers. Prolate and oblate discocytes, stomatocytes, dumbbells, and Y-shapes are some of the energy minimizing shapes that have been observed. Details about the minimization process and the types of solutions are readily found in the literature.<sup>6-11</sup> Some analytical solutions are known. Spherical solutions can exist in the zero buoyancy case. Also, closed-form analytical solutions are known for tori and biconcave discoids (discocytes), in addition to other constant mean curvature surfaces.<sup>10-11</sup> Additionally, other authors have given formulae that approximate discocyte shapes of red blood cells.<sup>8</sup> Our contribution in this work is to give closed-form approximate solutions for Y-shape and dumbbell solutions. We accomplish this task using a support function method.

If  $\mathbf{x}$  is a function representing a smooth surface and  $\mathbf{n}$  is a corresponding normal vector field on the surface, then a support function can be defined as  $w = \mathbf{x} \cdot \mathbf{n}$ .<sup>12</sup> In this way, at a given point in the surface, the support function measures the signed distance from the origin to the tangent plane. Support functions were first introduced by Minkowski in 1901, and they subsequently received attention in the study of minimal surfaces. Their use then diminished until recently.<sup>13</sup> In recent work, examples of minimal surfaces are given by means of spherical parameterizations created from support functions.<sup>14</sup> To this end, solutions of a particular partial differential equation involving  $w$  are analyzed. In another recent work, a Sturm-Liouville problem in terms of  $w$  is analyzed to help show the existence of certain minimal surfaces in the context of so-called period problems.<sup>13</sup> Here, we adopt the “spherical parameterization” method common to both of these works for a curve  $\mathbf{x}$  which we interpret by means of a “circular parameterization.” The relevant details for a Y-shape vesicle are presented. We begin by giving some generating curve preliminaries, in part to establish notational conventions. After demonstrating the validity of our circular parameterization, we give the closed-form approximate formulae for Y-shape vesicles and dumbbells.

### PRELIMINARIES

Assuming axisymmetry for our solutions, we seek a generating curve in the  $rz$ -plane. All the quantities described in

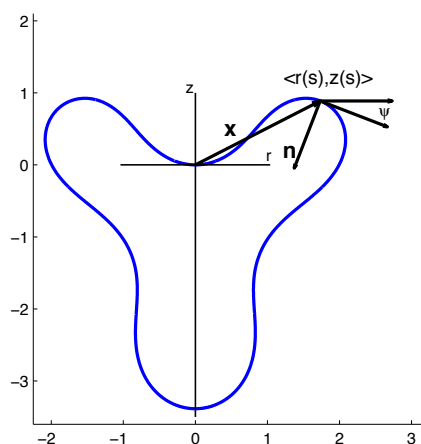


Figure 1. Generating curve for Y-shape defining  $r$ ,  $z$ ,  $\psi$ , and  $\mathbf{n}$

Figure 1 are functions of  $s$ , arc length along the generating curve.  $r = r(s)$  represents the radius of a section of the bio-membrane, and  $z = z(s)$  is the height at which that specific radius is present on the bio-membrane. Performing the minimization of  $E_{Total}$  in Matlab, we determine  $r$ ,  $z$ , and  $\psi = \psi(s)$ , where  $\psi$  is the angle between the horizontal

and tangent lines. The minimization is achieved by using a shooting method to compute a numerical solution to the Euler-Lagrange equations associated with Equation 1. subject to appropriate initial conditions and boundary conditions. In particular,  $r(0) = z(0) = 0$  and  $\psi(0) = 0$ . Also,  $r(L) = 0$  and  $\psi(L) = -\pi$ , where  $L$  is the a priori unknown length of the generating curve. It is computed as a solution in the minimization process. The details of the derivation of the appropriate system of ordinary differential equations are described elsewhere.<sup>6</sup> Plotting  $r$  and  $z$ , we obtain the shape of the bio-membrane generating curve,  $\mathbf{x} = \langle r, z \rangle$ . As pictured in Figure 1,  $\mathbf{x}(s)$  is the position vector for the point on the generating curve  $s$  units along the curve. The normal vector  $\mathbf{n} = \mathbf{n}(s)$  is computed numerically as  $\mathbf{n} = \langle \sin(\psi), -\cos(\psi) \rangle$ .

SUPPORT FUNCTIONS AND APPROXIMATE FORMULAE

The support function is defined as the dot product of  $\mathbf{x}$  and  $\mathbf{n}$

$$w = \mathbf{x} \cdot \mathbf{n} \tag{Equation 2}$$

In what follows, for a given  $w$  and  $\mathbf{n}$ , we demonstrate  $\mathbf{x}$  as a function of  $w$  and  $\mathbf{n}$ . The relationship is

$$\mathbf{x} = w\mathbf{n} + \frac{1}{\mathbf{n}' \cdot \mathbf{n}'} w' \mathbf{n}' \text{ if } \mathbf{n}' \cdot \mathbf{n}' \neq 0 \tag{Equation 3}$$

where  $\mathbf{n}'$  and  $w'$  are derivatives of  $\mathbf{n}$  and  $w$  with respect to the relevant independent variable, respectively. In particular,  $\mathbf{n} = \mathbf{n}(\theta)$  and  $w = w(\theta)$  in the following ellipse example, while  $\mathbf{n} = \mathbf{n}(s)$  and  $w = w(s)$  in the Willmore surface approximations. Higher dimensional analogues of Equation 3 have been used as spherical parameterizations for certain minimal surfaces.<sup>13-14</sup> As in those works, it is convenient to interpret  $\mathbf{x}$ , defined by Equation 3, as a mapping from the unit circle,  $S^1$ , to  $\mathbb{R}^2$  with the generating curve as the image. For some simple geometries, this is a well-defined map. In particular, we work through an example to verify Equation 3 for an ellipse. Figure 2 is an illustration for how  $S^1$  is deformed, via  $\mathbf{x}$ , into an ellipse. Unfortunately, for Y-shape and dumbbell generating curves, a single map  $\mathbf{x} : S^1 \rightarrow \mathbb{R}^2$  is insufficient to produce the entire generating curve. However, we explain how formulae can be derived for Willmore surfaces by using Equation 3.

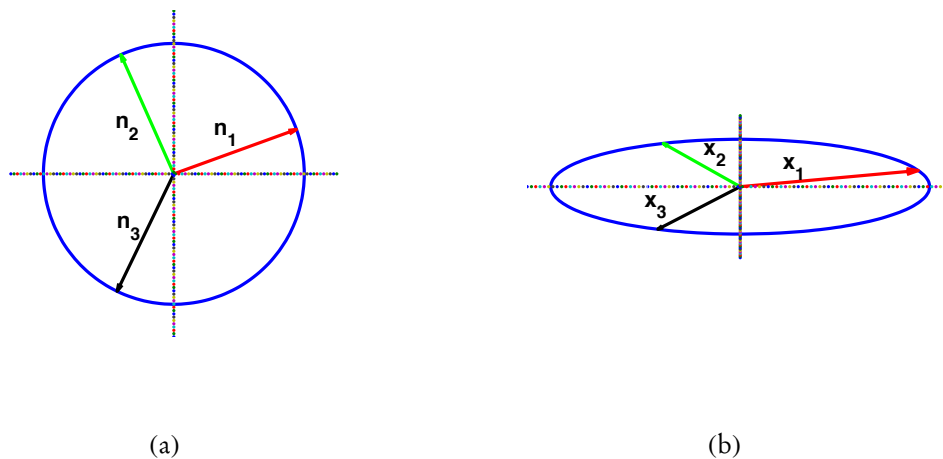


Figure 2. (a)  $S^1$  with normal vectors  $\mathbf{n}_i, i = 1, 2, 3$  (b) Ellipse with images  $\mathbf{x}(\mathbf{n}_i) = \mathbf{x}_i, i = 1, 2, 3$

Ellipse Example

To show how Equation 3 can be used as a representation for the shape of a generating curve  $\mathbf{x}$ , we will consider an ellipse parameterized by  $\mathbf{x} = \langle a \cos \theta, b \sin \theta \rangle$  for  $\theta \in [0, 2\pi]$  and fixed  $a, b \in (0, \infty)$ . One can compute the unit normal vector

$$\mathbf{n} = \frac{1}{\sqrt{b^2 \cos^2 \theta + a^2 \sin^2 \theta}} \langle b \cos \theta, a \sin \theta \rangle$$

From Equation 2, the support function for the ellipse is

$$w = \frac{ab}{\sqrt{b^2 \cos^2 \theta + a^2 \sin^2 \theta}}$$

The derivative of the support function is

$$w' = \frac{dw}{d\theta} = \frac{ab(b^2 - a^2) \cos \theta \sin \theta}{(b^2 \cos^2 \theta + a^2 \sin^2 \theta)^{3/2}}$$

One can also compute the derivative of  $\mathbf{n}$ . As  $\mathbf{n}$  is a vector, the derivative is computed component-wise. The derivative of the first component is found by the quotient rule:

$$\begin{aligned} \frac{d}{d\theta} \left( \frac{b \cos \theta}{(b^2 \cos^2 \theta + a^2 \sin^2 \theta)^{1/2}} \right) &= \frac{(b^2 \cos^2 \theta + a^2 \sin^2 \theta)^{1/2}(-b \sin \theta) - \frac{1}{2}(b^2 \cos^2 \theta + a^2 \sin^2 \theta)^{-1/2}(2b^2 \cos \theta(-\sin \theta) + 2a^2 \sin \theta \cos \theta)(b \cos \theta)}{(b^2 \cos^2 \theta + a^2 \sin^2 \theta)} \\ &= \frac{(b^2 \cos^2 \theta + a^2 \sin^2 \theta)(-b \sin \theta) - (b^2 \cos \theta(-\sin \theta) + a^2 \sin \theta \cos \theta)(b \cos \theta)}{(b^2 \cos^2 \theta + a^2 \sin^2 \theta)^{3/2}} \\ &= \frac{-a^2 b \sin^2 \theta \sin \theta - a^2 b \sin \theta \cos^2 \theta}{(b^2 \cos^2 \theta + a^2 \sin^2 \theta)^{3/2}} \\ &= \frac{-a^2 b \sin \theta}{(b^2 \cos^2 \theta + a^2 \sin^2 \theta)^{3/2}} \end{aligned}$$

Likewise, the derivative of the second component can be computed as

$$\begin{aligned} \frac{d}{d\theta} \left( \frac{a \sin \theta}{(b^2 \cos^2 \theta + a^2 \sin^2 \theta)^{1/2}} \right) &= \frac{(b^2 \cos^2 \theta + a^2 \sin^2 \theta)^{1/2}(a \cos \theta) - \frac{1}{2}(b^2 \cos^2 \theta + a^2 \sin^2 \theta)^{-1/2}(2b^2 \cos \theta(-\sin \theta) + 2a^2 \sin \theta \cos \theta)(a \sin \theta)}{(b^2 \cos^2 \theta + a^2 \sin^2 \theta)} \\ &= \frac{(b^2 \cos^2 \theta + a^2 \sin^2 \theta)(a \cos \theta) - (b^2 \cos \theta(-\sin \theta) + a^2 \sin \theta \cos \theta)(a \sin \theta)}{(b^2 \cos^2 \theta + a^2 \sin^2 \theta)^{3/2}} \\ &= \frac{b^2 a \cos^2 \theta \cos \theta + b^2 a \cos \theta \sin^2 \theta}{(b^2 \cos^2 \theta + a^2 \sin^2 \theta)^{3/2}} \\ &= \frac{b^2 a \cos \theta}{(b^2 \cos^2 \theta + a^2 \sin^2 \theta)^{3/2}} \end{aligned}$$

We see that

$$\mathbf{n}' = \frac{d\mathbf{n}}{d\theta} = \frac{1}{(b^2 \cos^2 \theta + a^2 \sin^2 \theta)^{3/2}} \langle -a^2 b \sin \theta, b^2 a \cos \theta \rangle$$

For the ellipse, we note  $\mathbf{n}' \cdot \mathbf{n}' \neq 0$  for any  $\theta$ . Thus, we can check the validity of Equation 3 for the ellipse. First,

$$w\mathbf{n} = \frac{ab \langle b \cos \theta, a \sin \theta \rangle}{b^2 \cos^2 \theta + a^2 \sin^2 \theta} \tag{Equation 4.}$$

The second term in Equation 3 is

$$\begin{aligned} \frac{1}{\mathbf{n}' \cdot \mathbf{n}'} w' \mathbf{n}' &= \frac{(b^2 \cos^2 \theta + a^2 \sin^2 \theta)^3}{a^4 b^2 \sin^2 \theta + b^4 a^2 \cos^2 \theta} \left( \frac{ab(b^2 - a^2) \cos \theta \sin \theta}{(b^2 \cos^2 \theta + a^2 \sin^2 \theta)^{3/2}} \right) \frac{\langle -a^2 b \sin \theta, b^2 a \cos \theta \rangle}{(b^2 \cos^2 \theta + a^2 \sin^2 \theta)^{3/2}} \\ &= \frac{(b^2 - a^2) \cos \theta \sin \theta \langle -a^2 b \sin \theta, b^2 a \cos \theta \rangle}{ab(a^2 \sin^2 \theta + b^2 \cos^2 \theta)} \end{aligned} \tag{Equation 5.}$$

After distributing and adding componentwise, Equation 4 and Equation 5 yield

$$\mathbf{x} = \frac{\langle ab^2 \cos \theta - ab^2 \sin^2 \theta \cos \theta + a^3 \sin^2 \theta \cos \theta, a^2 b \sin \theta + b^3 \cos^2 \theta \sin \theta - a^2 b \cos^2 \theta \sin \theta \rangle}{a^2 \sin^2 \theta + b^2 \cos^2 \theta}$$

Upon factoring and applying the identity  $\sin^2 \theta + \cos^2 \theta = 1$ , we obtain

$$\begin{aligned} \mathbf{x} &= \frac{1}{a^2 \sin^2 \theta + b^2 \cos^2 \theta} \langle a \cos \theta (b^2 \cos^2 \theta + a^2 \sin^2 \theta), b \sin \theta (a^2 \sin^2 \theta + b^2 \cos^2 \theta) \rangle \\ &= \langle a \cos \theta, b \sin \theta \rangle \end{aligned}$$

As mentioned above, given  $w$ , one can interpret  $\mathbf{x} = \mathbf{x}_w$  from Equation 3 as a mapping  $\mathbf{x} : S^1 \rightarrow \mathbb{R}^2$  by  $\mathbf{x}_w(\mathbf{n}) = w\mathbf{n} + \frac{1}{\mathbf{n}' \cdot \mathbf{n}'} w' \mathbf{n}'$ . In Figure 2, we highlight this approach by showing three normal vectors  $\mathbf{n}_1, \mathbf{n}_2$ , and  $\mathbf{n}_3$  and their respective images  $\mathbf{x}_1, \mathbf{x}_2$ , and  $\mathbf{x}_3$  in the ellipse. We view the function  $\mathbf{x}_w$  as deforming  $S^1$  in Figure 2(a) to the ellipse in Figure 2(b).

Approximations from Matlab

In this section, we give the closed-form approximate formulae for our Y-shape and dumbbell Willmore surface generating curves. We also check the validity of Equation 3 for the Y-shape Willmore surface. To derive the desired formulae, we use Matlab to approximate  $w$  and  $\psi + (\pi/2)$  as polynomials. Our numerical solution from Matlab provides arrays for  $\mathbf{x}$  and  $\psi$ , and thus, we can form  $\mathbf{n} = \langle \sin(\psi), -\cos(\psi) \rangle$ . Matlab can then compute an array for the support function  $w = \mathbf{x} \cdot \mathbf{n}$  (see Figure 3(a)). To obtain the desired approximate formulae for  $\mathbf{x}$ , we use Matlab to approximate  $w$  with a

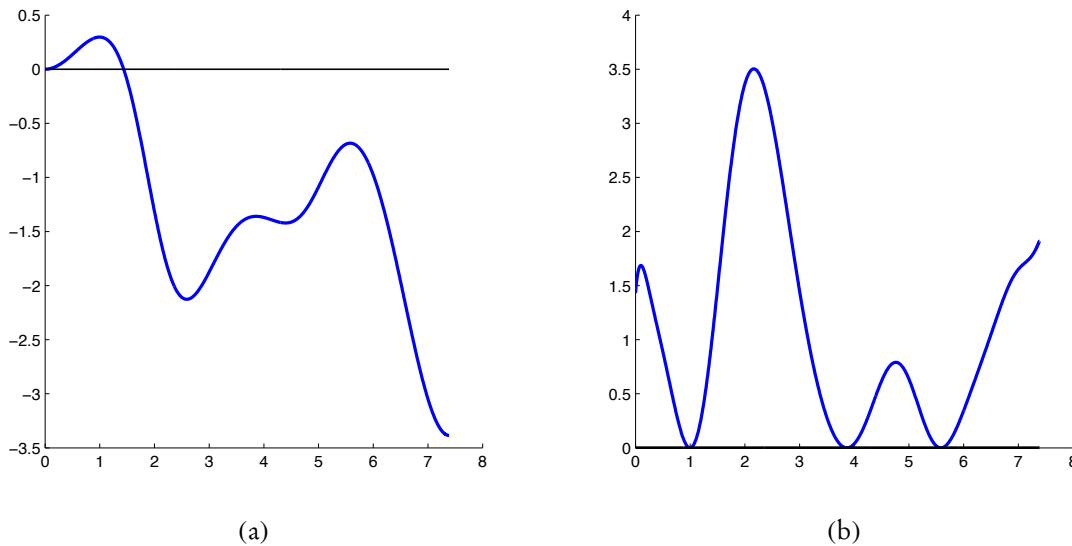


Figure 3. (a) Support function for Y-shape (b)  $\mathbf{n}' \cdot \mathbf{n}'$  with zeros at  $s \approx 0.9985, s \approx 3.8640, s \approx 5.5841$

polynomial. Coefficients for the polynomial approximation of  $w$  were determined by the expression ‘polyfit’, which returns the coefficients for a polynomial of any desired degree. In general, the approximation given by ‘polyfit’ gets better as the degree increases. One way to measure the accuracy of the approximation is to compute the total squared error, i.e., compute  $\sum_{i=1}^{1017} (w_i - w_{p,i})^2$ , where  $w_i$  is the  $i$ th component of the array  $w$  and  $w_{p,i}$  is the  $i$ th component of the corresponding polynomial approximation as given by ‘polyfit’ for some chosen degree. To choose the degree, we considered the total squared error for various degrees, in addition to visually inspecting superimposed plots of  $w$  and  $w_p$ . Using the 16th degree polynomial yields a total squared error less than 4%, a tolerance that we deemed acceptable. Of course, greater accuracy could be obtained with a higher degree polynomial approximation. For example, a 19th degree polynomial can be used to achieve a total squared error less than 1%. Ultimately, we chose a 16th degree polynomial since it was the lowest degree for which the approximate polynomial appeared nearly indistinguishable from  $w$ . The approximation is  $w \approx \sum_{i=0}^{16} c_i s^i$ , where the coefficients  $c_i$  are given in Table 1. With the coefficients for the polynomial approximation of  $w$ , one can calculate coefficients for a polynomial approximation of  $w'$  by computing  $ic_i$  as the coefficient of  $s^{i-1}$

$$w' = \frac{dw}{ds} \approx \sum_{i=1}^{16} ic_i s^{i-1}$$

A similar approach was taken to obtain an approximation for  $\theta = \psi + (\pi/2)$ , which can then be used to approximate  $\mathbf{n}$  as a function of  $s$ . In particular,  $\theta$  is found from Matlab by taking the solution  $\psi(s)$  (as pictured in Figure 1) and adding  $\pi/2$ . We add  $\pi/2$  because  $\psi$  is the angle between the horizontal and tangent lines of the generating curve, while we desire an approximation for the angle between the horizontal and normal lines of the generating curve. For the approximation, we find

$$\theta(s) = \psi(s) + \pi/2 \approx \sum_{i=0}^{16} d_i s^i \tag{Equation 6.}$$

where the coefficients  $d_i$  are given in Table 1. This polynomial allows us to obtain an approximate formula for  $\mathbf{n}$  in terms

Term	Coefficient for $w$	Coefficient for $\theta$
$s^0$	$c_0 = -0.000060771569692$	$d_0 = 1.570924108727812$
$s^1$	$c_1 = 0.114602595804498$	$d_1 = 1.196236274933391$
$s^2$	$c_2 = -1.719844524602488$	$d_2 = 1.241628057733661$
$s^3$	$c_3 = 15.603335003104629$	$d_3 = -6.569163020942945$
$s^4$	$c_4 = -49.235439770081733$	$d_4 = 15.219754968954797$
$s^5$	$c_5 = 85.851964954476983$	$d_5 = -22.249839707112130$
$s^6$	$c_6 = -93.192274800396135$	$d_6 = 20.931676370762279$
$s^7$	$c_7 = 66.572113028538610$	$d_7 = -13.454835395052019$
$s^8$	$c_8 = -32.643107035876724$	$d_8 = 6.171998900701146$
$s^9$	$c_9 = 11.327063427562599$	$d_9 = -2.068316556605748$
$s^{10}$	$c_{10} = -2.832752329974763$	$d_{10} = 0.510835578073774$
$s^{11}$	$c_{11} = 0.513673827418474$	$d_{11} = -0.092743939106679$
$s^{12}$	$c_{12} = -0.067051360050457$	$d_{12} = 0.012205101258158$
$s^{13}$	$c_{13} = 0.006149427856176$	$d_{13} = -0.001130878451232$
$s^{14}$	$c_{14} = -0.000376443328925$	$d_{14} = 0.000069864759188$
$s^{15}$	$c_{15} = 0.000013820393660$	$d_{15} = -0.000002580798593$
$s^{16}$	$c_{16} = -0.000000230250017$	$d_{16} = 0.000000043089161$

Table 1. Coefficients for  $w$  and  $\theta$  for a Y-shape

of the arc length on the generating curve. For convenience, we parameterize the unit circle as

$$\mathbf{n} = \langle -\cos(\theta), -\sin(\theta) \rangle \tag{Equation 7}$$

with  $0 \leq \theta \leq 2\pi$ . The negative value indicates that the normal vector is pointed toward the inside of the generating curve. As is evident from Equation 3, an expression for  $\mathbf{n}'$  is needed. Upon differentiating Equation 7 with respect to  $s$ , we find

$$\mathbf{n}' = \frac{d\mathbf{n}}{ds} = \langle \sin(\theta), -\cos(\theta) \rangle \theta' \tag{Equation 8}$$

where  $\theta' = \frac{d\theta}{ds}$ . We approximate  $\theta'$  from Equation 6 as a 15th degree polynomial with  $id_i$  as the coefficient of  $s^{i-1}$ . Now, using our approximations for  $w$ ,  $w'$ ,  $\mathbf{n}$ , and  $\mathbf{n}'$ , the formula for the generating curve of the Y-shape Willmore surface is

$$\mathbf{x}(s) = w(s)\mathbf{n}(s) + \frac{1}{\mathbf{n}'(s) \cdot \mathbf{n}'(s)} w'(s)\mathbf{n}'(s) \tag{Equation 9}$$

with domain  $\{s \in [0, L] \mid \mathbf{n}'(s) \cdot \mathbf{n}'(s) \neq 0\}$ . See Figure 3(b) for a graph of  $\mathbf{n}' \cdot \mathbf{n}'$  showing zeros at approximately  $s = 0.998476759700923$ ,  $s = 3.863998297698298$ , and  $s = 5.584116014650597$ . For our Y-shape,  $L$  is found to be 7.385119679927381. While the formula for  $\mathbf{x}(s)$  in Equation 9 is only valid for this one Y-shape, the procedure for creating  $\mathbf{x}$  holds regardless of the particular bio-membrane shape. Figure 4(a) shows the generating curve that we obtained from Matlab as a solution to the Euler-Lagrange equations. The figure also contains a plot of our approximate  $\mathbf{x}$  from Equation 9. The agreement is excellent. In fact, the images are indistinguishable. The points not on the curve correspond to arc lengths close to those that make  $\mathbf{n}' \cdot \mathbf{n}' = 0$ , thus giving erroneous results.

To further confirm the validity of our formula, we checked the approximation  $\mathbf{x}(2.0554) \approx \langle r(2.0554), z(2.0554) \rangle$ . To this end,  $w(2.0554)$  was determined using Matlab with command ‘polyval’ which gave the numerical value of -1.44600781990. The derivative  $w'(2.0554)$  was computed numerically with ‘polyval’ which resulted in the numerical value of -2.34828659727. These last two values are rounded for ease of exposition. For the normal vector, Matlab expression ‘polyval’ approximated  $\theta(2.0554)$ . This resulted in an approximation for  $\mathbf{n}$ :

$$\mathbf{n}(2.0554) \approx \langle -0.358125822681700, -0.933673334270908 \rangle$$

which is in good agreement with the normal vector field at the corresponding location  $s \approx 2.0554$  on the curve (see Figure 1). For  $\mathbf{n}'$ , we took a similar approach with the derivative of Equation 8 while still using Matlab expression ‘polyval’ for  $\theta(2.0554)$ . Ultimately, the final value of  $\mathbf{n}'$  is

$$\mathbf{n}'(2.0554) \approx \langle -1.732347541734692, 0.664470501386673 \rangle$$

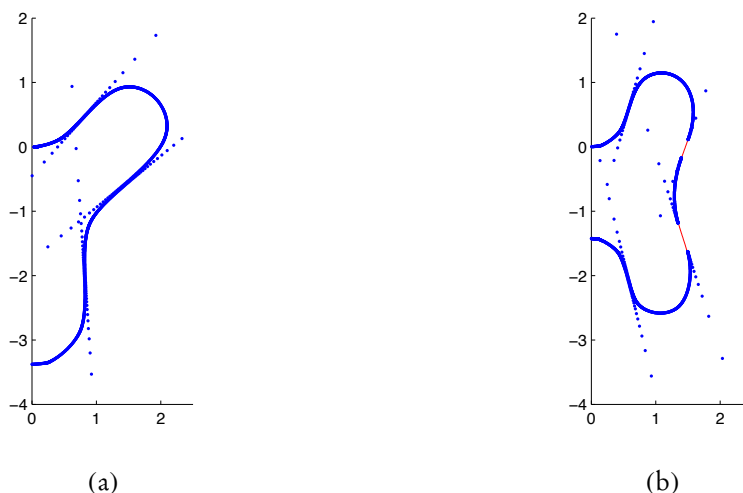


Figure 4. Generating curve from Matlab and approximate solution  $\mathbf{x}$ . (a) Y-shape (b) Dumbbell

Variable	Value at $s \approx 2.0554$
$w$	-1.446007819900795
$w'$	-2.348286597274282
$\mathbf{n}$	$\langle -0.358125822681700, -0.933673334270908 \rangle$
$\mathbf{n}'$	$\langle -1.732347541734692, 0.664470501386673 \rangle$
$r$	1.732183240619059
$z$	0.887509330469256

Table 2. Values provided by Matlab for variables  $w, w', \mathbf{n}, \mathbf{n}'$  at  $s \approx 2.0554$ .

All of these values are summarized in Table 2. When substituting the values from Table 2 into Equation 9, the numerical approximation is

$$\begin{aligned} \mathbf{x}(2.0554) &= -1.4460 \langle -0.3581, -0.9337 \rangle + \frac{(-2.3483) \langle -1.7323, 0.6645 \rangle}{\langle -1.7323, 0.6645 \rangle \cdot \langle -1.7323, 0.6645 \rangle} \\ &= \langle 1.699549341071895, 0.896839701002235 \rangle \end{aligned}$$

where we rounded to four decimal places for ease of exposition. The values of  $r$  and  $z$  at  $s \approx 2.0554$  are 1.732183240619059 and 0.887509330469256, respectively. Thus, we see that  $\mathbf{x}$  is in fact a decent approximation to the numerical solution  $\langle r, z \rangle$ . In particular, at  $s \approx 2.0554$ , our approximate formula varies from the numerical solution by  $\|\mathbf{x} - \langle r, z \rangle\| \approx 0.033941526393742$ .

For completeness, we note that coefficients for  $w$  and  $\theta$  can be obtained in order to compute an approximate formula  $\mathbf{x}$  for a dumbbell shape Willmore surface. For a dumbbell, we used a 23rd degree polynomial to approximate  $w$ . The method for obtaining  $\mathbf{x}$  is the same as above. Figure 4(b) shows the generating curve from the solution of the Euler-Lagrange equations and the approximate  $\mathbf{x}$ . Again, we see excellent agreement when  $\mathbf{n}' \cdot \mathbf{n}' \neq 0$ . For the dumbbell,  $\mathbf{n}' \cdot \mathbf{n}' = 0$  at four values of  $s$ . While the image in Figure 4(b) has two gaps in the approximate formula  $\mathbf{x}$ , other results with different numerical integration tolerances lead to slightly different pictures with one or zero gaps. We included Figure 4(b) with two gaps in order to highlight the regions of the curve where  $\mathbf{n}$  is essentially constant and thus  $\mathbf{n}' \cdot \mathbf{n}' = 0$ .

### CONCLUSIONS

Y-shape and dumbbell shape lipid bilayers were computed by minimizing Helfrich’s bending energy with buoyancy, subject to area and volume constraints. When analyzing the Y-shape, it is understood that the support function for this bio-membrane was approximated by a 16th degree polynomial (Table 1). Furthermore, when analyzing the dumbbell shape, the support function was approximated by a 23rd degree polynomial. Within a total squared error less than 4%, these polynomials approximated  $w$  and  $\theta$  which were then used to obtain the generating curves for both bio-membrane shapes.

Ultimately, we interpret  $\mathbf{x}$  as a mapping to show how a unit circle is deformed into the generating curve. However, this expression for the generating curve in terms of  $w$  and  $\mathbf{n}$  was only partially verified, owing to the fact that **Equation 3** depended on  $\mathbf{n}' \cdot \mathbf{n}' \neq 0$ . With this restriction, the equation failed at certain locations along the generating curves of Y-shape and dumbbell bio-membranes. Our systematic approach can provide a way of interpreting and examining other bio-membrane shapes of interest. For example, one might use the polynomial approximation for  $w$  as a way to determine a formula for the Gaussian and mean curvatures of Willmore surfaces. Further study remains on this approximation approach before such applications are fully understood.

#### ACKNOWLEDGEMENTS

The authors thank the Niagara University Research Council for financial support through the 2014-2015 Research Support Grant.

#### REFERENCES

1. Brooker, R. et. al. (2008) *Biology: Second Edition*, The McGraw Hill Companies, New York.
2. Baginski, F., Croce, R., Gillmor, S., and Krause, R. (2014) Numerical investigations of the role of curvature in strong segregation problems on a given surface, *Appl. Math. Comput.* **227**, 399–411.
3. Baumgart, T., Hess, S. T., and Webb, W. W. (2003) Imaging coexisting fluid domains in biomembrane models coupling curvature and line tension, *Nature* **425**, 821–824.
4. Gillmor, S., Lee, J., and Ren, X. (2011) The role of Gauss curvature in a membrane phase separation problem *Phys. D* **240**, No. 24, 1913–1927
5. Helfrich, W. (1973) Elastic properties of lipid bilayers: theory and possible experiments, *Z. Naturforsch* **28 c**, 693–703.
6. Seifert, U., Berndl, K., and Lipkowsky, R. (1991) Shape transformations of vesicles: phase diagram for spontaneous curvature and bilayer-coupling models, *Phys. Rev. A* **44** No. 2, 1182–1202.
7. Blyth, M. G., and Pozrikidis, C. (2004) Solution space of axisymmetric capsules enclosed by elastic membranes, *Eur. J. Mech. A Solids* **23**, 877–892.
8. Luke, J. (1982) A method for the calculation of vesicle shapes, *SIAM J. Appl. Math.* **42**, 333–345.
9. Duelling, H., and Helfrich, W. (1976) The curvature elasticity of fluid membranes: a catalogue of vesicle shapes, *Le Journal De Physique* **37**, 1335–1345.
10. Mladenov, I. M. (2002) New solutions of the shape equation, *Eur. Phys. J. B* **29**, 327–330.
11. Tu, Z. C., and Ou-Yang, Z. C. (2004) A geometric theory on the elasticity of bio-membranes, *J. Phys. A: Math. Gen.* **37**, 11407–11429.
12. Stoker, J. J. (1969) *Differential Geometry*, John Wiley & Sons, Inc., New York.
13. Baginski, F., and Ramos Batista, V. (2011) Solving period problems for minimal surfaces with the support function, *Adv. Appl. Math. Sci.* **9**, 85–114.
14. Baginski, F. (2002) Special functions on the sphere with applications to minimal surfaces, *Adv. in Appl. Math.* **28**, 360–394.

**ABOUT THE STUDENT AUTHOR**

Phillip Galbo graduated from Niagara University in 2015 with a B.S. in Biology and a minor in Chemistry. The research in this manuscript began during his Sophomore year and was completed during his Senior year. In 2014, Phillip was inducted into the national biological honor society for undergraduates. Upon graduating, Phillip accepted a research position at Roswell Park Cancer Institute in the Department of Neuro-Oncology where he is currently pursuing his passion for oncological research.

**PRESS SUMMARY**

Bio-membrane shapes are calculated by minimizing a bending energy with area and volume constraints. Many different minimizing shapes are known to exist, including Y-shapes and dumbbells. However, exact solutions remain elusive. We describe a method to use support functions to give approximate closed-form formulae for such shapes, thus offering a way to evaluate and analyze the wide array of bio-membrane shapes.



# Preparation of *t*-Butyldimethylphosphine Borane and *t*-Butyldiethylphosphine Borane by Selective Grignard Reagent Substitution of Phosphorus Trichloride

Auston G. Butterfield, Matthew B. Prater, and Nathan S. Werner\*

Department of Physical Science, Southern Utah University, Cedar City, Utah

Students: [austonbutterfield@hotmail.com](mailto:austonbutterfield@hotmail.com), [mattp222@gmail.com](mailto:mattp222@gmail.com)

Mentor: [nathanwerner@suu.edu](mailto:nathanwerner@suu.edu)\*

## ABSTRACT

The synthesis of differentially substituted trialkylphosphine boranes from the selective substitution reaction of Grignard reagents with phosphorus trichloride in a single reaction flask was studied. The reaction temperature, stoichiometric loading of the first equivalent of Grignard reagent and reaction time were found to be important for maximizing the yield and selectivity of the reaction. Reaction conditions were optimized to achieve maximum yield of *t*-butyldiethylphosphine borane. The optimized conditions were applied to the syntheses of *t*-butyldiethylphosphine borane and *t*-butyldimethylphosphine borane, which provided 60% and 62% isolated yields respectively. Products were characterized with mass spectrometry, infrared spectroscopy,  $^1\text{H}$ ,  $^{13}\text{C}$ , and  $^{31}\text{P}$  nuclear magnetic resonance spectroscopy.

## KEYWORDS

Synthesis; Trialkylphosphine; Grignard Reagent; Selective; Substitution Reaction; *t*-Butyldiethylphosphine Borane; *t*-Butyldimethylphosphine Borane; Phosphorus Trichloride

## INTRODUCTION

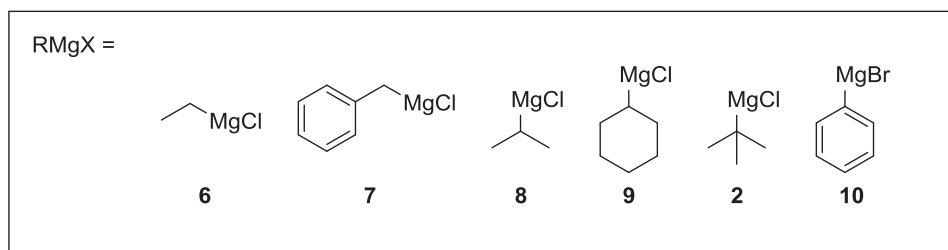
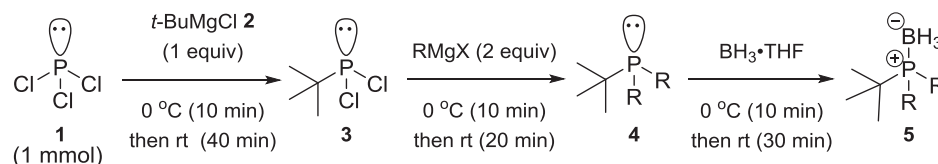
The reactions of Grignard reagents with phosphorus trihalides have been known for over a century.<sup>1-3</sup> Moreover, the alkylated phosphorus products of these reactions are useful as ligands in many transition metal-catalyzed transformations.<sup>3-8</sup> Previous to this work, it has been common to isolate the alkylchlorophosphine or purchase it from commercial sources before substituting the remaining two chlorides with alkyl nucleophiles.<sup>10-12</sup> For example, *t*-butyldimethylphosphine borane can be prepared from *t*-butyldichlorophosphine and MeMgBr in 60% yield.<sup>13</sup> However, general procedures for the selective one-pot substitution of different alkyl Grignard reagents with phosphorus trichloride to form differentially substituted trialkylphosphines remain unknown.<sup>14</sup> This is despite the fact that this represents the most straightforward way to prepare differentially substituted trialkylphosphines from inexpensive phosphorus trichloride. Herein we report our studies on the synthesis of *t*-butyldimethylphosphine borane and *t*-butyldiethylphosphine borane by selective Grignard reagent substitution reactions with phosphorus trichloride.

Borane protected trialkylphosphines were used in this work because electron rich trialkylphosphines are reactive with oxygen which makes their handling difficult. Fortunately, borane can be used to protect the readily oxidizable phosphorus atom by simple Lewis base/Lewis acid complexation.<sup>16</sup> This technique has multiple advantages: (1) the phosphine can be protected *in situ* by reaction with borane in tetrahydrofuran (THF), (2) the phosphine-borane adduct is stable to the exposure of ambient oxygen, silica gel chromatography, and aqueous acids; which enables the handling and purification of the phosphine-borane adducts, (3) the borane protecting group can be readily removed by reaction with a Lewis base<sup>17</sup> or strong anhydrous acid.<sup>18,19</sup>

## RESULTS AND DISCUSSION

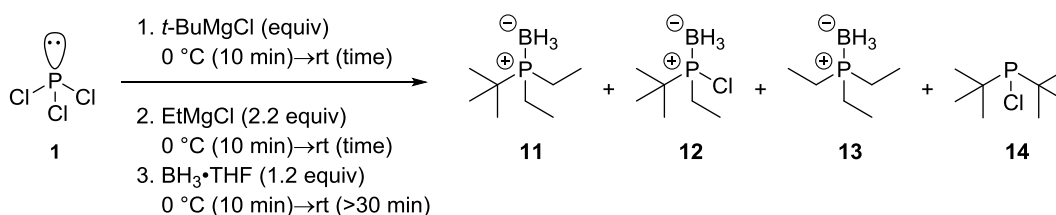
Initial studies on the selective addition of Grignard reagents to  $\text{PCl}_3$  1 began with the reaction of *t*-BuMgCl 2 and 1 (Scheme 1). The Grignard reagent *t*-BuMgCl was chosen because the preparation of *t*-BuPCl<sub>2</sub> suggested that the large size of *t*-BuMgCl would allow for selectivity between the mono, di, and trisubstitution reaction.<sup>11</sup> A second Grignard reagent was then added to substitute the remaining two chlorine atoms and the phosphorus atom was protected with borane prior to workup and analysis by gas chromatography-mass spectrometry (GC-MS). Preliminary experiments evaluated a variety of Grignard reagents as nucleophiles in the second substitution reaction. Grignard reagents with primary, secondary and tertiary  $\text{sp}^3$  hybridized C-Mg bonds, as well as

$sp^2$  hybridized C–Mg bonds were evaluated. Of these initially evaluated Grignard reagents, only EtMgCl provided clean production of the desired *t*-butyldialkylphosphine **5**. Therefore, EtMgCl was chosen as the second Grignard reagent for studies directed to optimize the yield of the selective substitution reaction.



Scheme 1.

The selective substitution reaction of one equivalent of *t*-BuMgCl and two equivalents of EtMgCl **6** with  $PCl_3$  was optimized by evaluating reagent equivalents and the incubation time between reagent additions (**Table 1**). In all experiments, reagents were added to the reaction mixture once it had been cooled to  $0^\circ\text{C}$  in an ice bath.<sup>20</sup> After each reagent addition, the reaction mixture was allowed to stir for 10 min at  $0^\circ\text{C}$  before warming to room temperature for the time specified. The reaction mixture was again cooled to  $0^\circ\text{C}$  before the next reagent was added. An experiment following these standard conditions provided 88% of *t*-butyldiethylphosphine borane **11** by GC-MS analysis of the crude reaction mixture (entry 1). Allowing the reaction to immediately warm to room temperature only after the addition of *t*-BuMgCl provided 71% of **11** (entry 2). In addition, allowing reactions to stir for ten minutes at  $0^\circ\text{C}$  prior to warming to room temperature decreased the amount of **13** produced, which later proved to be inseparable from **11** via chromatography. These results suggest that the first substitution reaction time of 10 min at  $0^\circ\text{C}$  is important to achieve selectivity for monoaddition. Next, the stoichiometric loading of *t*-BuMgCl (1–1.25 equiv) with respect to **1** was examined (compare entries 1, 3, and 4). The yield of **11** was found to be similar when 1.0 or 1.25 equiv of *t*-BuMgCl was used, however 1.0 equiv of *t*-BuMgCl produced less of the diaddition reaction product **14**.<sup>5</sup> The reaction times at room temperature after the addition of *t*-BuMgCl were then studied (entries 5–9). In these experiments, the yield of **11** increased only slightly from 88% to 90% as the reaction time was increased up to 40 minutes. However, at 60 minutes the yield of **11** began to decrease and production of **14** increased. The reaction times at room temperature after the addition of EtMgCl were also studied (entries 10–14). Unlike the reaction times associated with the addition of *t*-BuMgCl, reaction times of greater than 20 minutes after the addition of EtMgCl showed no significant change in the yield of **11**.



Entry	<i>t</i> -BuMgCl (equiv)	<i>t</i> -BuMgCl time at rt (min)	EtMgCl time at rt (min)	11 (%)	12 (%)	13 (%)	14 (%)
1	1.0	15	15	88	10	2	0
2 <sup>c</sup>	1.0	15	15	71	14	15	0
3	1.1	15	15	89	8	trace	3
4	1.25	15	15	90	trace	trace	10
5	1.0	20	15	88	4	8	0
6	1.0	40	15	90	4	6	0
7	1.0	60	15	82	6.5	7	4.5
8	1.0	80	15	76	5	6	13
9	1.0	100	15	68	6	8	18
10	1.0	40	20	88	0	12	0
11	1.0	40	40	87	0	13	0
12	1.0	40	60	88	0	12	0
13	1.0	40	80	88	0	12	0
14	1.0	40	100	87	0	13	0

Table 1. Optimization of the Selective Grignard Reagent Substitution Reaction.<sup>a,b</sup>

<sup>a</sup>Structure of **12**, **13**, and **14** tentatively assigned by analysis of GC-MS data. <sup>b</sup>Relative peak area ratios. 0°C→room temperature immediately after drop-wise addition of *t*-BuMgCl.

An additional set of experiments to evaluate Grignard reagent scope were performed using the previously optimized reaction conditions. In these experiments, *t*-butyldichlorophosphine was prepared *in situ* by reaction of PCl<sub>3</sub> and *t*-BuMgCl at 0°C for 10 min and warming to room temperature and stirring an additional 40 min. The reaction was cooled to 0°C and a Grignard reagent (2.0 equiv) from **Figure 1** was then added drop-wise by syringe. The reaction was stirred for 10 min at 0°C before warming to room temperature and stirring an additional 20 min. The reaction was cooled to 0°C and BH<sub>3</sub>·THF was added drop-wise by syringe. The reaction was again stirred for 10 min at 0°C before warming to room temperature and stirring an additional 3 h. In addition to EtMgCl, MeMgCl **15** was also found to provide clean production of the desired *t*-butyldialkylphosphine borane by GC-MS analysis of crude reaction aliquots under the optimized reaction conditions. The optimized reaction conditions were then applied to the 5 mmol preparation of *t*-butyldiethylphosphine borane **11** and *t*-butyldimethylphosphine borane **16**.

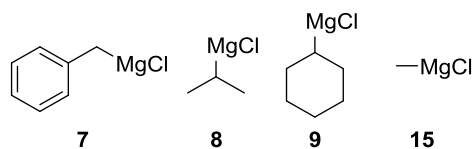
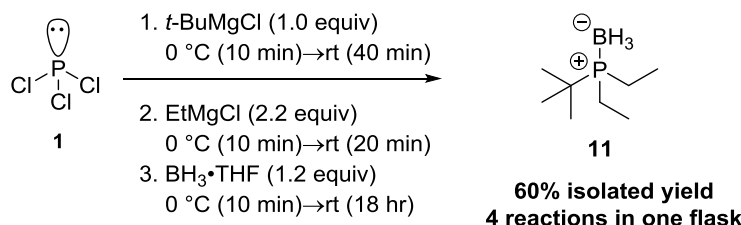


Figure 1. Grignard reagents evaluated under the optimized reaction conditions.

Procedure for the Synthesis of *t*-Butyldiethylphosphine Borane (11)

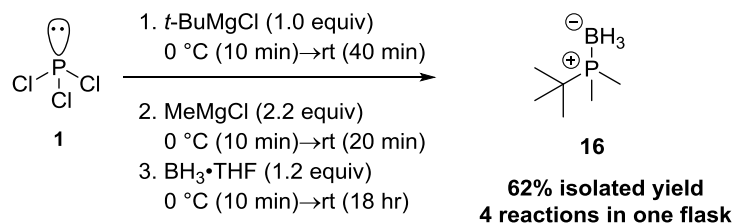
Scheme 2.

To an oven dried, 50-mL, single neck, round-bottomed flask, containing a magnetic stir bar, capped with a septum that was bound with copper wire, and then evacuated and filled with argon ( $\times 3$ ) was added dry THF by syringe. The solvent was purged for 20 min with argon. The flask was cooled to  $0^\circ\text{C}$  using an ice bath, followed by the addition of  $\text{PCl}_3$  (436  $\mu\text{L}$ , 5 mmol) by syringe.  $t\text{-BuMgCl}$  ([1.7], 2.94 mL, 1.0 equiv) was added drop-wise by syringe and allowed to stir at  $0^\circ\text{C}$  for 10 min. The reaction was warmed to room temperature by removal from the cooling bath and stirred for 40 min. The reaction was cooled to  $0^\circ\text{C}$  and  $\text{EtMgCl}$  ([2.7], 4.07 mL, 2.2 equiv) was added drop-wise by syringe. The reaction was allowed to stir at  $0^\circ\text{C}$  for 10 min, warmed to room temperature, and stirred an additional 20 min. The mixture was cooled to  $0^\circ\text{C}$  and  $\text{BH}_3 \cdot \text{THF}$  ([1.0], 6.0 mL, 1.2 equiv) was added drop-wise by syringe. The reaction was allowed to stir at  $0^\circ\text{C}$  for 10 min, warmed to room temperature, and stirred at least 30 min. The mixture was quenched by slow addition to a stirred solution of 1 M HCl (60 mL) at  $0^\circ\text{C}$ . The resulting mixture was extracted with  $\text{EtOAc}$  ( $3 \times 10$  mL). The combined organic extracts were washed with brine ( $3 \times 20$  mL), and dried over anhydrous  $\text{Na}_2\text{SO}_4$ . The solution was concentrated by rotary evaporation at  $50^\circ\text{C}$  and 140 torr. Residual solvent was further removed under vacuum at 2 torr for 20 min.

The crude product was purified by silica gel column chromatography. The column was prepared using 40 g of silica gel suspended in hexane. The product was loaded neat and the flask was rinsed with minimal dichloromethane. An eluent consisting of a concentration gradient of 100 mL hexane, 100 mL 1%  $\text{EtOAc}$ /hexane, and 100 mL 2%  $\text{EtOAc}$ /hexane was used to elute the product. Fractions (2-3 mL each) were collected and analyzed by thin-layer chromatography. Fractions containing the desired product were combined and concentrated as described above to provide 480 mg (60%) of **11** as a white, crystalline solid (Scheme 2). The product was stable to exposure to ambient oxygen and was stored in a refrigerator for weeks with no discernible change in purity or reactivity.

Data for *t*-Butyldiethylphosphine Borane (11)

<u>mp</u> :	42.7–43.5 $^\circ\text{C}$
<u><math>^1\text{H NMR}</math></u> :	(400 MHz, $\text{CDCl}_3$ ) 1.62 (m, 4 H, $\text{C}(\underline{\text{H}})\text{Me}$ ), 1.16 (d, $J = 12.9$ , 9 H, $\text{C}(\underline{\text{H}})_3$ ), 1.18 (dt, $J = 15.0, 7.5$ , 6 H, $\text{CH}_2\text{C}(\underline{\text{H}})$ ), 0.46 (td, $J = 94.7, 14.3$ , 3 H, $\underline{\text{H}}\text{B}$ ).
<u><math>^{13}\text{C NMR}</math></u> :	(130 MHz, $\text{CDCl}_3$ ) 28.1 (d, $J = 33.1$ , $\underline{\text{C}}(\text{CH}_3)_3$ ), 25.7 (d, $J = 1.4$ , $\text{C}(\underline{\text{C}}\text{H}_3)_3$ ), 13.2 (d, $J = 32.7$ , $\underline{\text{C}}\text{H}_2\text{CH}_3$ ), 8.06 (d, $J = 1.9$ , $\text{CH}_2\underline{\text{C}}\text{H}_3$ )
<u><math>^{31}\text{P NMR}</math></u> :	(162 MHz, $\text{CDCl}_3$ ) 33.7 (q, $J = 62.2$ ).
<u>IR</u> :	(neat) 2974 (w), 2944 (w), 2882 (w), 2373 (w), 2339 (w), 2317 (w), 2270 (w), 2252 (w), 1466 (w), 1409 (w), 1367 (w), 1273 (w), 1254 (w), 1203 (w), 1132 (w), 1076 (w), 1064 (w), 1043 (w), 1031 (w), 1020 (w), 940 (w), 822 (w), 774 (m), 751 (w), 709 (w).
<u>MS</u> :	(EI, 70 eV) 159 ( $[\text{M}-\text{H}]^+$ , 8), 155 (10), 146 ( $[\text{M}-\text{BH}_3]^+$ , 100), 130 (3), 116 (9), 102 ( $[\text{M}-t\text{-butyl}]^+$ , 9), 90 ( $[\text{M}-\text{BH}_3, t\text{-butyl}]^+$ , 98), 74 ( $[\text{M}-t\text{-butyl, ethyl}]^+$ , 16), 69 (5), 62 ( $[\text{M}-\text{BH}_3, t\text{-butyl, ethyl}]^+$ , 41), 57 (65), 53 (2).
<u>TLC</u> :	$R_f$ 0.43 (95:5 hexane/ethyl acetate) [silica gel, aqueous $\text{KMnO}_4$ ]

Procedure for the Synthesis of *t*-Butyldimethylphosphine Borane (**16**)

Scheme 3.

To an oven dried, 50-mL, single neck, round-bottomed flask, containing a magnetic stir bar, capped with a septum that was bound with copper wire, and then evacuated and filled with argon ( $\times 3$ ) was added dry THF by syringe. The solvent was purged for 20 min with argon. The flask was cooled to 0°C using an ice bath, followed by the addition of PCl<sub>3</sub> (436  $\mu$ L, 5 mmol) by syringe. *t*-BuMgCl ([1.7], 2.94 mL, 1.0 equiv) was added drop-wise by syringe and allowed to stir at 0°C for 10 min. The reaction was warmed to room temperature by removal from the cooling bath and stirred for 40 min. The reaction was cooled to 0°C and MeMgCl ([3.0], 3.67 mL, 2.2 equiv) was added drop-wise by syringe. The reaction was allowed to stir at 0°C for 10 min, warmed to room temperature, and stirred an additional 20 min. The mixture was cooled to 0°C and BH<sub>3</sub>·THF (1.2 equiv.) was added drop-wise by syringe. The reaction was allowed to stir at 0°C for 10 min, warmed to room temperature, and stirred at least 30 min. The mixture was quenched by slow addition to a stirred solution of 1 M HCl (60 mL) at 0°C. The resulting mixture was extracted with Et<sub>2</sub>O (3  $\times$  10 mL). The combined organic extracts were washed with brine (3  $\times$  20 mL), and dried over anhydrous Na<sub>2</sub>SO<sub>4</sub>. Et<sub>2</sub>O was removed by rotary evaporation at 35 °C and 200 torr. Residual solvent was further removed under vacuum at 2 torr for 20 min.

The crude product was purified by column chromatography. The column was prepared using 40 g of silica gel suspended in hexane. The product was loaded neat and the flask was rinsed with minimal dichloromethane. An eluent consisting of a concentration gradient of 200 mL hexane, 50 mL 1% Et<sub>2</sub>O/hexane, 50 mL 2% Et<sub>2</sub>O/hexane, 100 mL 4% Et<sub>2</sub>O/hexane, and 100 mL 6% Et<sub>2</sub>O/hexane was used to elute the product. Fractions (2-3 mL each) were collected and analyzed by thin-layer chromatography. Fractions found to contain the desired product were combined and concentrated as described above to provide 411 mg (62%) of **16** as a white, crystalline solid (**Scheme 3**). The product was stable to exposure to ambient oxygen and was stored in a refrigerator for weeks with no discernible change in purity or reactivity.

Data for *t*-Butyldimethylphosphine Borane (**16**)

<u>mp</u> :	160.5–161.0 °C
<u><sup>1</sup>H NMR</u> :	(400 MHz, CDCl <sub>3</sub> ) 1.24 (d, <i>J</i> = 9.9, 6H, C( <u>H</u> ) <sub>3</sub> ) 1.17 (d, <i>J</i> = 13.5, 9H, C(C( <u>H</u> ) <sub>3</sub> ) <sub>3</sub> ) 0.5 (qd <i>J</i> = 95.3, 15.4, 3H, <u>H</u> <sub>3</sub> B)
<u><sup>13</sup>C NMR</u> :	(130 MHz, CDCl <sub>3</sub> ) 26.65 (d, <i>J</i> = 35.09, 1C, <u>C</u> (CH <sub>3</sub> ) <sub>3</sub> ) 24.77 (d, <i>J</i> = 2.45, 3C, C( <u>C</u> (H <sub>3</sub> ) <sub>3</sub> ) 7.30 (d <i>J</i> = 35.97, 2C, <u>C</u> H <sub>3</sub> )
<u><sup>31</sup>P NMR</u> :	(162 MHz, CDCl <sub>3</sub> ) 20.3 (q, <i>J</i> = 38 Hz)
<u>IR</u> :	(neat) 2965 (w), 2869 (w), 2376 (m), 2256 (w), 1474 (w), 1463 (w), 1422 (w), 1290 (w), 1137 (w), 1068 (w), 1018 (w), 942 (w), 918 (w), 851 (w), 820 (w), 756 (w).
<u>MS</u> :	(EI 70eV) 131 ([M–H], 12), 118 ([M–BH <sub>3</sub> ], 100), 88 ([M–BH <sub>3</sub> , methyl, methyl, 19), 74 ([M– <i>t</i> -butyl, H], 24), 62 (68), 57 (50).
<u>TLC</u> :	R <sub>f</sub> : 0.20 (97:3 hexanes/diethyl ether) [silica gel, aqueous KMnO <sub>4</sub> ]

## CONCLUSIONS

The *t*-butyldialkylphosphine boranes, *t*-butyldiethylphosphine borane and *t*-butyldimethylphosphine borane, were prepared by selective Grignard substitution reaction of  $\text{PCl}_3$ . The highlights of this method include the use of inexpensive  $\text{PCl}_3$  and a one-pot experimental procedure. Reaction temperature and time were found to be important for maximizing the yield and selectivity of the reaction. A stoichiometric loading of 1 equivalent of *t*-BuMgCl was found to be optimal. The optimized reaction conditions were demonstrated in the 5 mmol preparation of *t*-butyldiethylphosphine borane and *t*-butyldimethylphosphine borane in 60% and 62% yields respectively. We currently work to transform the phosphine boranes into phosphonium tetrafluoroborate salts and use them in transition metal-catalyzed reactions.

## ACKNOWLEDGEMENTS

We are grateful to Southern Utah University for a Faculty Scholarly Support Fund Grant (N.S.W.), a Walter Maxwell Gibson Research Fellowship (A.G.B. & M.B.P.), and a L.S. and Aline W. Skaggs Research Grant (M.B.P.) for the generous support of this work.

## REFERENCES

1. Auger, V., Billy (1904) Action des solutions organomagnésiennes sur les derives halogésés du phosphore de l'arsenic et de l'antimoine, *B C R* 139, 597–599.
2. Quin, L. D. (2000) *A Guide to Organophosphorus Chemistry*, 1<sup>st</sup> ed., pp 45–92, Wiley, New York.
3. Kharasch, M. S., Reinmuth, O. (1954) *Grignard Reactions of Nonmetallic Substances*, 1<sup>st</sup> ed., pp 1335–1345, Prentice-Hall, New York.
4. Simard-Mercier, J., Jiang, J. L., Ho, M. L., Flynn, A. B., Ogilvie, W. W. (2008) Multidimensional steric parameters in the analysis of asymmetric catalytic reactions, *J Org Chem* 73, 5899–5906.
5. Nishizawa, K., Ouchi, M., Sawamoto, M. (2013) Phosphine–ligand decoration toward active and robust iron catalysts in LRP, *Macromolecules* 46, 3342–3349.
6. Grim, S. (1982) Catalytic aspects of metal phosphine complexes. *Organometallics* 1, 1106–1107.
7. Brasse, C. C., Englert, U., Salzer, A., Waffenschmidt, H., Wasserscheid, P. (2000) Ionic phosphine ligands with cobaltocenium Backbone: novel ligands for the highly selective, biphasic, rhodium-catalyzed hydroformylation of 1-octene in ionic liquids, *Organometallics* 19, 3818–3823.
8. Simhai, N., Iverson, C. N., Edelbach, B. L., Jones, W. D. (2001) Formation of phenylene oligomers using platinum–phosphine complexes, *Organometallics* 20, 2759–2766.
9. Doherty, S., Knight, J. G., Ward, N. A. B., Bittner, D. M., Wills, C., McFarlane, W., Clegg, W., Harrington, R. W. (2013) Electron-rich trialkyl-type dihydro-KITPHOS monophosphines: efficient ligands for palladium-catalyzed Suzuki-Miyaura cross-coupling. Comparison with their biaryl-like KITPHOS monophosphine counterparts, *Organometallics* 32, 1773–1788.
10. McGrath, M. J., O'Brien, P. (2005) Catalytic asymmetric deprotonation using a ligand exchange approach, *J Am Chem Soc* 127, 16378–16379.
11. Rex E. Murray, Rex E. (May 26, 1987) Process for the preparation of bulky alkylarylphosphines and unsymmetrical arylalkyl phosphines, Patent US 4,668,823.
12. Romanenko, V. D., Sanchez, M., Lamande, L. (1995) *Comprehensive Organic Functional Group Transformations*, Vol. 6, (Katritzky, A. R.; Meth-Cohn, O., Rees, C. W., Gilchrist, T. L., Ed.) 1<sup>st</sup> ed., pp 689, Elsevier, New York.
13. Carbone, G., O'Brien, P., Hilmersson, G. (2010) Asymmetric deprotonation using *s*-BuLi or *i*-PrLi and chiral diamines in THF: the diamine matters, *J Am Chem Soc* 132, 15445–15450.
14. We are aware of a single report that describes the unoptimized synthesis of *t*-butyldimethylphosphine borane by selective Grignard reagent substitution reaction: Imamoto, T., Watanabe, J., Wada, Y., Masuda, H., Yamada, H., Tsuruta, H., Matsukawa, S., Yamaguchi, K. (1998) P-Chiral bis(trialkylphosphine) ligands and their use in highly enantioselective hydrogenation reactions, *J Am Chem Soc* 120, 1635–1636.
15. Hosein, A. I., Le Goff, X. F., Ricard, L., Caffyn, A. J. M. (2011) Reaction of perfluoroalkyl grignard reagents with phosphorus trihalides: a new route to perfluoroalkyl-phosphonous and -phosphonic acids, *Inorg Chem* 50, 1484–1490.
16. Staubitz, A., Robertson, A. P. M., Sloan, M. E., Manners, I. (2010) Amine- and phosphine-borane adducts: new interest in old molecules, *Chem Rev* 110, 4023–4078.
17. Taylor, N., Lloyd-Jones, G. C. (2015) Mechanism of phosphine borane deprotection with amines: the effects of phosphine, solvent and amine on rate and efficiency, *Chem Eur J* 21, 5423–5428.
18. Denmark, S. E.; Werner, N. S. (2011)  $\gamma$ -Selective cross-coupling of allylic silanolate salts with aromatic bromides using trialkylphosphonium tetrafluoroborate salts prepared directly from phosphine-borane adducts, *Org Lett* 13, 4596–4599.

19. McKinstry, L., Overberg, J. J., Soubra-Ghaoui, C., Walsh, D. S., Robins, K. A., Toto, T. T., Toto, J. L. (2000) Acid mediated phosphine-borane decomplexation: a model for characterizing short-lived intermediates with Experimental and ab initio NMR data, *J Org Chem* 65, 2261–2263.
20. Silverman, G. S. (1996) *Handbook of Grignard Reagents*, (Silverman, G.S., Ed.) 1<sup>st</sup> ed., pp 307–354, Marcel Dekker, Inc., New York.

#### ABOUT THE STUDENT AUTHORS

Auston Butterfield graduated from Southern Utah University in 2015 with a B.S. degree in chemistry with an emphasis in healthcare and a minor in biology. While at SUU, Auston was the recipient of the Walter Maxwell Gibson Research Fellowship. He aspires to treat patients as a healthcare professional.

Matthew Prater graduated Magna Cum Laude from Southern Utah University in 2015 with a B.S. degree in chemistry with an emphasis in professional chemistry. While at SUU, Matthew was the recipient of the Walter Maxwell Gibson Research Fellowship, and the L.S. and Aline W. Skaggs Research Grant. He currently pursues a graduate degree in chemistry at the University of Utah.

#### PRESS SUMMARY

Trialkylphosphines are commonly used as ligands in the transition metal-catalyzed reactions that produce a number of fine chemicals and pharmaceuticals. These reactions often require tuning of the catalyst by subtle variation in the ligand structure to maximize yield and selectivity. This work describes the discovery and optimization of an efficient synthesis of *t*-butyldimethylphosphine and *t*-butyldiethylphosphine, protected as their borane adducts, by a one-pot, selective Grignard reagent substitution reaction of inexpensive phosphorus trichloride.



## The Effect of *Umbellularia californica* Essential Oil on Blood Vessel Diameter in Frogs

Holden M. Wagstaff, Stephan R. Maman, Mary Jo Tufte, & Matthew S. Weeg\*

Department of Biology, Southern Utah University, Cedar City, UT

Students: holden.wagstaff@gmail.com, stephanmaman@gmail.com

Mentors: tufte@suu.edu, matthewweeg@suu.edu\*

### ABSTRACT

Plant essential oils contain many chemicals that are physiologically active in vertebrates. Terpenoids, which represent the largest category of these compounds, have been shown to lower blood pressure by reducing cardiac output and causing vasodilation. Most studies on the vasoactivity of terpenoids have been done on aortic rings and mesenteric artery preparations, and little is known about their effects on microvasculature. We applied *Umbellularia californica* essential oil, which contains several different terpenoids, to the cutaneous microvasculature of frogs and measured changes in blood vessel diameter. The *U. californica* oil caused a sustained, reversible vasoconstriction of these blood vessels, whereas no significant change in diameter was caused by medical grade sesame oil, which served as our control. The vasoconstriction we observed was therefore induced by compounds in the *U. californica* oil, many of which have previously been shown to cause vasodilation in arteries. Our results suggest that the vasoactive effects of terpenoids may differ across blood vessel types, and are more variable than previously thought.

### KEYWORDS

Cardiovascular; Terpenoid; Vasoactive; Arteriole; Secondary Metabolite; Vasoconstriction; Essential Oil; Microvasculature

### INTRODUCTION

Most plant species produce secondary metabolites that, among other things, provide protection against herbivory.<sup>1</sup> Although these compounds largely have negative physiological effects on herbivores,<sup>2</sup> many of them have been investigated for potential medicinal uses and exhibit promising therapeutic effects.<sup>3</sup> The most ubiquitous secondary metabolites are the terpenoids, of which over 40,000 have been identified.<sup>4</sup> Intravenous administration of terpenoids reduces blood pressure,<sup>5-8</sup> which is thought to occur because these compounds reduce heart rate<sup>5,7-10</sup> and cause vasodilation.<sup>6-11</sup> These findings have raised the possibility that terpenoids may prove effective at treating hypertension.<sup>12</sup>

Whether terpenoids universally cause vasodilation throughout the cardiovascular system is unknown. Studies on their vascular effects have been conducted almost exclusively on mammalian aortic rings and mesenteric arteries,<sup>13</sup> and little is known about how these compounds affect the microvasculature and veins. There is evidence to suggest that curcumin, a terpenoid that causes vasorelaxation in arteries,<sup>14,15</sup> can cause vasoconstriction in arterioles.<sup>16</sup> This raises the possibility that terpenoids are not exclusively vasodilators, and that their effects may vary depending on blood vessel type.

To explore the vasoactive effects of terpenoids on microvasculature, we applied *Umbellularia californica* essential oil to cutaneous blood vessels of frogs. Frog skin is particularly well suited for this purpose because it is highly vascularized with dense beds of epidermal capillaries and networks of subcutaneous arterioles and venules.<sup>17</sup> These subcutaneous vessels are readily accessible by surgical resection of the skin,<sup>18</sup> allowing microscopic changes in blood vessel diameter to be measured following treatment with vasoactive chemicals. We chose *U. californica* essential oil because it contains a cocktail of terpenoids,<sup>19</sup> several of which induce vasorelaxation in isolated aortic rings and/or mesenteric arteries.<sup>9,20-23</sup> Our objective for this study was to determine whether essential oil containing these compounds causes a similar response in the microvasculature as well.

### METHODS AND PROCEDURES

#### *Essential oil distillation*

Aerial portions of *Umbellularia californica* were collected near San Francisco, CA, and dried at room temperature. Essential oil was obtained by steam distillation<sup>24</sup> and stored in the dark at room temperature. GC-MS analysis of the oil verified the presence of the terpenoids umbellulone, eucalyptol, and terpinen-4-ol (H. Kansagra, personal communication).

### Experimental procedure

Experimental methods were approved by SUU IACUC (2013302-S). Fifteen leopard frogs (*Rana pipiens*) were obtained from Connecticut Valley Biological Supply Company. Frogs were double-pithed and covered with moist paper towels to maintain cutaneous respiration. Because anesthetics are known to alter the physiology of the amphibian cardiovascular system,<sup>25,26</sup> frogs were not anesthetized before the pithing procedure. Subcutaneous blood vessels were exposed by making incisions in the skin covering the limbs and pinning it flat on a dissection tray. The exposed blood vessels were bathed in amphibian Ringer's solution until the time of treatment. Regions that were well supplied with vessels in which blood flow could be observed were treated with 10  $\mu$ l of either *U. californica* oil or medical grade sesame oil (Sigma-Aldrich; St. Louis, MO, USA). Sesame oil was used as a control to ensure that changes in blood vessel diameter were due to the chemical components of the *U. californica* oil rather than potential hydrophobic effects of the oil. Only one site per limb was treated, with multiple limbs used on each frog.

To record changes to blood vessel diameter, digital photos were captured before and after oil application with an eyepiece-mounted digital camera (Moticam 10; Motic, Richmond, BC, Canada) and image capturing software (Motic Images Plus 2.0; Motic). One image was captured prior to oil application to give a baseline measure of blood vessel diameter. Images were then captured once per second for 300 seconds after oil application, and imported into NIH ImageJ for subsequent data analysis.

### Data collection

To measure vasoactive effects of the oil, we compared blood vessel diameter before and 60 seconds after treatment. Six blood vessels were randomly selected from each pre-treatment image. Data measurement tools in ImageJ were used to measure the diameter of these vessels in each pair of before and after treatment images. Blood vessels were selected and measurements were taken without knowledge of the type of oil that had been applied. Anatomical landmarks such as chromatophores were used to ensure that each vessel was measured at the same point along its length in each image. Pre- and post-treatment measurements were taken from 102 vessels in the experimental group and 84 vessels in the control group.

### Data analysis

All data are presented as mean +/- standard error. Paired t-tests were used to determine whether *U. californica* essential oil and/or sesame oil caused a significant change in blood vessel diameter. Unpaired t-tests were used to determine whether there was a significant difference in the percent change in diameter between *U. californica* essential oil and sesame oil.

## RESULTS

Application of *U. californica* essential oil caused several blood vessels at each site to become noticeably smaller in diameter, while other blood vessels did not appear to be affected (**Figure 1**). *U. californica* essential oil caused a significant decrease in blood vessel diameter,  $t(99) = 6.63, p = 1.75 \times 10^{-9}$ , as the average diameter before treatment was  $46.1 \mu\text{m} \pm 3.4$  and after treatment was  $32.2 \mu\text{m} \pm 2.7$  (**Figure 2**). This effect persisted for the duration of data acquisition (300 seconds post-treatment), but was reversed when the oil was washed off with Ringer's solution (data not shown). There were no visible changes in the diameter of any blood vessels following application of our sesame oil control. Data analysis confirmed that sesame oil did not have significant vasoactive effects,  $t(83) = -1.34, p = 0.18$ , as the average vessel diameter before treatment was  $49.9 \mu\text{m} \pm 4.2$  and after treatment was  $50.7 \mu\text{m} \pm 4.4$  (**Figure 2**). The percent change in blood vessel diameter caused by *U. californica* essential oil ( $-28.9\% \pm 3.1$ ) was significantly greater,  $t(140) = -8.71, p = 7.8 \times 10^{-15}$ , than that caused by our sesame oil control ( $1.1\% \pm 1.5$ ; **Figure 3**).

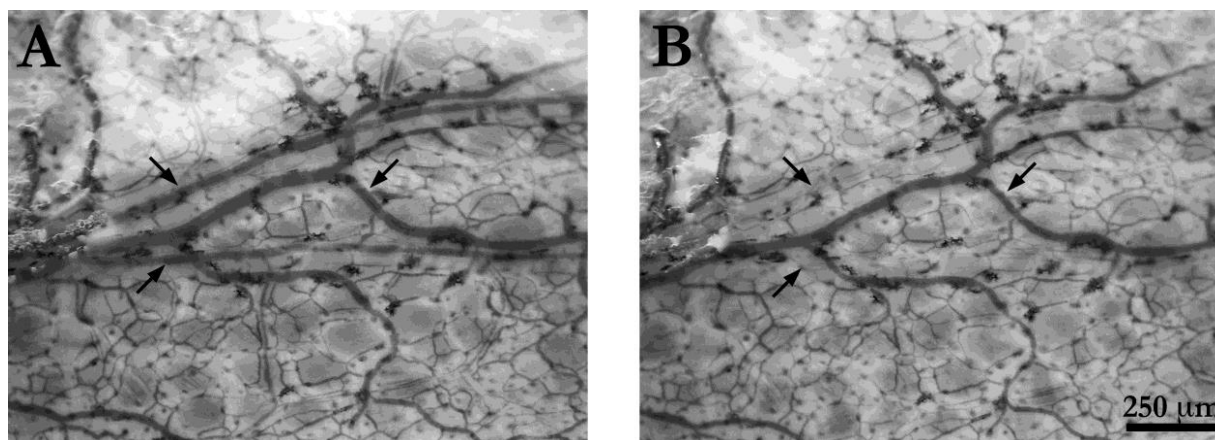


**Figure 1.** Photomicrographs of cutaneous blood vessels before (A) and 60 seconds after (B) application of 10 µl of *U. californica* essential oil. *U. californica* essential oil caused vasoconstriction in many blood vessels (arrows). Scale bar = 250 µm.

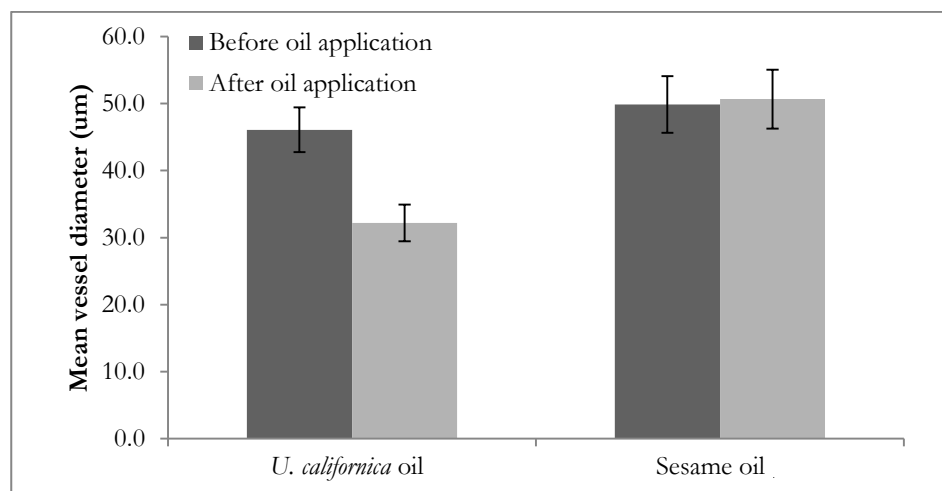


**Figure 2.** Mean cutaneous blood vessel diameter before and after application of 10 µl *U. californica* essential oil or medical grade sesame oil. *U. californica* essential oil caused a significant decrease in vessel diameter ( $p = 1.75 \times 10^{-9}$ , paired t-test), while sesame oil caused no significant change in vessel diameter ( $p = 0.18$ ). Error bars represent standard error.

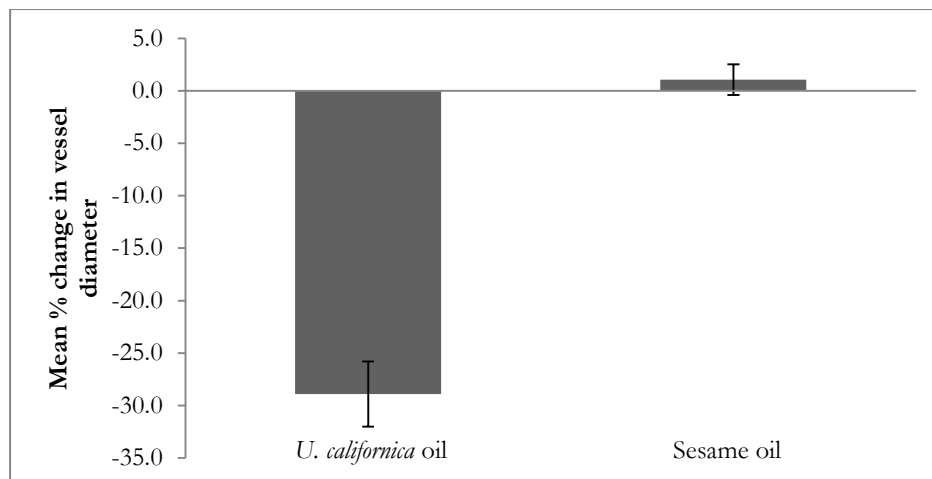


**Figure 3.** Mean percent change in cutaneous blood vessel diameter caused by application of 10  $\mu$ l *U. californica* essential oil or medical grade sesame oil. *U. californica* essential oil caused a significantly greater change in blood vessel diameter than sesame oil ( $p = 4.2 \times 10^{-14}$ , unpaired t-test). Error bars represent standard error.

## DISCUSSION

Our results indicate that *U. californica* essential oil causes significant vasoconstriction when applied directly to cutaneous blood vessels in frogs. Because our control did not affect blood vessel diameter, we conclude that the vasoconstriction we observed was due to the vasoactive properties of one or more components of the *U. californica* oil rather than its hydrophobic nature. The return of the blood vessels to their original diameter after washing with Ringer's solution indicates that the change in diameter was physiological, and not due to any unknown cytotoxic effects of the oil.

We observed considerable variation in the degree of vasoconstriction caused by *U. californica* oil, with some vessels constricting almost completely and some not at all. It is possible that cutting and pinning the skin compromised the integrity of some vessels and not others, leading to the differences we observed. However, we only applied oil to regions in which blood was flowing in all of the vessels, which suggests that they were all physiologically viable. More likely, these results arose from the different types of blood vessels present in frog skin and the specific vasoactive properties of each vessel type. The subcutaneous layer of amphibian skin contains arterioles that supply epidermal capillary beds and venules that drain them. Blood flow through the capillaries is controlled primarily by changes in the diameter of arterioles,<sup>27</sup> which have a stronger vasoactive response than venules.<sup>28</sup> We therefore hypothesize that the vessels showing the greatest vasoconstriction were arterioles and those showing little or no response were venules.

The vasoconstriction that we observed is contrary to the vasodilatory effects of terpenoids on aortic rings and mesenteric arteries.<sup>6-11</sup> Our results are also inconsistent with the hypotensive effects that occur when terpenoids are administered systemically,<sup>5-8</sup> as a drop in blood pressure suggests arteriolar vasodilation rather than vasoconstriction. These differences are surprising, given that our oil was comprised primarily of the terpenoids umbellulone, 1,8-cineole (eucalyptol), and terpinen-4-ol, which have all been shown to cause arterial vasodilation.<sup>12,13</sup> Umbellulone causes an increase in meningeal blood flow, which is interpreted as vasodilation, when administered intravenously or intranasally.<sup>29</sup> This occurs due to an interaction between umbellulone and trigeminal neurons rather than vascular smooth muscle, which may explain the difference in vascular response. 1,8-cineole (eucalyptol) causes vasodilation when applied directly to aortic rings or mesenteric arteries,<sup>9,20</sup> and intravenous injections of terpinen-4-ol cause a decrease in blood pressure that is thought to arise from vasodilation.<sup>30</sup> Thus, our results are contrary to all previously published work on the vasoactivity of compounds contained within *U. californica* oil.

There are a number of possible explanations for these differences. Previous studies on the vasoactive effects of terpenoids have focused on mammals, so our results may reflect species-specific effects. It would be interesting to apply *U. californica* oil to a mammalian preparation such as the rabbit cheek pouch to investigate this hypothesis. Many vasoactive compounds interact synergistically,<sup>31-33</sup> and it is possible that vasoconstriction arises from the combined activity of the terpenoids within *U. californica* essential oil. This idea could be explored by applying umbellulone, eucalyptol, and terpinen-4-ol individually and in different combinations to our frog skin preparation. We are most intrigued by the possibility that our results reflect differences in how arteries and arterioles respond to terpenoids. This hypothesis is supported by studies on the terpenoid curcumin, which causes

vasodilation when applied to isolated aortic rings,<sup>14</sup> but vasoconstriction when applied at high concentrations to cutaneous arterioles.<sup>16</sup> The physiological cause of this difference is unknown, but may be due to differences in the receptors found on arterial and arteriolar smooth muscle. This possibility warrants further investigation, including applying *U. californica* oil to arteries or applying known vasodilatory terpenoids to microvasculature.

## CONCLUSIONS

Previous research has supported the hypothesis that terpenoids act exclusively as vasodilators.<sup>12,13</sup> However, the majority of studies have been conducted on arteries, with little attention paid to arterioles. Our results lend support to the alternative hypothesis that the vasoactive effects of terpenoids are variable, and that vessels of the microvasculature respond differently to these compounds than arteries do. Future research should focus on the microvasculature to evaluate these competing hypotheses, and determine the physiological mechanisms behind the variability in terpenoid effects.

## ACKNOWLEDGEMENTS

The authors thank T. Hildebrandt for bringing *U. californica* to our attention and H. Kansagra for GC-MS analysis. D. Tufte and J. Grant provided help with statistics and feedback on an earlier version of this manuscript. We also thank two anonymous reviewers for their thoughtful feedback. Funding was generously provided by SUU UGRASP, an L.S. & Aline W. Skaggs Research Fellowship, and a Walter Maxwell Gibson Research Fellowship.

## REFERENCES

1. Fürstenberg-Hägg, J., Zagrobelny, M., and Bak, S. (2013) Plant defense against insect herbivores, *Int J Mol Sci* 14, 10242–10297.
2. Iason, G. (2005) The role of plant secondary metabolites in mammalian herbivory: ecological perspectives, *Proc Nutr Soc* 64, 123–131.
3. Edris, A.E. (2007) Pharmaceutical and therapeutic potentials of essential oils and their individual volatile constituents: a review, *Phytother Res* 21, 308–323.
4. Aharoni, A., Jongsma, M.A., and Bouwmeester, H.J. (2005) Volatile science? Metabolic engineering of terpenoids in plants, *Trends Plant Sci* 10, 594–602.
5. Aydin, Y., Kutlay, Ö., Ari, S., Duman, S., Uzuner, K., and Aydin, S. (2007) Hypotensive effects of carvacrol on the blood pressure of normotensive rats, *Planta Med* 73, 1365–1371.
6. Bastos, J.F., Moreira, Í.J., Ribeiro, T.P., Medeiros, I.A., Antonioli, A.R., De Sousa, D.P., and Santos, M.R. (2010) Hypotensive and vasorelaxant effects of citronellol, a monoterpene alcohol, in rats, *Basic Clin Pharmacol Toxicol* 106, 331–337.
7. Guedes, D.N., Silva, D.F., Barbosa-Filho, J.M., and Medeiros, I.A. (2002) Muscarinic agonist properties involved in the hypotensive and vasorelaxant responses of rotundifolone in rats, *Planta Med* 68, 700–704.
8. Interaminense, L.F.L., Jucá, D.M., Magalhães, P.J.C., Leal-Cardoso, J.H., Duarte, G.P., and Lahlou, S. (2007) Pharmacological evidence of calcium-channel blockade by essential oil of *Ocimum gratissimum* and its main constituent, eugenol, in isolated aortic rings from DOCA-salt hypertensive rats, *Fundam Clin Pharmacol* 21, 497–506.
9. Lahlou, S., Figueiredo, A.F., Magalhães, P.J.C., and Leal-Cardoso, J.H. (2002) Cardiovascular effects of 1, 8-cineole, a terpenoid oxide present in many plant essential oils, in normotensive rats, *Can J Physiol Pharmacol* 80, 1125–1131.
10. Ribeiro, T.P., Porto, D.L., Menezes, C.P., Antunes, A.A., Silva, D.F., De Sousa, D.P., Nakao, L.S., Braga, V.A., and Medeiros, I.A. (2010) Unravelling the cardiovascular effects induced by  $\alpha$ -terpineol: a role for the nitric oxide–cGMP pathway, *Clin Exp Pharmacol Physiol* 37, 811–816.
11. Criddle, D.N., Madeira, S.V.F., and Moura, R.S. (2003) Endothelium-dependent and-independent vasodilator effects of eugenol in the rat mesenteric vascular bed, *J Pharm Pharmacol* 55, 359–365.
12. Santos, M.R., Moreira, F.V., Fraga, B.P., De Souza, D.P., Bonjardim, L.R., and Quintans-Junior, L.J. (2011) Cardiovascular effects of monoterpenes: a review, *Rev Bras Farmacogn* 21, 764–771.
13. Luna-Vázquez, F.J., Ibarra-Alvarado, C., Rojas-Molina, A., Rojas-Molina, I., and Zavala-Sánchez, M.Á. (2013) Vasodilator compounds derived from plants and their mechanisms of action, *Molecules* 18, 5814–5857.
14. Sasaki, Y., Goto, H., Tohda, C., Hatanaka, F., Shibahara, N., Shimada, Y., Terasawa, K., and Komatsu, K. (2003) Effects of curcuma drugs on vasomotion in isolated rat aorta, *Biol Pharm Bull* 26, 1135–1143.
15. Xu, P.-H., Long, Y., Dai, F., and Liu, Z.-L. (2007) The relaxant effect of curcumin on porcine coronary arterial ring segments, *Vascul Pharmacol* 47, 25–30.
16. Dewar, A.M., Clark, R.A., Singer, A.J., and Frame, M.D. (2011) Curcumin mediates both dilation and constriction of peripheral arterioles via adrenergic receptors, *J Invest Dermatol* 131, 1754–1760.
17. Czopek, J. (1965) Quantitative studies on the morphology of respiratory surfaces in amphibians, *Cells Tissues Organs* 62, 296–323.
18. Pinder, A., Clemens, D., and Feder, M. (1990) An isolated perfused frog skin preparation for the study of gas exchange, in *Oxygen Transport to Tissue XII* (Piiper, J., Goldstick, T., and Meyer, M., Ed.) 719–724, Springer, New York.

19. Tabanca, N., Avonto, C., Wang, M., Parcher, J.F., Ali, A., Demirci, B., Raman, V., and Khan, I.A. (2013) Comparative investigation of *Umbellularia californica* and *Laurus nobilis* leaf essential oils and identification of constituents active against *Aedes aegypti*, *J Agric Food Chem* 61, 12283–12291.
20. Pinto, N.V., Assreuy, A.M.S., Coelho-de-Souza, A.N., Ceccatto, V.M., Magalhães, P.J.C., Lahlou, S., and Leal-Cardoso, J.H. (2009) Endothelium-dependent vasorelaxant effects of the essential oil from aerial parts of *Alpinia zerumbet* and its main constituent 1, 8-cineole in rats, *Phytomedicine* 16, 1151–1155.
21. Lahlou, S., Interaminense, L.F.L., Magalhães, P.J.C., Leal-Cardoso, J.H., and Duarte, G.P. (2004) Cardiovascular effects of eugenol, a phenolic compound present in many plant essential oils, in normotensive rats, *J Cardiovasc Pharmacol* 43, 250–257.
22. Peixoto-Neves, D., Silva-Alves, K.S., Gomes, M.D.M., Lima, F.C., Lahlou, S., Magalhães, P.J.C., Ceccatto, V.M., Coelho-de-Souza, A.N., and Leal-Cardoso, J.H. (2010) Vasorelaxant effects of the monoterpene phenol isomers, carvacrol and thymol, on rat isolated aorta, *Fundam Clin Pharmacol* 24, 341–350.
23. Magalhães, P.J.C., Lahlou, S., Jucá, D.M., Coelho-de-Souza, L.N., Frota, D., Tibúrcio, P.T., Da Costa, A.M.G., and Leal-Cardoso, J.H. (2008) Vasorelaxation induced by the essential oil of *Croton nepetaefolius* and its constituents in rat aorta are partially mediated by the endothelium, *Fundam Clin Pharmacol* 22, 169–177.
24. Starman, D.A., and Nijhuis, H.H. (1996) Extraction of secondary metabolites from plant material: a review, *Trends Food Sci Technol* 7, 191–197.
25. Cakir, Y., and Strauch, S.M. (2005) Tricaine (MS-222) is a safe anesthetic compound compared to benzocaine and pentobarbital to induce anesthesia in leopard frogs (*Rana pipiens*), *Pharmacol Rep* 57, 467–474.
26. Goulet, F., Hélie, P., and Vachon, P. (2010) Eugenol anesthesia in African clawed frogs (*Xenopus laevis*) of different body weights, *J Am Assoc Lab Anim Sci* 49, 460–463.
27. Segal, S.S. (2005) Regulation of blood flow in the microcirculation, *Microcirculation* 12, 33–45.
28. Malvin, G.M., and Walker, B.R. (2001) Sites and ionic mechanisms of hypoxic vasoconstriction in frog skin, *Am J Physiol-Regul Integr Comp Physiol* 280, R1308–R1314.
29. Nassini, R., Materazzi, S., Vriens, J., Prenen, J., Benemei, S., Siena, G.D., la Marca, G., André, E., Preti, D., Avonto, C., Sadofsky, L., Marzo, V.D., Petrocellis, L.D., Dussor, G., Porreca, F., Tagliabue, S., Scafati, O., Appendino, G., Nilius, B., and Geppetti, P. (2011) The “headache tree” via umbellulone and TRPA1 activates the trigeminovascular system, *Brain* 135, 376–390.
30. Lahlou, S., Galindo, C.A., Leal-Cardoso, J.H., Fonteles, M.C., and Duarte, G.P. (2002) Cardiovascular effects of the essential oil of *Alpinia zerumbet* leaves and its main constituent, Terpinen-4-ol, in rats: role of the autonomic nervous system, *Planta Med* 68, 1097–1102.
31. Gardiner, S.M., Compton, A.M., Bennett, T., Kemp, P.A., and Ney, U. (1990) Synergistic internal carotid vasodilator effects of human  $\alpha$ -calcitonin gene-related peptide and nimodipine in conscious rats, *Br J Pharmacol* 99, 830–834.
32. Li, J., and Meng, Z. (2009) The role of sulfur dioxide as an endogenous gaseous vasoactive factor in synergy with nitric oxide, *Nitric Oxide* 20, 166–174.
33. Oliveira, M.A., Fortes, Z.B., Santos, R.A., Kosla, M.C., and De Carvalho, M.H.C. (1999) Synergistic effect of angiotensin-(1–7) on bradykinin arteriolar dilation in vivo, *Peptides* 20, 1195–1201.

#### ABOUT THE STUDENT AUTHORS

Holden Wagstaff graduated with a Bachelor of Science in Biology from Southern Utah University in 2015. He is currently attending the University of Rochester School of Medicine and Dentistry seeking an MD degree.

Stephan R. Maman graduated with a Bachelor of Science in Biology from Southern Utah University in 2015. He is currently pursuing an MD degree at Penn State College of Medicine and will graduate in May 2019.

#### PRESS SUMMARY

Essential oils contain chemicals that can alter the physiology of animals. Many of these chemicals affect the cardiovascular system by increasing the diameter of large arteries. We applied *Umbellularia californica* essential oil to smaller arterioles and observed a decrease in diameter, opposite to what was expected. Our results suggest that arterioles respond differently to the chemicals in essential oils, and that the effect of essential oils on the cardiovascular system is more variable than previously described.

# The Wellbeing of Young Adults as a Function of Parental Status in Rural Tanzania

H. Callie Silber

Department of Human Development, College of Human Ecology, Cornell University, Ithaca, NY

Student: [bc58@cornell.edu](mailto:bc58@cornell.edu)\*

Mentors: [jhw43@cornell.edu](mailto:jhw43@cornell.edu)\*, [cb34@cornell.edu](mailto:cb34@cornell.edu), [jbeckham@cjee.org](mailto:jbeckham@cjee.org)

## ABSTRACT

The East-African nation of Tanzania has one of the highest HIV/AIDS rates in the entire world, and thus, an alarmingly high number of orphaned children. The present study sought to determine if being an orphan during childhood, either single or double, is related to one's psychological wellbeing in young adulthood. Orphan status and psychological wellbeing information was gathered via surveys containing background information and standardized wellbeing scales. The oral survey was administered in person in Kiswahili, the national language of Tanzania. Sixty-three young adults, ages 18–25, in a small rural village community participated in the study. The results of the study found no significant association between orphan status in childhood and psychological wellbeing in young adulthood, leading to a discussion on how parental loss may be experienced in small, African, rural villages, under the framework of resilience. Conclusions were all speculative and further research is thus recommended.

## KEY WORDS

Psychological; Wellbeing; Orphan; Parental Loss; HIV/AIDS; Tanzania; Sub-Saharan Africa

## BACKGROUND INFORMATION

Tanzania is a nation of 49.25 million people,<sup>1</sup> located in Eastern African, just south of the equator. Unlike many other African countries, the national language, Kiswahili, is still widely spoken and most Tanzanians identify as “Tanzanian” first and foremost. This national unity has led to a history of peace, even with the 120 different ethnic groups that exist<sup>2</sup> and the varying religious beliefs, including Christianity (30%), Muslim (35%) and indigenous beliefs (35%).<sup>2</sup> The basic family structure in Tanzania is extended, especially in the urban areas. The pressures of development in the urban areas have led to an increasing regularity of nuclear family units.<sup>3</sup>

Compared to the United States' median age of 36.8 years,<sup>1</sup> the median age in Tanzania is 17.5 years.<sup>1</sup> The vast majority (44.34%) of Tanzania's population is between the ages of 0 and 14. The percent of the population between 15 and 24 is 19.59% and only 2.97% of the population is 65 years or older.<sup>1</sup> Much of this skewedness can be attributed to the poverty and disease that has stricken Tanzania since its inception. In 2011, it was estimated that 67.9% of the population was living below the poverty line and the CIA's World Factbook categorizes the degree of risk of infectious disease as very high.<sup>1</sup>

In general, Sub-Saharan Africa has the highest HIV/AIDS rates across the entire globe. In Tanzania, specifically, it has been estimated that the prevalence of adults living with HIV/AIDS is 5.1%. In the Iringa region, the current region of interest, the percentage of 15-49 year olds who are HIV positive surpasses the national average at 9.1%.<sup>3, 4</sup> Beyond the HIV/AIDS epidemic, data from the World Health Organization has indicated that maternal/perinatal conditions and TB/respiratory infections are the second and third leading causes of disability-adjusted life years lost in Tanzania (after HIV/AIDS).<sup>5</sup> For developed nations, many of these deaths would be preventable. But, due to the rampant poverty and poor education in Tanzania, many Tanzanians are suffering from such life-threatening diseases.

The devastating rates of HIV/AIDS and other diseases, especially in some rural regions, have led to a disconcerting number of orphans. For the purpose of this study, an orphan is defined as an individual who has lost one or both biological parents before the age of 15. It is estimated that in Tanzania as a whole, 12% of all children are orphans.<sup>6</sup> But, in the location of this research, the Mufindi region of Iringa, a HIV/AIDS prevalence of 14.8% has contributed

to an orphanhood rate of nearly 16%.<sup>7</sup> Though it is not possible to know from this data whether orphanhood rates are due to HIV/AIDS, orphanhood has been most common in areas with high current or past prevalence of HIV/AIDS.

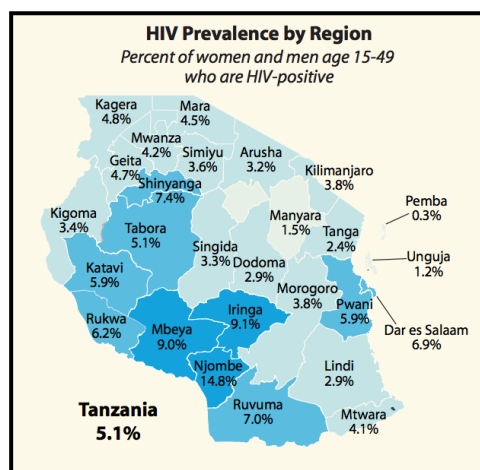


Figure 1. Map of Tanzania’s HIV prevalence rates by region.<sup>4</sup>

It has been speculated that Mufindi has especially high rates due to a lack of access to HIV/AIDS testing, treatment and education, as a result of its geographic isolation.<sup>8</sup> Additionally, due to its natural resources, such as timber and tea, Mufindi is a trade center for many people from larger cities.<sup>9</sup> This constant flow of people in and out of Mufindi allows for the spread of HIV/AIDS from the cities into rural Mufindi.

Since the HIV/AIDS endemic began in 1983, the disease has continued to spread and rates have continually increased. The increasing number of orphans in Tanzania and Sub-Saharan Africa as a whole has led to a heightened interest in the psychological wellbeing of orphans. While there is not one universally agreed upon definition for “psychological wellbeing,” the current study will be working under an operational definition developed from previous literature in the field<sup>10</sup> and an understanding of cultural values in Tanzania.<sup>11</sup> Psychological wellbeing is defined in this study as having a sense of agency over, and contentment with, one’s thoughts, emotions and behaviors.

**REVIEW OF THE LITERATURE**

The continuous rise in the population of orphan children has resulted in a body of literature regarding orphan wellbeing. Much of the previous literature has focused on the mental health, social functioning and academic achievement among orphans, compared to non-orphans. In the current study, the psychological wellbeing of young adults is being examined based on their childhood orphan status. Based on the findings of previous orphan studies and studies related to the cognitive neuroscience related to the enduring effects of parental loss, the current study hypothesizes that one’s psychological wellbeing in young adulthood is related to parental loss as a child.

In Sub-Saharan African, there is growing evidence that orphans, in general, suffer increased psychological distress. Paul Narh Doku, a psychologist at the University of Ghana, explains that, “HIV/AIDS will not only restrict psychological development but also contribute to psychological distress like depression, anxiety and low self-esteem, due to the shock that results from the parents’ death.”<sup>12</sup> Many field studies have supported this idea of orphan vulnerability, by comparing orphans to their non-orphan counterparts.

In one of the earlier studies conducted in 2002 in the capital of Tanzania, Dar Es Salaam, researchers used multiple questionnaires to examine the psychological conditions of orphans, compared to non-orphans of similar ages and geographic locations. An internalizing problem scale was used to assess pessimism, sense of failure, anxiety and other mental health problem areas. Orphans had significantly higher scores on the internalizing problem scale than non-

orphans, with high scores indicating more internalizing problems. Additionally, nearly triple the amount of orphans admitted that they had contemplated suicide within the past year, compared to non-orphan counterparts.<sup>13</sup>

In a similar Ugandan study, researchers used the Beck Youth Inventories of Emotional and Social Impairment to compare 123 children who had one or both parent pass away from HIV/AIDS and 110 children of similar age and gender who were living in households with two living parents. Their results showed that orphans were at greater risk for higher levels of anxiety, depression and anger. Additionally, orphans' responses to questions indicated potential depressive disorders significantly more frequently than non-orphans.<sup>14</sup> Furthermore, a study in eastern Zimbabwe, yielded similar findings with a sample of 1469 children ages 0-18, with equal numbers of paternal, maternal and double orphans and non-orphans, compared on levels of psychological distress. In this 2008 study, data revealed that boys and girls experiencing all forms of orphanhood (paternal, maternal, double) had higher levels of psychological distress than their non-orphaned counterparts.<sup>15</sup>

In response to these findings being replicated around the globe, Western cognitive neuroscientists attempted to uncover potential neural explanations for psychological ramifications of parental loss. Though often times it is not advisable to use Western research in a cross-cultural context, the following studies are concerned with altered brain structures that all human beings share. Most cognitive neuroscientists agree that experiences, especially traumatic ones, during childhood and adolescence have a profound impact on adult functioning, due to actual neurological changes and restructuring.<sup>16,17</sup> One study published in the journal of Biological Psychiatry found alterations in the hypothalamic-pituitary-adrenal (HPA) axis among adults who suffered from childhood parental loss. Changes to the HPA axis function can predispose adults to the development of psychiatric disorders, specifically major depression. These findings are consistent with the hypothesis that early parental loss induces enduring changes in one's neurological functions.<sup>18</sup> Additionally, researchers at the University of Pittsburgh found that a parent's death more than quadruples the risk for depression in children, adolescents, and young adults, due to neural differences compared to a control group.<sup>19</sup>

There is overwhelming evidence that orphans experience more psychological disturbances than non-orphans during childhood, but do these variations in psychological wellbeing persist into young adulthood or are there protective factors working to mitigate these discrepancies? In the current study, the question under consideration is whether or not being orphaned (maternal, paternal or double) during childhood (between the ages 0 and 15) is associated with greater levels of distress and lower levels of psychological wellbeing in young adulthood. If the results are consistent with previous Sub-Saharan African and Western findings, orphans will earn lower scores on wellbeing scales compared to non-orphans, even in young adulthood (ages 18–25).

## DATA AND METHODOLOGY

### *Research setting*

The data was collected in Igoda, a village within the Mufindi district of Tanzania over a two-week period in April 2015 (refer to the image below for a map of Mufindi's location). The village of Igoda has been blessed with a plethora of natural resources, including lumber and fertile soil to farm tea, beans, and other crops. Unfortunately though, Igoda has one of the highest HIV/AIDS rates in the entire world, with an estimated 35% of adults infected. In the village of Igoda, there is a non-governmental organization, Foxes' NGO, that helps to care for the rising number of orphans. At any given time, the NGO has the capacity to care for 50–60 children, leaving other orphans to live with family or community members in their home village.

### *Participants*

In the present study, there were 63 participants. Participants were recruited through random sampling and purposeful location sampling. In three villages, Iyayi, Mwaya and Fyogo, randomization was employed approaching only every other house on alternating sides of the street. At Luhunga Secondary School, purposeful location sampling was used as all eligible students on the campus were asked to participate.

After having the participant listen to an oral consent script, read in Kiswahili, and provide oral consent, signatures from the primary researcher and research assistant verified participant consent. Consenting participants were then able

to proceed with the oral survey. With the exception of the participants at Luhunga Secondary School, all surveys took place within the participant’s homes. To ensure participant confidentiality and open, candid responses, we asked all other family members, with the exception of small children, to not be present as the survey was taking place.

Out of the 63 responses, 29 were orphans (46.8%), 33 were non-orphans (53.2%), and 1 respondent did not complete the survey. The participants were all between the ages of 18 and 25, with a mean age of 20.48 years old. Refer to Chart 1 for the full break down of ages. Out of the 63 participants whose data was analyzed, 34 people identified as female, 23 as male, and five participants did not respond.

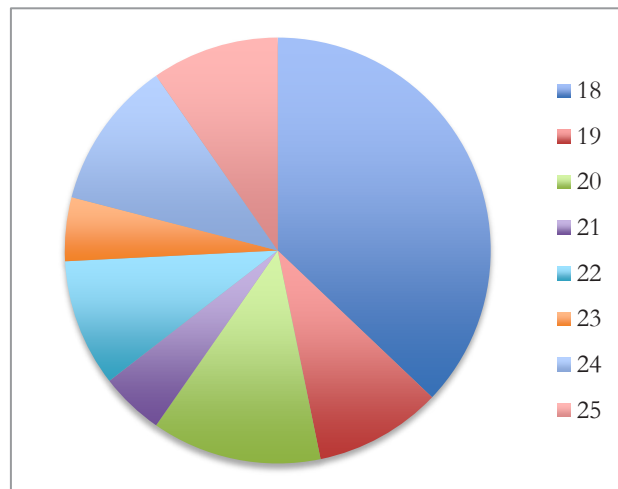


Chart 1. Age of participants.

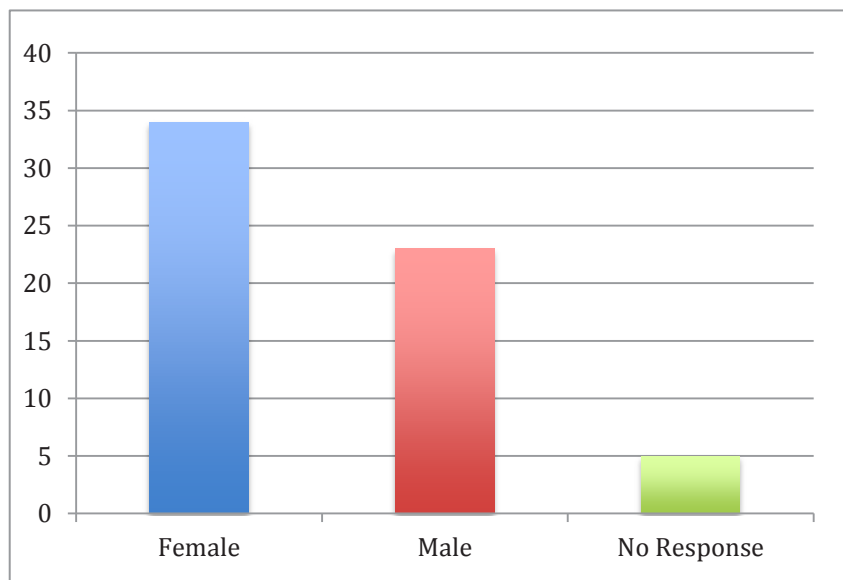


Chart 2. Sex of participants.

Information regarding the parental status of the participant can be found in **Table 1**. Paternal orphans refer to those individuals who lost their father between the ages of 0 and 15 (before or during primary school). Maternal orphans refer to those individuals who lost their mother between the ages of 0 and 15 (before or during primary school). Double orphans refer to those individuals who lost their mother and father between the ages of 0 and 15 (before or during primary school). Compared to the national average predictions in 2010 of the Iringa region, 6% paternal, 4% maternal, 1.6% double, the findings in the present study are alarming.<sup>20</sup> The current results are from the total sample of 63 participants, in order to show the distribution of non-orphans to orphans among the random sample.

This data shows an orphan rate tripling the Iringa region average in nearly every category. As previously stated, the Mufindi region has a higher rate of orphans, compared to the Iringa region as a whole. However, compared to even statistics from Mufindi (16% orphan rate),<sup>7</sup> the rates in our study are alarmingly high. Mufindi is comprised of many different villages, but data collection only took place in Iyayi, Mwaya and Fyogo. In 2007, an NGO to address the orphan problem in Mufindi was built closest to the villages where data was collected.<sup>15</sup> It can be posited that this NGO was built in proximity to the most vulnerable villages. Therefore, the villages that data was collected from might be the most vulnerable among the Mufindi villages.

Orphan Status	# Of Participants	Percent of Total	2010 National Estimates of Iringa region <sup>20</sup>
Paternal	12	19.05%	6%
Maternal	10	15.87%	4%
Double	7	11.11%	1.6%
Total orphans	29	46.8%	11.6%

Table 1. Orphanhood status of participants.

*Materials*

The original survey was written and compiled in English, then translated into Kiswahili, the national language of Tanzania. After the initial translation, my trained research assistant, born and raised in Mufindi, back translated the survey and made suggestions based on cultural appropriateness that were used to finalize the survey. The survey included 39 multiple-choice questions. The questions consisted of a brief demographics questionnaire (gender and age), two standardized well-being scales: General Well Being Schedule (GWBS) and Mental Health Continuum-Short Form (MHC-SF), and a short set of questions related to childhood/parental status. The final set of childhood/parental status questions contained questions pertaining to living situation during childhood (i.e. lived with mother and father, lived in orphanage), the current status of both mother and father, and the approximate age of passing of their parent(s), if appropriate.

The MHC-SF has been used in hundreds of different studies and has been employed on the African continent, in a rural South African study. The short form of the MHC has shown outstanding internal consistency (>.80) and discriminant validity in adolescents and adults in the United States, the Netherlands, and South Africa.<sup>21-23</sup> Specifically, in a South African study, the MHC-SF was translated into Setswana, an African language, to test for reliability and validity. The internal reliability of the MHC-SF was .74 and it correlated most strongly with measures of subjective wellbeing, which is most appropriate for the current study’s needs.<sup>22</sup> Furthermore, the GWBS, a scale that has been translated and culturally adopted in over 35 languages, was also translated into Setswana and used in a validation study in rural and urban South Africa. The scale yielded a high, reliable Cronbach alpha of .89 and showed evidence of construct validity.<sup>24</sup>

The questions from the GWBS pertained to the participants’ moods/emotions (i.e. exhausted, anxious, pleased, in control, discouraged) and how often they were experiencing them, over the past month, ranging from all the time to none of the time. Similarly, the MHC-SF asked questions in the format “during the past month, how often did you feel...?” However, the MHC-SF placed a greater emphasis on the social part of psychological wellbeing, asking more questions about belonging to a community and views of society.

*Procedure*

The Kiswahili surveys were administered orally, and responses were recorded by hand, using number and letter codes. Each participant’s responses were recorded on separate pieces of paper to ensure the confidentiality of all participants. Participants were given unlimited time to complete the survey. However, the majority of our participants completed the survey in 25–30 minutes.

### *Ethical Considerations*

Before the research began, the University of Iringa provided a signed and stamped document from the Deputy Vice Chancellor for Resources Management, allowing the research team to associate themselves with the university throughout the field work. Additionally, upon arrival in Mufindi, verbal consent was obtained from the village leader of each of the four villages that research was conducted in. Furthermore, the researcher sought further ethical approval from the Cornell University IRB, ultimately obtaining an exemption to review. An exemption to review is granted to researchers whose research involves surveys that are recorded in a way in which individuals (adults above the age of 18) cannot be identified. This exemption allowed the researcher to proceed with their research, upholding the ethical standards of the IRB but without review and oversight by the IRB. The Cornell University IRB exemption to review was received prior to all data collection.

Additionally, informed oral consent was obtained from each participant, recorded only by the researcher and research assistant to ensure no identifying information (signatures) was recorded. Due to the nature of the questions, psychological counseling services were made available to each participant. The available services included a Tanzanian licensed therapist and transportation to and from, paid for by the researcher's study abroad program (CIEE Iringa). The participants were notified of this offer at the beginning and end of the survey. None of the participants expressed a desire to obtain the offered psychological services. To show appreciation for their participation, each young adult was given 1,000 Tanzania shillings (\$0.60). This amount was calculated based on the fact that the minimum wage for a day of employment in Tanzania is 6,000 shillings and the survey took roughly one half hour to complete.

### **RESULTS**

In the initial hypothesis, it was predicted that the experimental group, those who had been orphaned before the age of 15, would have lower GWBS and MHC scores overall than the control group of non-orphans. Statistical analyses were carried out using Data Desk 7.0.1 Student (Ithaca, NY 2014) and R/R Studio (Boston, MA 2015).

First, analyses were performed on overall MHC-SF scores, after grouping the participants by their orphan status. The highest score one can receive on the MHC-SF is a 70, indicating exemplary wellbeing in three categories (emotional, social and psychological wellbeing). For the sample of orphans ( $n=29$ ), the overall MHC scores had a mean of 47.79 ( $SD=9.04$ ) and a range of 29. For the sample of non-orphans ( $n=33$ ), the overall MHC scores had a mean of 48.515 ( $SD=9.16$ ) and a range of 30. A Welch's two-sample t-test was then used to determine whether the mean scores of the experimental group (orphans) and control group (non-orphans) were significantly different, as the original hypothesis predicted. This test was chosen specifically as it is not sensitive to the different sample sizes between the two groups. This test yielded a statistically non-significant p-value of 0.62, thus we failed to reject the null hypothesis at  $\alpha = .05$  ( $t(56.93) = .50$ ). A post-hoc analysis indicated a very small effect size ( $\eta^2 = .004$ ).

The highest possible score for the GWBS scale is 110, indicating the highest level of overall wellbeing. From the sample of orphans ( $n=29$ ), the overall GWBS scores had a mean of 66.21 ( $SD=11.47$ ) and a range of 50. For the non-orphan sample ( $n=33$ ), the overall GWBS scores had a mean of 71.576 ( $SD=17.439$ ) and a range of 69. For the GWBS scores, another Welch's two-sample t-test was conducted, yielding a p-value of .15, thus we failed to reject the null hypothesis at  $\alpha = .05$  ( $t(55.81) = 1.45$ ). A post-hoc analysis indicated a relatively small effect size ( $\eta^2 = .036$ ).

### **DISCUSSION**

This study's results conclude that there is no statistically significant association between orphan status in childhood and psychological wellbeing in young adulthood. In both of the Welch's two-sample t-tests, for MHC scores and GWBS scores, the p-values were too large (greater than .05) to be statistically significant, and therefore no associations could be justified. The initial hypothesis predicted that there would be an association between childhood orphan status and psychological wellbeing scores: children who had suffered parental loss would have lower scores on wellbeing scales in young adulthood.

Though not in line with the original hypothesis, the lack of an association between orphan status and psychological wellbeing in young adulthood is an intriguing finding in itself. The data is suggestive of the idea that there may be something serving as a protective factor that allows young adults who were orphaned to be comparable, in terms of

psychological wellbeing, to their non-orphan counterparts. Among psychologists, it is widely accepted that losing a parent, or both parents, increases the likelihood for that individual to develop psychopathological symptoms in the future.<sup>18, 19</sup>

Despite these findings, however, a smaller body of related research has explored another theoretical framework contrasting vulnerability: resilience and protective factors. Some of this research has applied the framework to orphans and the HIV/AIDS epidemic. One study, in Arusha, Tanzania found that “children and young people’s relationships with siblings and other surviving members of the household are an important source of emotional support, which may represent a protective factor in mitigating individuals’ vulnerability.”<sup>25</sup> This study was conducted in a rural setting, similar to Mufindi. Within the villages of Mufindi, family lines are blurred and the unity among all community members is unique to this part of the world. It is very common for adults to care for all of the children in their village as if they were their own. This extended support system, along with attachments formed outside of one’s biological family could be serving as protective factors.

In support of this insinuation, according to the survey results, during the past month, 41 out of 58 (70.7%) participants felt almost every day or every day that they belonged in a community, like a social group or neighborhood and 48 out of 58 participants (82.8%) felt almost every day or every day that they had warm and trusting relationships with others. There is much value in having solid relationships and feeling supported, as many studies have found strong associations between having supportive social relationships and adolescent resilience following a loss.<sup>26, 27</sup> Further research is necessary to validate these speculations from the current study.

## LIMITATIONS

The present study had three main limitations. First, this study employed the General Well Being Schedule and the Mental Health Continuum-Short Form for psychological measurements. Though the researchers chose these scales thoughtfully, they did come with limitations. Due to the fact that both of these measurements have been used and validated in other African contexts, it was decided that it would not be unreasonable to use them in the current study. Other scales that had only been validated in Western countries were not considered. Additionally, the translator of the GWBS and MHC scales from English to Kiswahili is an esteemed linguist, speaking both fluent English and Kiswahili. Therefore, even the idioms and figures of speech found in the GWBS and MHC were properly treated. However, due to the many variations between African nations, especially between those more and less developed, it would be advisable to create and validate a Kiswahili psychological wellbeing scale specifically for rural locations in Tanzania, or East Africa in general.

Second, the small sample size ( $n = 58$ ) limited the ability to generalize the findings to the population of all Tanzanian young adults, or even of all young adults in the Iringa region. The fact that the surveys had to be administered orally, taking around half an hour each, hindered our ability to get a larger sample size. Though our data cannot be generalized to a regional population, the villages sampled had small populations that may allow for the sample size of 58 to be indicative of the larger population of young adults in Iyayi, Mwaya, Fyogo, and Luhunga.

Third, the study did not employ a longitudinal design and as a result, causal inference between parental loss and psychological wellbeing could not be drawn. Gathering data about psychological symptoms at different time-points would be necessary in order to understand any potential causal relationships.

## FUTURE RESEARCH

There are many areas in which future research would be helpful in evaluating the current study’s results. To begin, creating a specific measure to address wellbeing in the context of rural Tanzania and validating it would allow the researchers to be certain of the cultural appropriateness of the measure used. In order to create this scale, qualitative methods, including in-depth interviews and focus groups, and a proper field-testing would be useful.

Furthermore, a larger sample size, potentially from more villages within Mufindi, would be necessary in order to be able to analyze the demographics (age, sex) and differences in family structures (paternal, maternal, double orphans).

This study's initial intent was to perform analyses using these variables, but due to the distribution of the results received, significant analyses were not powerful enough.

To conclude, it would be interesting to further this field of research by inquiring about the circumstances of parental death of the young adults. Potential variations in the trauma involved and HIV/AIDS status of the parents and participants could all be factors explored in future research. This is a field of research that could have great policy implications and should certainly be investigated further.

### ACKNOWLEDGEMENTS

I thank Paulo Kateme for the translation of all tools from English to Kiswahili, Steven Chumi for his support as a research assistant and translator, Justin Beckham for his guidance and assistance, and Dr. Cindy Hazan and the Cornell IRB for their timeliness and understanding. I also convey my appreciation for the hospitality and participation of the young adults in Mufindi. Lastly, I am forever grateful for my amazing parents, who enabled me to have this opportunity in the first place.

### REFERENCES

1. The World Factbook. (2015, September 24). Retrieved October 1, 2015, from <https://www.cia.gov/library/publications/the-world-factbook/geos/tz.html>
2. Carlson, R., & Pratt, M. (2015). Tanzania. Retrieved October 8, 2015, from <http://www.everyculture.com/Sa-Tb/Tanzania.html>
3. Tanzania National Bureau of Statistics (2012). "2011–12 Tanzania HIV/AIDS and Malaria Indicator Survey (THMIS)."
4. Tanzania National Bureau of Statistics (2011). Iringa Region GDP Report 2008.
5. Kwesigabo, G., Mwangi, M. A., Kakoko, D. C., & Killewo, J. (2012). Health challenges in Tanzania: Context for educating health professionals. *Journal of Public Health Policy*, 33, S23–S34. <http://doi.org/10.1057/jphp.2012.47>
6. United Nations Children's Fund, "Children: The Missing Face of AIDS: A call to action", UNICEF, New York, 2005, 11.
7. Leach, V. (2007). *Children and Vulnerability in Tanzania: A Brief Synthesis. Research on Poverty Alleviation*.
8. Vulnerable Childcare. (2014). Retrieved October 1, 2015, from <http://mufindiorphans.org>
9. Kitaluka, N. 2006. "A Brief Report on Biodiversity Conservation Assessment and Agriculture Practices in Villages Surrounding Unilever Tea Tanzania plantations." Mufindi District Forest Office.
10. Martikainen, P. (2002). Psychological determinants of health in social epidemiology. *International Journal of Epidemiology*, 31(6), 1091–1093. <http://doi.org/10.1093/ije/31.6.1091>
11. Tanzania Culture. (2015). Retrieved October 1, 2015, from <http://tanzania.peacecorps.gov/content/tanzanian-culture>.
12. Doku, P. N. (2009). Parental HIV/AIDS status and death, and children's psychological wellbeing. *International Journal of Mental Health Systems*, 3, 26.
13. Makame, V. Ani, C. and Grantham-McGregor, S. (2002) Psychological well-being of orphans in Dar El Salaam, Tanzania, *Acta Paediatrica*, 91, 459–465.
14. Atwine, B., Cantor-Graae, E., and Bajunirwe F. (2005). Psychological distress among AIDS orphans in rural Uganda. *Social Science & Medicine*, 61(30), 555-564. doi:10.1016/j.socscimed.2004.12.018
15. Nyamukapa, C. A., Gregson, S., Wambe M., Mushore P., Lopman B., Mupambireyi Z., Nhongo K. and Jukes M.C.H. (2010) Causes and consequences of psychological distress among orphans in eastern Zimbabwe, *AIDS Care: Psychological and Socio-medical Aspects of AIDS/HIV*, 22(8), 988–996.
16. Lewis-Morrarty, E., Degnan, K. A., Chronis-Tuscano, A., Pine, D. S., Henderson, H. A., and Fox, N. A. (2015). Infant Attachment Security and Early Childhood Behavioral Inhibition Interact to Predict Adolescent Social Anxiety Symptoms. *Child Development*, 86(2), 598–613. <http://doi.org/10.1111/cdev.12336>
17. Raby, K. L., Roisman, G. I., Fraley, R. C. and Simpson, J. A. (2015), The Enduring Predictive Significance of Early Maternal Sensitivity: Social and Academic Competence Through Age 32 Years. *Child Development*, 86: 695–708. doi: 10.1111/cdev.12325
18. Tyrka, A.R., Wier, L., Price, L.H., Ross, N., Anderson, G.M., Wilkinson, C.W., and Carpenter, L.L. (2008) Childhood parental loss and adult Hypothalamic-Pituitary-Adrenal function, *Biological Psychiatry*, 63(12), 1147–1154.

19. Brent, D., Melhem, N., Donohoe, M. B., and Walker, M. (2009). The Incidence and Course of Depression in Bereaved Youth 21 Months After the Loss of a Parent to Suicide, Accident, or Sudden Natural Death. *The American Journal of Psychiatry*, 166(7), 786–794.
20. “Children on the Brink 2002: A Joint Report on Orphan Estimates and Program Strategies.” New York: UNICEF, November 2002.
21. Keyes, C. L. M. (2006). Mental health in adolescence: Is America’s youth flourishing? *American Journal of Orthopsychiatry*, 76, 395–402.
22. Keyes, C. L. M., Wissing, M., Potgieter, J. P., Temane, M., Kruger, A., and van Rooy, S. (2008). Evaluation of the mental health continuum—short form (MHC–SF) in setswana-speaking South Africans. *Clinical Psychology & Psychotherapy*, 15(3), 181–192. doi:10.1002/cpp.572
23. Westerhof, G. J., & Keyes, C. L. M. (2010). Mental Illness and Mental Health: The Two Continua Model Across the Lifespan. *Journal of Adult Development*, 17(2), 110–119. doi:10.1007/s10804-009-9082-y
24. Khumalo, I.P., Temane, Q.M., & Wissing, M.P. (2010). Development and initial validation of a General Psychological Well-being Scale (GPWS) in an African context. *Journal of Psychology in Africa*, 20(1), 13–22.
25. Evans, R. M. C. (2005). Social Networks, Migration, and Care in Tanzania: Caregivers’ and children’s resilience to coping with HIV/AIDS. *Journal of Children and Poverty*, 11(2), 111–129. <http://doi.org/10.1080/10796120500195527>
26. Resnick, M. D. (2000). Resilience and protective factors in the lives of adolescents. *The Journal of Adolescent Health: Official Publication of the Society for Adolescent Medicine*, 27(1), 1–2.
27. Heinzer, M. (1993). “Adolescent resilience following parental death in childhood and its relationship to parental attachment and coping.” Case Western Reserve University (Health Sciences).

#### **ABOUT THE STUDENT AUTHOR**

Callie Silver is a senior at Cornell University, majoring in Human Development with a concentration in Social and Personality Development, and minors in Policy Analysis and Management, Inequality Studies and Law and Society. She will be graduating with a B.S. in May 2016. She conducted this independent research during her semester abroad in Tanzania.

#### **PRESS SUMMARY**

The HIV/AIDS epidemic in Sub-Saharan Africa has raised serious concerns about the wellbeing of orphaned children. The current study sought to understand the lasting psychological effects in young adulthood of parental loss during childhood. Using data from a small, rural village in Tanzania, the effects of orphanhood in a non-Western setting were trying to be better understood. The results indicate that supportive, close-knit communities may serve as a protective factor for children who have experienced parental loss.

